

OPTICAL PROPERTIES OF III-NITRIDE SEMICONDUCTORS AND  
THE APPLICATIONS IN ALL-OPTICAL SWITCHING

By

Yueling Wan

M.Eng. (Telecommunications), Asian Institute of Technology, 1997  
M.S. (Physics), University of Memphis, 2000

Submitted to the Department of Electrical Engineering and Computer Science and the  
Faculty of the Graduate School of the University of Kansas  
In partial fulfillment of the requirements for the degree of  
Doctor of Philosophy

---

Chairperson

Committee members

---

---

---

Date defended: \_\_\_\_\_

The Dissertation Committee for Yueling Wan certifies  
that this is the approved version of the following dissertation:

**OPTICAL PROPERTIES OF III-NITRIDE SEMICONDUCTORS AND  
THE APPLICATIONS IN ALL-OPTICAL SWITCHING**

Committee:

---

Chairperson

---

---

---

---

Date approved: \_\_\_\_\_

*To  
My Parents and Siblings*

## **ACKNOWLEDGEMENTS**

I would like to express my gratitude to Dr. Rongqing Hui, my committee chair, for his guidance throughout this research work and for his precious advice and support during my graduate studies here at the University of Kansas. His encouragement and full support led me to the success of this work. I have also been able to learn a lot from him about being a better researcher. It was an absolute pleasure working for him the past five years.

I would also like to thank other members of my committee, Dr. Christopher Allen, Dr. Victor Frost, Dr. Hongxing Jiang and Dr. Karen Nordheden, for serving on my dissertation committee and giving me invaluable suggestions through out my research work. Also, I would like to express my thanks to the National Science Foundation for providing the financial support for my research work.

Finally, I would like to thank my family and friends for their patience and encouragement throughout the work of my dissertation. The support from them makes this work successful.

## ABSTRACT

The goal of this research was to build an  $N \times N$  all-optical WDM switch, which is indispensable for the next-generation of all-optical packet-switched networks. We started from the basic concepts of telecommunication network architectures, optical networks, WDM network elements and basic components in optical networks. We focused on the principles and applications of optical couplers, Mach-Zehnder Interferometers (MZI), arrayed waveguide gratings (AWG), and some switch architectures and techniques that have helped in the design of the optical switch.

Based on the AWG principle, we derived a general design rule for constructing an  $N$ -interleaved AWG ( $N$ -IAWG), and proposed a  $1 \times N$  WDM switch consisting of two  $N$ -IAWGs and a phase shifter array. We then simplified the structure by using only one  $N$ -IAWG with total reflection implemented at the end of each phase shifter. The simplified structure significantly reduced the device size and relaxed the design tolerance. This suggests that it could be used as the fundamental building block to construct non-blocking  $N \times N$  all-optical WDM switches with Spanke architecture.

The feasibility of the proposed optical switch depends on the refractive index tuning in the phase shifter array, which can be realized through the carrier-induced index tuning of semiconductors. We proposed to use III-nitride semiconductors due to

their unique characteristics, and presented a theoretical study of carrier-induced refractive index change in GaN in the infrared wavelength region. Calculations verified that the magnitude of carrier-induced refractive index change is high enough for the application to the proposed optical switch.

We then prepared various devices in GaN/AlGaN material and characterized their optical properties in the 1550 nm wavelength region experimentally. We measured the refractive indices and the impact of Al concentrations. We also measured the birefringence of the GaN waveguides, which helped understand the polarization effect in the devices and would help design polarization independent optical waveguides. Among the devices we prepared, there was an eight-wavelength AWG, which was the first AWG in GaN/AlGaN material. The performance of the AWG agreed well with our design expectations and may be a foundation for the application in optical switches.

## TABLE OF CONTENTS

<b>1. Introduction.....</b>	<b>1</b>
<b>2. Optical Networking and Switching.....</b>	<b>4</b>
2.1. Introduction.....	4
2.2. Telecommunications Network Architecture.....	4
2.3. Optical Networks.....	8
2.3.1. Multiplexing Techniques .....	8
2.3.2. Second-Generation Optical Networks.....	10
2.4. WDM Network Elements.....	12
2.5. Basic Components.....	17
2.5.1. Couplers.....	17
2.5.2. Mach-Zehnder Interferometer.....	20
2.5.3. Arrayed Waveguide Grating.....	23
2.6. Optical Switches.....	26
2.6.1. Large Optical Switch Architectures.....	28
2.6.2. Optical Switch Technologies.....	31
2.7. WDM Optical Switches.....	36
2.7.1. Design of Passive Waveguide Devices.....	36
2.7.2. Design of Carrier Controlled Simple Waveguide Devices.....	40
2.7.3. Design of Carrier Controlled AWG All-Optical Switch.....	47
2.8. Design of All-Optical Switch Networks.....	52
2.9. Conclusion.....	53
<b>3. Design of WDM Cross Connect Based on Interleaved AWG (IAWG) and a Phase Shifter Array.....</b>	<b>54</b>

3.1.	Introduction.....	54
3.2.	An Approach of an $N \times N$ All Optical Switch.....	56
3.3.	The Scheme of the $1 \times N$ All-Optical Switch.....	58
3.4.	Design of the N-IAWG.....	59
3.4.1.	Functionality of N-IAWG.....	59
3.4.2.	From AWG to IAWG.....	61
3.4.3.	AWG Multiple-Beam Interference Condition.....	63
3.4.4.	Vector Illustration of the AWG Multiple-Beam Interference Condition.....	65
3.4.5.	Additional Lengths to Arrayed Waveguides for Constructing 4-IAWG.....	66
3.4.6.	General Design Rule of N-IAWG.....	69
3.4.7.	Output Port Arrangement.....	70
3.4.8.	Comparison with Previous Results.....	71
3.4.9.	Verification of Equal Vector Magnitudes in BZs of N-IAWG...	73
3.4.10.	Verification of N-IAWG with Numerical Simulation.....	79
3.4.11.	Transfer function of an N-IAWG.....	83
3.4.12.	Extinction Ratio Versus the Interleaved Number N.....	85
3.5.	Realization of a $1 \times N$ All Optical Switch.....	86
3.5.1.	The Transfer Function of a $1 \times N$ All-Optical Switch.....	86
3.5.2.	Switching Functionality Verification and Phase Change Information.....	87
3.5.3.	Simulation Verification -----An Example.....	90
3.5.4.	The Scheme of Mirror $1 \times N$ All-Optical Switch.....	94
3.6.	Conclusion.....	96

<b>4. Carrier Induced Refractive Index Changes in GaN/AlGaN Semiconductors.....</b>	<b>98</b>
4.1. Introduction.....	98
4.2. Carrier-Induced Refractive Index Change in Semiconductors.....	100
4.2.1. Bandfilling.....	100
4.2.2. Bandgap Shrinkage.....	114
4.2.3. Free-Carrier Absorption.....	116
4.2.4. Combination of Effects.....	118
<b>5. GaN Material Design and Experiments.....</b>	<b>123</b>
5.1. Introduction.....	123
5.2. Optical Waveguide Theory.....	124
5.2.1. Symmetric Dielectric Slab Waveguides.....	125
5.2.2. Asymmetric Dielectric Slab Waveguides.....	130
5.2.3. Rectangular Dielectric Waveguides.....	131
5.3. Beam Propagation Method.....	137
5.3.1. Finite Difference Method Analysis of Planar Optical Waveguides.....	138
5.3.2. FDMBPM Analysis of Rectangular Waveguides.....	140
5.3.3. Straight Waveguide Design with BPM Software.....	141
5.4. Measurement Method and Experimental Setup.....	152
5.4.1. Measurement Method Based On Feby-Perot (FP) Interference.	152
5.4.2. Experimental Setup.....	154
5.5. Measurement of Refractive Indices in Infrared.....	155
5.6. Measurement Results of the Single-Mode GaN/AlGaN Waveguides....	157
5.6.1. Experimental Results: Power Loss in Waveguide Transmission.	157

5.6.2. Birefringence of GaN/AlGaN optical waveguides.....	159
5.7. Design of the Optical Couplers and the Mach-Zehnder Interferometer Device with GaN/AlGaN.....	166
5.7.1. Simulation Results of Couplers and Mach-Zehnder Interferometer Device.....	167
5.7.2. A Simple Example: Waveguide Coupler.....	169
5.8. The AWG Based on the GaN/AlGaN Heterostructures.....	170
5.8.1. Simulation Results of the Arrayed Waveguide Gratings.....	172
5.8.2. A Sample: A Fabricated Arrayed Waveguide Grating.....	174
5.9. The Thermal Stability of the Refractive Index.....	177
<b>6. Conclusions and Future Work.....</b>	<b>182</b>
6.1. Conclusions.....	182
6.2. Future Work.....	185
<b>7. Bibliography.....</b>	<b>188</b>

## LIST OF FIGURES

Figure 2.1.	An overview of a public fiber network architecture.....	5
Figure 2.2.	Different types of time division of multiplexing: (a) fixed, (b) statistical.....	7
Figure 2.3.	Different multiplexing techniques for increasing the transmission capacity on an optical fiber. (a) Electronic or optical time division multiplexing and (b) wavelength division multiplexing.....	9
Figure 2.4.	A WDM wavelength-routing network, showing optical line terminals (OLTs), optical add/drop multiplexers (OADMs), and optical crossconnects (OXCs). The network provides lightpaths to its users, which are typically IP routers or SONET terminals.....	11
Figure 2.5.	Block diagram of an optical line terminal.....	12
Figure 2.6.	Illustrating the role of optical add/drop multiplexers.....	13
Figure 2.7.	A fully tunable OADM.....	14
Figure 2.8.	An OXC is applied in the network.....	15
Figure 2.9.	An optical core wavelength plane OXC.....	16
Figure 2.10.	A directional coupler.....	17
Figure 2.11.	A basic $2 \times 2$ Mach-Zehnder Interferometer.....	20
Figure 2.12.	Transfer functions of the basic $2 \times 2$ Mach-Zehnder Interferometer...	22
Figure 2.13.	Illustration of an arrayed Waveguide Grating structure.....	25
Figure 2.14.	Configuration of the star coupler.....	25
Figure 2.15.	A $4 \times 4$ crossbar switch realized using 16 $2 \times 2$ switches.....	28

Figure 2.16.	A strict-sense nonblocking three-stage $1024 \times 1024$ Clos architecture switch.....	29
Figure 2.17.	A strict-sense nonblocking Spanke architecture $n \times n$ switch.....	30
Figure 2.18.	An analog beam steering mirror.....	32
Figure 2.19.	An $n \times n$ switch built using two arrays of analog beam steering MEMS mirrors.....	33
Figure 2.20.	Mach-Zehnder Interferometer As Thermo-Optical Switch.....	35
Figure 2.21.	Schematic diagram illustrating the operation of a wavelength router: (a) Interconnectivity scheme ( $a_i$ denotes the signal at input port $a$ with frequency $i$ ) and (b) Frequency response.....	37
Figure 2.22.	Three different ADM configurations: (a) Loop-back, (b) fold-back, and (c) cascaded demux/mux.....	39
Figure 2.23.	Schematic diagram of a tunable filter with a ladder-type structure...	41
Figure 2.24.	(a) AWG Functioning As a Filter. (b) Electrode Controlled AWG Filter.....	44
Figure 2.25.	Electrode Controlled AWG Filter, with different lengths of electrodes.....	46
Figure 2.26.	Schematic diagram of the interleave cross connect. The inset in the lower left corner illustrates the Brillouin zones for star coupler 2....	48
Figure 2.27.	Carrier Controlled Loop-Back Add-Drop Switch (a) Schematic Diagram, (b) Corresponding Black Box.....	51
Figure 2.28.	$1 \times N$ Wavelength Switch Network.....	52
Figure 3.1.	The scheme of $4 \times 4$ all-optical switch.....	57
Figure 3.2.	Schematic diagram of $1 \times N$ all-optical switch.....	59
Figure 3.3.	Schematic diagram of $N$ -IAWG.....	60

Figure 3.4.	Diagram of output port distribution for an $N$ -interleaved AWG. (a) An $N$ -interleaved AWG, where $N = 4$ ; (b) Close-up of the output star coupler, where $\Omega_i$ ( $i = -1, 0, 1, 2$ ) denotes the new Brillouzin zones of this 4-IAWG. These new BZs were split from the central BZ of a conventional AWG before it was interleaved.....	64
Figure 3.5.	(a) Diagram of output port distribution for a 5-interleaved AWG. (b) Close-up of the output star coupler, where $\Omega_i$ ( $i = -2, -1, 0, 1, 2$ ) denotes the new BZs of this 5-IAWG. These new BZs were split from the central BZ of a conventional AWG before it was interleaved.....	74
Figure 3.6.	(a) The changes of the signal vectors in BZ $\Omega_1$ when an AWG changes to a 5-IAWG; (b) The changes of the signal vectors in BZ $\Omega_2$ when an AWG changes to a 5-IAWG.....	77
Figure 3.7.	Verification of 4-IAWG. The output powers at its related four output ports are exactly the same for each channel. (a) Central channel with wavelength $\lambda_0 = 1550$ nm, (b) Channel of wavelength 1549.2 nm, (c) Channel of wavelength 1549.6 nm, (d) Channel of wavelength 1550.4 nm.....	81
Figure 3.8.	Schematic diagram of $1 \times 4$ switch for single channel with wavelength $\lambda_0$ .....	89
Figure 3.9.	Simulation result of $1 \times 4$ switch for four wavelength channels with wavelengths 1549.2 nm, 1549.6 nm, 1550.0 nm and 1550.4 nm with a channel spacing of 0.4 nm. The 1550.0nm channel was switched to output port 1, 1549.6nm channel to output 2, 1550.4nm channel to output 3 and 1549.2nm channel to output 4.....	91

Figure 3.10. Simulation result of $1 \times 4$ switch for four wavelength channels with wavelengths 1549.2 nm, 1549.6 nm, 1550.0 nm and 1550.4 nm with a channel spacing of 0.4 nm. The crosstalk between channels is round $-32$ dB or less.....	92
Figure 3.11. Mirror scheme of $1 \times N$ all-optical switch.....	94
Figure 3.12. Simulation result of the mirror scheme of $1 \times (N-1)$ all-optical switch for $N = 4$ .....	95
Figure 4.1. Energy band structure and Bandfilling effect for direct-gap semiconductor. Absorption of a photon can occur only between occupied valence band states and unoccupied conduction band states.....	101
Figure 4.2. The absorption coefficient versus photon energy for GaN layer grown on sapphire. $T = 293$ K.....	107
Figure 4.3. The absorption coefficient versus photon energy for GaN layer grown on sapphire. $T = 10$ K (Provided by Dr. Wei Shan).....	109
Figure 4.4. Change in absorption due to electron-hole injection and the resulting Bandfilling in GaN. Note: the vertical values are in logarithm.....	110
Figure 4.5. Change in refractive index due to Bandfilling effect of GaN. $N = P = 3.0 \times 10^{17}, 1.0 \times 10^{18}, 3.0 \times 10^{18}, 1.0 \times 10^{19} \text{ cm}^{-3}$ .....	111
Figure 4.6. Index change versus signal wavelength due to Bandfilling effect in GaN. Solid line: $N = 7 \times 10^{18} \text{ cm}^{-3}$ , dashed line: $N = 3 \times 10^{19} \text{ cm}^{-3}$ , dotted line: $N = 6 \times 10^{19} \text{ cm}^{-3}$ .....	112
Figure 4.7. Change of refractive index versus carrier density at 1550 nm for GaN.....	113

Figure 4.8.	Change of refractive index of GaN due to electron-hole injection and the resulting band-gap shrinkage.....	115
Figure 4.9.	Index change versus signal wavelength due to bandgap shrinkage effect of GaN. Solid line: $N = 7 \times 10^{18} \text{ cm}^{-3}$ , dashed line: $N$ $= 3 \times 10^{19} \text{ cm}^{-3}$ , dotted line: $N = 6 \times 10^{19} \text{ cm}^{-3}$ .....	116
Figure 4.10.	Index change versus signal wavelength due to plasma effect of GaN. Solid line: $N = 7 \times 10^{18} \text{ cm}^{-3}$ , dashed line: $N = 3 \times 10^{19} \text{ cm}^{-3}$ , dotted line: $N = 6 \times 10^{19} \text{ cm}^{-3}$ .....	118
Figure 4.11.	Predicted changes in refractive index of GaN from the combination of three effects (the dashed line). $N = P = 3 \times 10^{19} / \text{cm}^3$ .....	119
Figure 4.12.	Overall index change versus wavelength calculated at three carrier density levels: $N = 7 \times 10^{18} \text{ cm}^{-3}$ (solid line), $3 \times 10^{19} \text{ cm}^{-3}$ (dashed line) and $6 \times 10^{19}$ , (dotted line).....	120
Figure 4.13.	Index change versus carrier density calculated at 1550nm wavelength.....	121
Figure 5.1.	A symmetric dielectric slab waveguide, where x-y is the cross-section plane and z is the propagation direction.....	125
Figure 5.2.	A graphical solution for determining $\alpha$ and $k_x$ for the modes in symmetric dielectric slab waveguide.....	127
Figure 5.3.	An asymmetric dielectric slab waveguide.....	129
Figure 5.4.	A rectangular dielectric waveguide.....	131
Figure 5.5.	Intensity patterns in a rectangular waveguide where $w/d = 2$ , the refractive index of the waveguide $n_1 = 1.5$ , and the background medium has $n_0 = 1$ .....	133

Figure 5.6.	(a) A rectangular dielectric waveguide to be solved using the effective index method. (b) Solve the slab waveguide at each fixed $y$ and obtain an effective index profile $n_{\text{eff}}(y)$ . (c) Solve the slab waveguide problem with the $n_{\text{eff}}(y)$ .....	135
Figure 5.7.	The design of a layered rectangular waveguide with <i>BeamPROP</i> . (a) Refractive index distribution. (b) The illustration of the cross section of waveguide design. The refractive index is illustrated in different colors. (c) Vertical cut of index profile of the rectangular waveguide.....	142
Figure 5.8.	The mode calculation of a layered rectangular waveguide with <i>BeamPROP</i> . (a) The basic mode. (b) The illustration of the cross section of waveguide design. The refractive index is illustrated in different colors. (c) Vertical cut of index profile of the rectangular waveguide.....	145
Figure 5.9.	The cross section of the design of GaN single-mode waveguide.....	148
Figure 5.10.	Simulation result of the designed GaN single-mode waveguide with <i>BeamPROP</i> . (a) Single mode simulation verification and the effective refractive index; (b) Radiation pattern versus exit angle; (c) Refractive index characteristics along $Y$ direction, at $X = 0$ .....	150
Figure 5.11.	Fiber-optical experimental setup.....	154
Figure 5.12.	(a) Refractive indices of $\text{Al}_x\text{Ga}_{1-x}\text{N}$ versus wavelength for several different Al molar fractions. (b) Sellmeier expansion coefficients versus Al molar fractions.....	156
Figure 5.13.	Measured optical transmission spectrum (solid point) and numerical fitting using equation (2-13) (continuous line).....	158

Figure 5.14.	The wurtzite structure of GaN unit cell and the choice of coordinates.....	160
Figure 5.15.	Waveguide sample. Waveguide differs by the angle $\theta$ .....	160
Figure 5.16.	Birefringence measurement experimental setup.....	161
Figure 5.17.	Measured (solid dots) and calculated (continuous lines) optical transfer function with the input optical field perpendicular (trace 1), parallel (trace 3) and $45^0$ from (trace 2) the crystal c-axis.....	162
Figure 5.18.	Measured birefringence versus waveguide orientation (solid squares). The continuous line is a sinusoid fitting using, $\Delta n = 0.04275 - 0.00545 \cos(6\theta)$ , where $\theta$ is in degree.....	164
Figure 5.19.	Simulation of a 3dB coupler.....	166
Figure 5.20.	Simulation of M-Z Interferometer optical switch controlled by carrier induced refractive index change.....	167
Figure 5.21.	Microscopic images of a $2 \times 2$ GaN/AlGaN heterostructure optical waveguide coupler (a) top view and (b) cross section at the output...	168
Figure 5.22.	Measured output optical power vs the probe displacement in the horizontal direction for a $2 \times 2$ GaN/AlGaN heterostructure optical waveguide coupler. The input optical signal is launched at port 1....	169
Figure 5.23.	(a) Arrayed waveguide grating configuration, (b) simulation output result.....	173
Figure 5.24.	Microscope picture (a) and measured optical transfer function (b) of an AWG-based WDM coupler with 2nm channel separation.....	176

Figure 5.25. Calculated temperature sensitivity of AlGaN refractive index, (a) as a function of operation temperature for different Al concentration x and, (b) as a function of Al concentration with a fixed operating temperature at 25  $^{\circ}\text{C}$ ..... 180

## LIST OF TABLES

Table 3.1.	Initial Vector Information for Constructing a 4-IAWG.....	65
Table 3.2.	Vector Information of a Constructed 4-IAWG.....	67
Table 3.3.	Multiple sets of additional waveguide lengths [ $\lambda_c$ ] in the design of an $N$ -IAWG.....	70
Table 3.4.	Comparisons between the distributions of additional waveguide lengths [ $\lambda_c$ ] in the design of IAWG.....	72
Table 3.5.	Initial Vector Information of Constructing a 5-IAWG.....	76
Table 3.6.	Extinction ratio ( $ER$ ) versus the interleaved number $N$ .....	86
Table 3.7.	Phase changes ( $\Delta\theta$ ) needed in phase shifters for each output port selection in $1\times 4$ all-optical switch ( $\lambda = 1550$ nm).....	93
Table 3.8.	Refractive index changes ( $\Delta n$ ) needed in phase shifters with length $LP = 2$ mm for each output port selection in $1\times 4$ all-optical switch ( $\lambda = 1550$ nm).....	93
Table 4.1.	Values of Semiconductor Parameters ( $T = 300$ K).....	103
Table 4.2.	Values of GaN Semiconductor Parameters ( $T = 300$ K).....	108

## 1. Introduction

Internet traffic has been doubling every four to six months, and this trend appears set to continue for a while [1]. This explosive growing of Internet traffic requires the development of new technologies to fully utilize the wide bandwidth of optical fibers (more than 50 THz [2]) and to manage the huge volume of data information more efficiently. Although fiber-optic telecommunications has been going through an enormous development since optical fibers have been applied in this area, finding new optical materials, developing new fundamental optical devices and designing new optical subsystems are still critical issues in constructing all-optical telecommunications networks.

Unlike other communication technologies, optical technology offers a new dimension, the color of light, to perform such network functions as multiplexing, routing, and switching. Wavelength division multiplexing (WDM) techniques effectively use the wavelength as an additional degree of freedom by concurrently operating distinct portions of the 1.3- to 1.6- $\mu\text{m}$  wavelength spectrum accessible within the fiber network [3]. In WDM systems, WDM optical multiplexers/demultiplexers, wavelength routers and optical amplifiers are the fundamental devices.

So far, silica-based arrayed waveguide gratings (AWG) have been widely used as WDM optical multiplexers and demultiplexers. However, due to its passive nature, the lack of tunability limited its applications in dynamic wavelength routings.

The combination with mechanical optical switches partly solved this problem [4][5]. But it was still limited at the circuit switch level instead of the demanded packet switch level, because of the slow response of the mechanical optical switch. InP is a semiconductor material and the planar photonics integrated circuit (PIC) based on it can be made tunable by carrier injection [6][7]. However, because of its high refractive index and relatively small waveguide size, InP based PIC has its own disadvantages such as, high scattering loss, high temperature sensitivity and high coupling loss with optical fibers [8]. It thus became quite natural to find some other semiconductor materials with lower refractive indices and lower temperature sensitivity than InP to make the WDM devices.

III-nitride wide band gap semiconductors (GaN, AlGaN and InGaN) have recently attracted intense attention [9][10] because of their unique characteristics. Their wide bandgap and the hardness of the material make it possible to operate at very high temperature and power levels and in harsher environments. The wide bandgap also makes the materials highly transparent to the wavelength in the near infrared region, which makes them excellent candidates for passive optical waveguide devices for long wavelength optical communication. On one hand, the refractive indices of III-nitride semiconductor materials (i.e.  $n = 2.34$  for GaN) are lower than those of InP ( $n = 3.5$ ) [11], which makes III-nitrides better than InP to fit with optical fibers. Additionally, the refractive index of III-nitrides can be varied and controlled for example by alloying GaN with different percentages of InN and AlN. This is essential for the design of integrated optical circuits. Furthermore, carrier injection in

heterostructures of InGaN/GaN and GaN/AlGaN can provide high-speed modulation of refractive indices in waveguides, which can be utilized to make wavelength selective optical routers based on fast switchable optical phased-arrayed (PHASAR) devices.

The research will focus on the optical properties of III-nitride materials, the design of the optical devices based on the materials and their applications in WDM fiber-optic networks. The goal is to realize all-optical packet switches.

This thesis is divided into six chapters. After this introductory chapter, chapter two presents a literature review. Chapter three outlines a complete theory about how to design a  $1 \times N$  and  $N \times N$  all optical switch. Chapter four shows physical properties and calculated parameters of GaN semiconductor materials. In chapter five, we show the results of the characterizations of the fabricated III-Nitride devices and our experimental measurements of the samples. Some important discoveries are also summarized in this chapter. Chapter six shows the conclusion and the future work needed in this area.

## **2. Optical Networking and Switching**

### **2.1. Introduction**

In this chapter, we will review some basic concepts of telecommunication system architectures, optical networks, WDM system elements and basic components in optical networks. Then our discussion will be focused on the concepts and structures of optical switches which are used in WDM technology. We will start by reviewing the Micro-Electro-Mechanical System (MEMS), which is currently a very popular technology in terms of its applications in the building of optical switches. Then we will review optical switches for WDM applications, in which we will discuss why WDM switches are different from conventional optical circuit switches and how to build WDM optical switches from simple integrated guided-wave optical devices. At the end, we will propose several unique designs of waveguide based WDM switches.

### **2.2. Telecommunications Network Architecture**

Optical fiber provides an excellent medium to transfer huge amounts of data per second (nearly 50 Tb/s). It has low cost per bit, extremely low bit error rates, low signal attenuation (0.25 dB/km around 1550nm), low signal distortion, low power requirement, low material use, small space requirement, and higher level of security. So far, fiber optic networks have been widely applied in telecommunications.

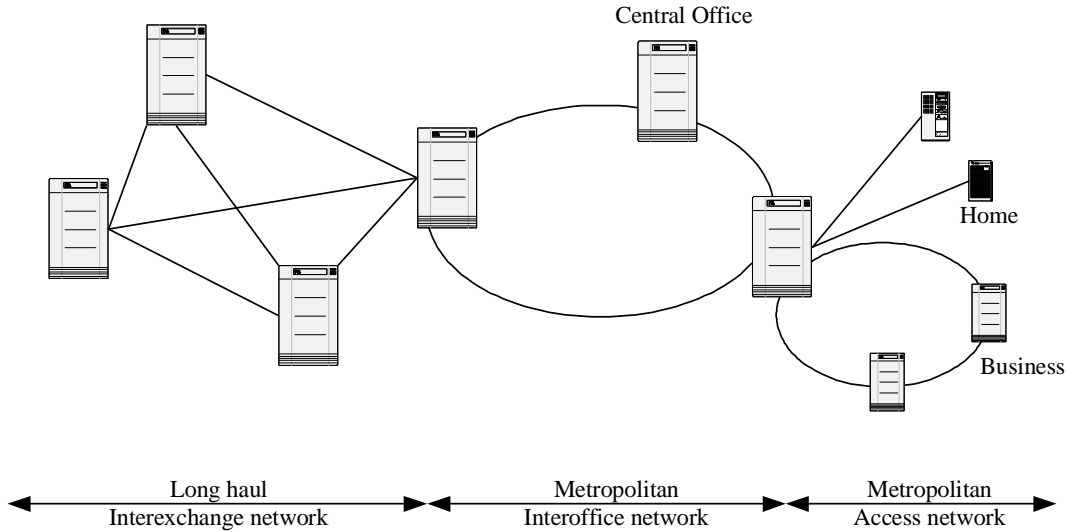


**Figure 2.1** An overview of a public fiber network architecture (after [1]).

Figure 2.1 shows an overview of a typical public fiber network architecture [1]. The network consists of a long-haul network and a metropolitan network. The long-haul network has a number of nodes with a pair of fibers between each other. It connects between cities and different regions that are usually separated by long distances. In this example, the connection between nodes for the long-haul network is in mesh format. However, ring topologies are also often deployed to provide alternative paths of traffic in case some of the links fail. The metropolitan network consists of a metropolitan interoffice network and a metropolitan access network. The interoffice network can have a link topology similar to that of the long-haul network. It connects groups of central offices within a city or region. The access network,

which typically covers a range of a few kilometers, extends from a central office out to individual businesses and homes.

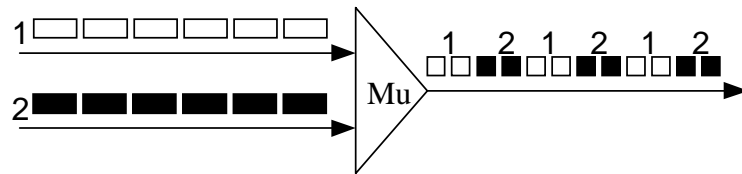
In a network as shown in Fig.2.1, there is always a concern about how to connect two different nodes to have information transmitted between them while the quality-of-service is guaranteed. Based on how traffic is multiplexed and switched inside the network, there are two fundamental types of underlying switch infrastructures: circuit-switch and packet-switch. A circuit-switched network provides the capability of switching circuit connections to its customers, in which a guaranteed amount of bandwidth is allocated to each connection. Once the connection is setup, the dedicated bandwidth for the customer is always available. The sum of the bandwidth of all the circuits, or connections, on a link must be less than the link bandwidth.

The problem with circuit switching is that it is not efficient in handling bursty data traffic. A bursty stream requires a lot of bandwidth from the network when all users are active and very little bandwidth when there is no demand. It is usually characterized by an average bandwidth and a peak bandwidth, which correspond to the long-term average and the short-term burst rates, respectively. In a circuit-switched network, one has to reserve sufficient bandwidth to deal with the temporary peak rate, while this bandwidth may be unused for most of the time.

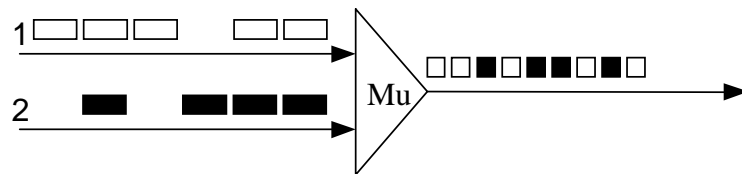
To deal with the problem of transporting bursty data traffic efficiently, packet switching was introduced in which the data stream is broken up into small packets of data and transmitted independently. Packet switching uses a technique called

statistical multiplexing when multiplexing multiple bursty data streams together on a link. Different types of time division multiplexing are shown in figure 2.2.

Since each data stream is bursty, it is probably unlikely that all the streams are active at any given time. Therefore the bandwidth required on the link can be made significantly smaller than that required when all streams were active simultaneously. This is the advantage of a packet-switched scheme. However, there are certainly disadvantages associated with packet-switched networks especially when a large number of streams are active simultaneously and the required bandwidth exceeds the available bandwidth on the link. However, this only requires more effort to be made from the carriers to provide some guarantees on the quality of service they offer.



(a)



(b)

**Figure 2.2** Different types of time division of multiplexing: (a) fixed, (b) statistical.  
(after [1])

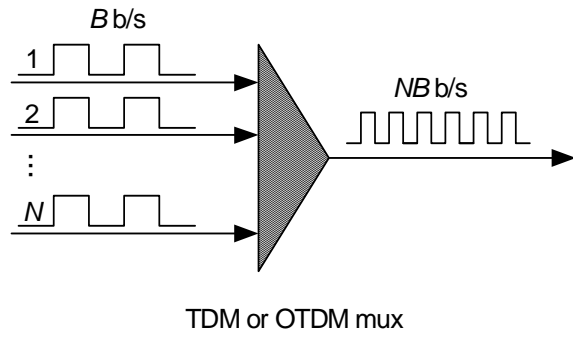
## **2.3. Optical Networks**

In addition to providing enormous capacities, an optical network also provides a common infrastructure over which a variety of services can be delivered. With optical fibers widely deployed and the evolution of telecommunication networks, optical networks have been evolved from the first generation, where optics was essentially used for transmission and simply to provide capacity, to the second generation, where some of the routing, switching, and intelligence is moving from the electronics domain into the optical layer. Before we describe the second-generation optical networks, let's look at the multiplexing techniques utilized in current optical networks.

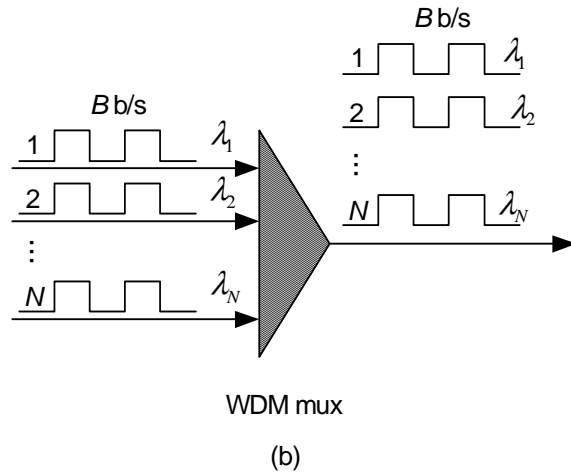
### **2.3.1 Multiplexing Techniques**

Multiplexing makes it possible to transmit data at higher rates and thus much more economical. It is more convenient for many reasons to transmit high speed data over a single fiber than to transmit lower data rates over multiple fibers. There are fundamentally two ways of traffic multiplexing as shown in figure 2.3, which are time division multiplexing (TDM) and wavelength division multiplexing (WDM). By utilizing higher-speed electronics, TDM increases the bit rate by interleaving lower-speed data streams to obtain the higher-speed stream at the transmission bit rate. To achieve even higher bit rates with TDM technology, researchers are working on methods to perform the multiplexing and demultiplexing all-optically. This approach is known as optical time division multiplexing (OTDM). On the other hand, WDM is essentially the same as frequency division multiplexing (FDM) in wireless systems. It

transmits data simultaneously at multiple carrier wavelengths over a fiber. Under first order approximation, there is no crosstalk between these wavelengths as long as they do not overlap with each other in the frequency domain. WDM has been widely deployed in long-haul networks, and now is being deployed in metro and regional access networks. [12].



(a)



(b)

**Figure 2.3** Different multiplexing techniques for increasing the transmission capacity on an optical fiber. (a) Electronic or optical time division multiplexing and (b) wavelength division multiplexing. (after [1])

WDM and TDM both provide ways to increase the transmission capacity and are complementary to each other. Therefore networks today use a combination of TDM and WDM.

### **2.3.2 Second-Generation Optical Networks**

The architecture of a second-generation optical network is shown in figure 2.4. This is a wavelength-routing network. The signals are transmitted from the source to the destination through light paths provided by the network. The light paths are optical connections from a source node to a destination node over a wavelength on each intermediate link. The wavelength being routed on the light path can be converted from one to another. The same wavelength can be used among different light paths in a wavelength routing network as long as the light paths do not share any common link. This means the wavelength can be reused spatially in different parts of the network.

Fundamental building blocks of this second-generation optical network include optical line terminals (OLTs), optical add/drop multiplexers (OADM), and optical cross-connects (OXCs), as shown in figure 2.4. An OLT multiplexes multiple wavelengths into a single fiber and demultiplexes a set of wavelengths on a single fiber into separate fibers. An OADM takes in signals of multiple wavelengths and selectively drops some of these wavelengths or adds some other wavelengths locally while letting others pass through. An OXC essentially performs a similar function in routing that switches wavelengths from one input port to another but at much larger sizes with the number of ports ranging from a few tens to thousands. Compared with

electronic switching, lightpath switching has an advantage in delivering data in a transparent fashion, which enables the network to interface with customers with a wide variety of demands. It is obvious that second-generation optical networks are capable of providing more functions than just point-to-point transmission.

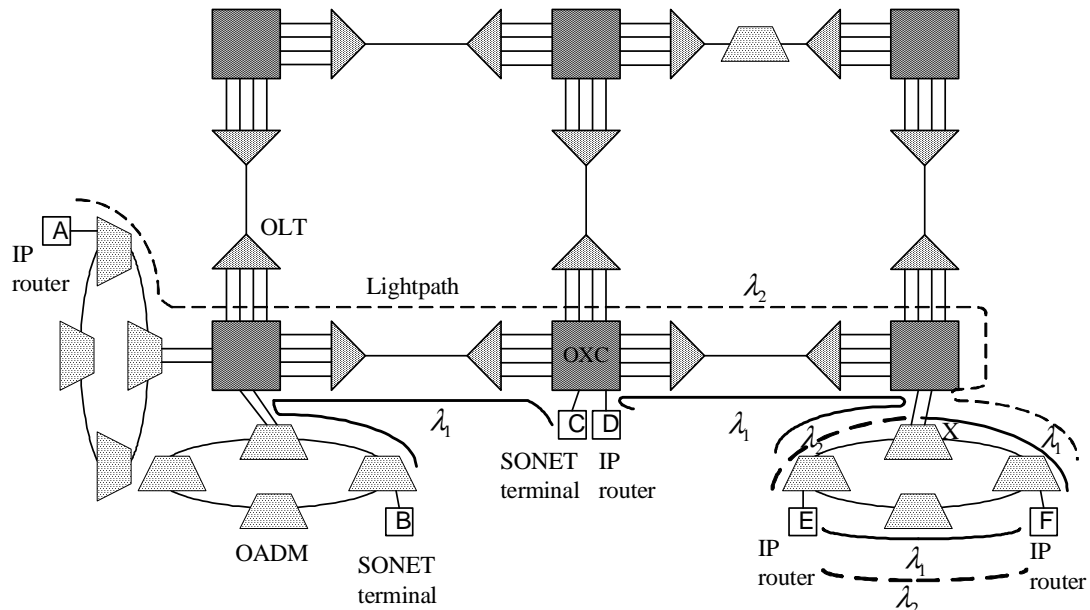


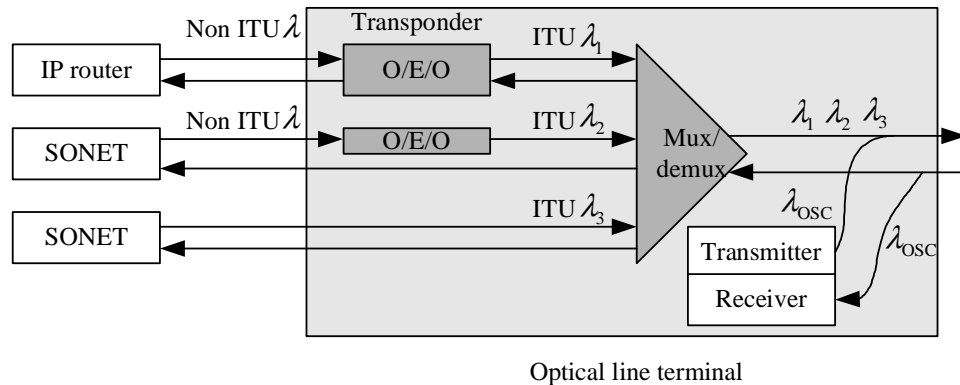
**Figure 2.4** A WDM wavelength-routing network, showing optical line terminals (OLTs), optical add/drop multiplexers (OADMs), and optical crossconnects (OXCs). The network provides lightpaths to its users, which are typically IP routers or SONET terminals. (after [1])

Optical networks based on the above architecture have been deployed and signaling protocols between IP routers and optical networks have been standardized

[13]. OLTs have been widely deployed for point-to-point applications. They can be shared by all the optical network units (ONUs) to reduce the number of expensive DWDM transceivers [14]. OADMs that support different data rates with same bandwidth efficiency are developed [15] and are now used in long-haul and metro networks [1][16][17][18]. OXCs were deployed primarily in long-haul networks because of their high capacity requirement.

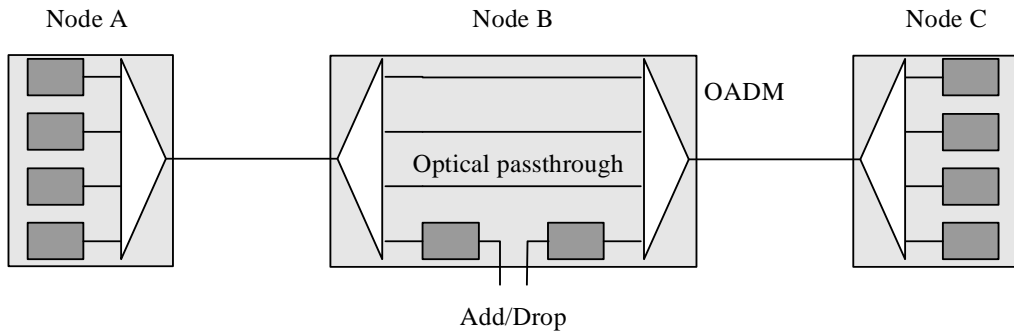
## 2.4. WDM Network Elements

As we mentioned above, OLT, OADM and OXC are three important elements in optical networks. The users of the network are connected to these elements. Now let's have a brief overview of these three important elements.



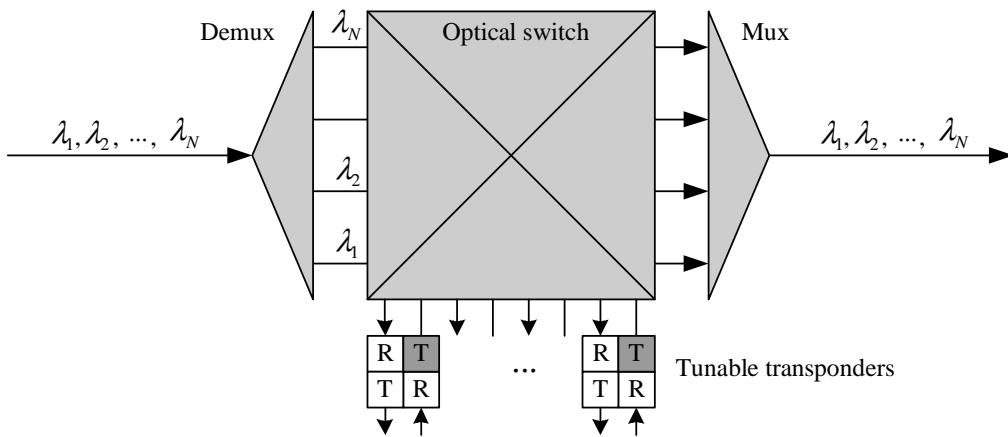
**Figure 2.5** Block diagram of an optical line terminal. (after [1])

Figure 2.5 shows a block diagram of an OLT [1]. An OLT is used at either end of a point-to-point link to multiplex and demultiplex wavelengths. From the figure, we can see that the signal coming out of a transponder is multiplexed with other signals of different wavelengths onto a fiber. In the opposite direction, the demultiplexer extracts the individual wavelengths and sends them either to the transponder or to the client directly. A transponder adapts the signal from a client into a signal suitable for use inside the optical network. Likewise, in the reverse direction, it adapts the signal from the optical network into a signal suitable for the client. From the figure, we can see that the OLT also terminates an optical supervisory channel (OSC), which is carried on a separate wavelength  $\lambda_{\text{OSC}}$ , which is different from the wavelengths carrying the actual traffic. From the description above, we can see that the basic components in an OLT structure are the multiplexer and the demultiplexer, which can be made by arrayed waveguide gratings (AWG), dielectric thin-film filters and fiber Bragg gratings.



**Figure 2.6** Illustrating the role of optical add/drop multiplexers. (after [1])

Figure 2.6 illustrates the role of an OADM. In this example, a wavelength-routing network is used. Nodes A and C are each deployed with an OLT and node B is deployed with an OADM. The OADM drops one of the four wavelengths to a local terminal and passes through three other remaining wavelengths. This is a cost-effective solution for wavelength add/drop realization. Basic components in node B are, again, a multiplexer and a demultiplexer.



**Figure 2.7** A fully tunable OADM. (after [1])

Figure 2.7 shows an ideal reconfigurable OADM architecture. The architecture is flexible and fully tunable regarding the channels being added or being dropped while still maintaining a low fixed loss. The basic components used in this structure are again a multiplexer and a demultiplexer, but in addition, an optical switch is required for dynamic wavelength routing.

OADMs are useful network elements to handle simple network topologies. For more complex mesh topologies with large traffic and a large number of wavelengths, OXCs are required. OXCs also help realize reconfigurable optical networks in which lightpaths can be set up or terminated as needed without having to distribute them beforehand. Figure 2.8 shows an OXC applied in the network. It terminates some fiber links, each usually carrying a large number of wavelengths and also passes other wavelengths through to other nodes. OXCs enable true mesh networks to be deployed. There are different versions of OXCs. But ideally, it should be able to provide lightpaths in a large network in an automated manner; it should be an intelligent network element that can detect failures in the network and rapidly reroute lightpaths around the failure; it should be bit rate transparent so that it can switch signals with arbitrary bit rates and frame formats, etc.

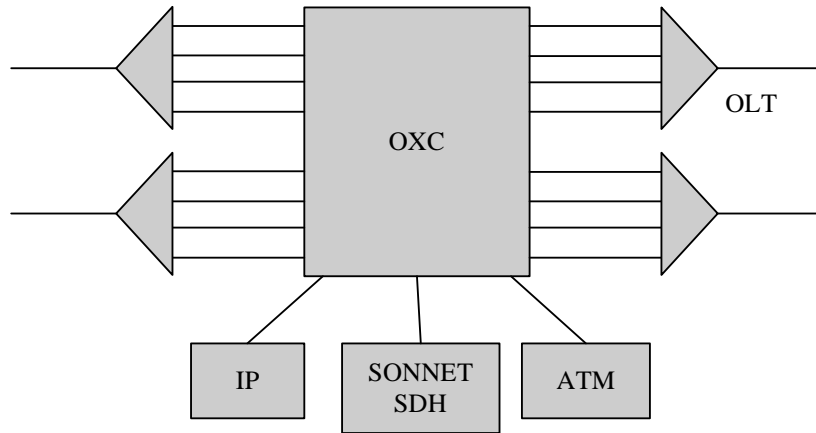


**Figure 2.8** An OXC is applied in the network. (after [1])

There is always a switch core in an OXC. The switching can be done either electrically or optically. It is certainly preferred to have it done all-optically since all-optical switches are more scalable in capacity, data rate transparent and it is not necessary to groom traffic. Figure 2.9 shows an optical core wavelength plane OXC, consisting of a plane of optical switches. The signals coming in from different fibers are first demultiplexed and then sent to the optical switches according to their wavelengths. Each optical switch switches signals with a specific wavelength. After the signals are switched, they are multiplexed back together by multiplexers. The configuration in figure 2.9 also shows the add/drop terminals for some channels.

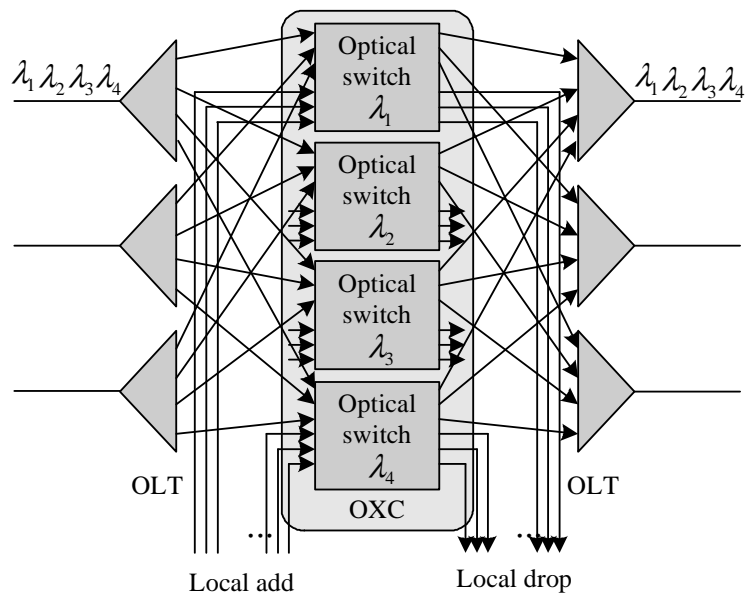


**Figure 2.9** An optical core wavelength plane OXC. (after [1])

## 2.5. Basic Components

In the above section, we see that multiplexing, demultiplexing and optical switching are indispensable functions in all-optical networks. Now we will present some basic components that are used to realize all these functions.

### 2.5.1 Couplers

A directional coupler is used to combine or split signals in an optical network. Figure 2.10 shows a  $2 \times 2$  coupler consisting of two input ports and two output ports. The power from one input port,  $P_0$  or  $P_3$ , can be split into two output ports  $P_1$ , and  $P_2$ .

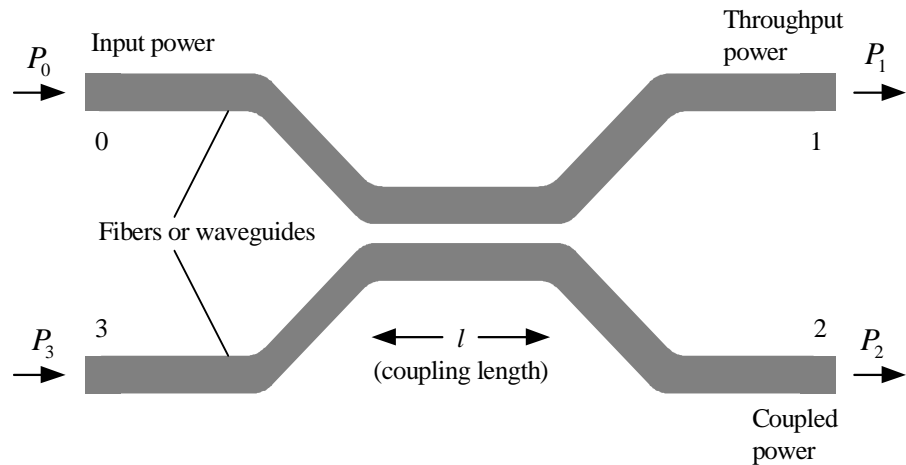


**Figure 2.10** A directional coupler.

A quantitative analysis of this coupling phenomenon can be found in [19]. A general form can be obtained for the relationship between the electric fields at the output side,  $E_1$  and  $E_2$ , and the electric fields at the input sides,  $E_0$  and  $E_3$  [1].

$$\begin{pmatrix} E_1(f) \\ E_2(f) \end{pmatrix} = e^{-j\beta l} \begin{pmatrix} \cos(\kappa l) & j \sin(\kappa l) \\ i \sin(\kappa l) & \cos(\kappa l) \end{pmatrix} \begin{pmatrix} E_0(f) \\ E_3(f) \end{pmatrix} \quad (2.1)$$

where  $l$  is the coupling length as shown in figure 2.10,  $\beta$  is the propagation constant in each of the two waveguides of the directional coupler,  $\kappa$  is coupling coefficient and is a function of the width of waveguides, the refractive indices of the waveguide core and the substrate, and the proximity of the two waveguides.

A directional coupler is often used with only one active input, say input 0 as in figure 2.10, although it has two input ports and two output ports. In this case, we can get the power transfer function of the coupler from equation (2.1) by setting  $E_3 = 0$

$$\begin{pmatrix} T_{01}(f) \\ T_{02}(f) \end{pmatrix} = \begin{pmatrix} \cos^2(\kappa l) \\ \sin^2(\kappa l) \end{pmatrix} \quad (2.2)$$

Here,  $T_{ij}(f)$  represents the power transfer function from input  $i$  to output  $j$  and is defined by  $T_{ij}(f) = |E_j(f)|^2 / |E_i(f)|^2$ . From equation (2.2), we can see that the directional coupler is a *3-dB coupler* when the coupling length  $l$  satisfies  $\kappa l = (2k+1)\pi/4$ , where  $k$  is a nonnegative integer.

Below are some of the basic specifications of directional couplers [3].

*Splitting ratio or coupling ratio:*

$$\text{Splitting ratio} = \left( \frac{P_2}{P_1 + P_2} \right) \times 100\% \quad (2.3)$$

The two basic loss terms in a coupler are excess loss and insertion loss. The *excess loss* is defined as the ratio of the input power to the total output power. Thus, in decibels, the excess loss for a  $2 \times 2$  coupler is

$$\text{Excess loss} = 10 \log \left( \frac{P_0}{P_1 + P_2} \right) \quad (2.4)$$

The *insertion loss* refers to the loss for a particular port-to-port path. For example, for the path from input  $i$  to output  $j$ , we have, in decibels,

$$\text{Insertion loss} = 10 \log \left( \frac{P_i}{P_j} \right) \quad (2.5)$$

Another performance parameter is *crosstalk*, which measures the degree of isolation between the input power at one input port and the optical power scattered or reflected back into the other input port.

A coupler may have many applications in an optical network. It can be either wavelength selective or wavelength independent. For wavelength independent couplers, one of the common uses is to split optical power. They can also be used to tap off a small portion of the power from a system for monitoring purposes. For wavelength dependent couplers, they are widely used to combine signals with different wavelengths into a single output port or to separate the two signals coming in on a common fiber to different output ports, fulfilling the functions of multiplexing and demultiplexing. One thing should be mentioned when the coupler is used as a 3-dB coupler. Although the electric fields at the two output ports have the same magnitude, they have a relative phase shift of  $\pi/2$ . This characteristic plays a crucial role in the design of devices like Mach-Zehnder Interferometer.

## 2.5.2 Mach-Zehnder Interferometer

Combining two 3-dB couplers together forms a Mach-Zehnder Interferometer (MZI) as shown in figure 2.11. The device can be made either by fiber or by planar waveguides, the latter is more rigid compared to fiber and therefore more stable. Throughout this dissertation, we will only discuss waveguide-based MZIs.

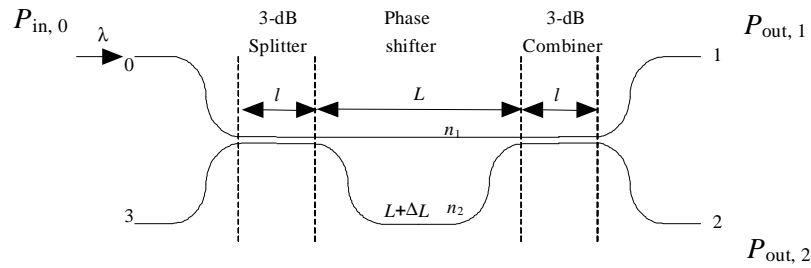


**Figure 2.11** A basic  $2 \times 2$  Mach-Zehnder Interferometer.

The transfer function of the MZI shown in figure 2.11 can be obtained based on the general relationship of a coupler as shown in equation (2.1). Since we are only interested in the relative phase relationships for the transfer function, we can ignore the common phase shift  $e^{-i\beta l}$  at the right hand side of equation (2.1). For a 3-dB coupler, the propagation matrix is

$$M_{\text{coupler}} = \begin{pmatrix} \cos(\kappa l) & j \sin(\kappa l) \\ j \sin(\kappa l) & \cos(\kappa l) \end{pmatrix} = \frac{1}{\sqrt{2}} \begin{pmatrix} 1 & j \\ j & 1 \end{pmatrix} \quad (2.6)$$

As for the central region in figure 2.11, we can see that the phase difference caused by the two waveguides in that region can be expressed as

$$\Delta\phi = \frac{2\pi n_1}{\lambda} L - \frac{2\pi n_2}{\lambda} (L + \Delta L) \quad (2.7)$$

The phase difference can arise either from a different path length ( $\Delta L$ ) or from a difference of refractive indices ( $n_1 \neq n_2$ ). When  $n_1 = n_2 = n_{\text{eff}}$ , we have

$$\Delta\phi = -k\Delta L \quad (2.8)$$

where  $k = 2\pi n_{\text{eff}} / \lambda$ , so the propagation matrix for the phase shifter is

$$M_{\Delta\phi} = \begin{pmatrix} \exp(jk\Delta L/2) & 0 \\ 0 & \exp(-jk\Delta L/2) \end{pmatrix} \quad (2.9)$$

The relationship between the electric fields at the output side,  $E_{\text{out},1}$  and  $E_{\text{out},2}$ , and the electric fields at the input sides of the MZI,  $E_{\text{in},0}$  and  $E_{\text{in},3}$  is

$$\begin{pmatrix} E_{\text{out},1} \\ E_{\text{out},2} \end{pmatrix} = C \cdot M \begin{pmatrix} E_{\text{in},0} \\ E_{\text{in},3} \end{pmatrix} \quad (2.10)$$

where  $C$  is a phase constant, which has  $|C|=1$ , and  $M$  is the overall propagation matrix of the MZI, which is expressed as

$$M = M_{\text{coupler}} \cdot M_{\Delta\phi} \cdot M_{\text{coupler}} = j \begin{pmatrix} \sin(k\Delta L/2) & \cos(k\Delta L/2) \\ \cos(k\Delta L/2) & -\sin(k\Delta L/2) \end{pmatrix} \quad (2.11)$$

From equations (2.10) and (2.11), we can get the output powers in the case of single input (at 0 input port) as

$$P_{\text{out},1} = E_{\text{out},1} E_{\text{out},1}^* = \sin^2(k\Delta L/2) P_{\text{in},1} \quad (2.12)$$

$$P_{\text{out},2} = E_{\text{out},2} E_{\text{out},2}^* = \cos^2(k\Delta L/2) P_{\text{in},1} \quad (2.13)$$

So the transfer function of MZI for single power input at port 0 and two output ports at port 1 and port 2 can be expressed as

$$\begin{pmatrix} T_{01}(\lambda) \\ T_{02}(\lambda) \end{pmatrix} = \begin{pmatrix} \sin^2(\pi n_{\text{eff}} \Delta L / \lambda) \\ \cos^2(\pi n_{\text{eff}} \Delta L / \lambda) \end{pmatrix} \quad (2.14)$$

where  $n_{\text{eff}}$  is the effective refractive index in the waveguide,  $\lambda$  is the wavelength of the input signal,  $\Delta L$  is the difference between the lengths of the two arms in MZI as shown in figure 2.11. This transfer function of equation (2.14) can be depicted in figure 2.12. We see that wavelength  $\lambda_1$  output from port 1 and  $\lambda_2$  output from port 2. Different wavelength signals go to different output ports. From equation (2.14), we can see that switch functionality of the MZI can be realized if we can control or adjust  $\Delta L$ .

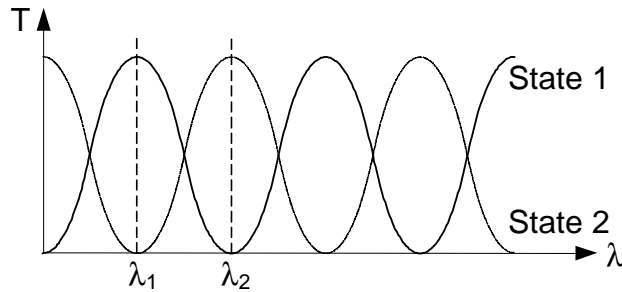


**Figure 2.12** Transfer functions of the basic  $2 \times 2$  Mach-Zehnder Interferometer

It should be noted that figure 2.12 is based on  $n_1 = n_2$ , which means the two arms in the central region of the MZI have the same effective refractive index and the

phase difference between the two arms is expressed in equation (2.8). When  $n_1$  is not equal to  $n_2$ , the result would be different. From equation (2.7), we have

$$\Delta\phi = -\frac{2\pi L}{\lambda} \Delta n - \frac{2\pi n_2}{\lambda} \Delta L \quad (2.15)$$

where  $\Delta n = n_2 - n_1$ . The propagation matrix of the central region has the general form as

$$M_{\Delta\phi} = \begin{pmatrix} \exp(jk\Delta L/2) & 0 \\ 0 & \exp(-jk\Delta L/2) \end{pmatrix} \quad (2.16)$$

Based on equation (2.16), we get the general propagation matrix of the whole MZI as

$$M = M_{\text{coupler}} \cdot M_{\Delta\phi} \cdot M_{\text{coupler}} = j \begin{pmatrix} -\sin(\Delta\phi/2) & \cos(\Delta\phi/2) \\ \cos(\Delta\phi/2) & \sin(\Delta\phi/2) \end{pmatrix} \quad (2.17)$$

So the transfer function of MZI for single power input at port 0 and two outputs at ports 1 and 2 can be expressed as

$$\begin{pmatrix} T_{01}(\lambda) \\ T_{02}(\lambda) \end{pmatrix} = \begin{pmatrix} \sin^2(\Delta\phi/2) \\ \cos^2(\Delta\phi/2) \end{pmatrix} \quad (2.18)$$

From equation (2.15), we can see that we can change either  $\Delta n$  or  $\Delta L$  or both to have different phase difference,  $\Delta\phi$ , between the two arms in the central region of the MZI. From equation (2.18), we see that the output at each output port will be different for each wavelength. This is the basis for our design of an all-optical switch based on the interleaved arrayed waveguide gratings, which will be discussed in Chapter 3.

### 2.5.3 Arrayed Waveguide Grating

An arrayed-waveguide-grating (AWG) is typically used in WDM optical systems as a frequency domain multiplexer, demultiplexer, or a wavelength router.

The wavelength selectivity of an AWG is based on multi-beam interference. Unlike a conventional transmission or reflection grating, an AWG is composed of integrated waveguides deposited on a planar substrate, which is commonly referred to as planar lightwave circuit (PLC). As shown in Figure 2.13, the basic design of an AWG consists of input and output waveguides, two star couplers and an array of waveguides between the two star couplers. The array is composed in such a way that any two adjacent waveguides have the same optical path difference, which satisfies the constructive interference condition for the central wavelength  $\lambda_0$  of the signal. The interference condition for the output signal also depends on the design of the star couplers. For the star coupler, as schematically shown in figure 2.14, the input and the output waveguides are positioned at the opposite side of a Rowland sphere with a radius of  $L_f/2$ , where  $L_f$  is the focus length of the sphere. In an AWG operation, the optical signal is first distributed into all the arrayed waveguides through the input star coupler. After passing through the arrayed waveguides, the signal is diffracted into the output star coupler where each wavelength component of the signal is added up constructively at the appropriate output waveguide. The phase condition of this constructive interference is determined by the following equation [20]:

$$n_c \cdot \Delta L + n_s d \sin \theta_o = m\lambda \quad (2.19)$$

where  $\theta_o = j \cdot \Delta x / L_f$  is the diffraction angle in the output star coupler,  $\Delta x$  is the separation between adjacent output waveguides,  $j$  indicates the particular output waveguide number,  $\Delta L$  is the length difference between two adjacent waveguides in the waveguide array,  $n_s$  and  $n_c$  are the effective refractive indices in the star coupler

and waveguides respectively,  $m$  is the diffraction order of the grating and an integer, and  $\lambda$  is the wavelength.

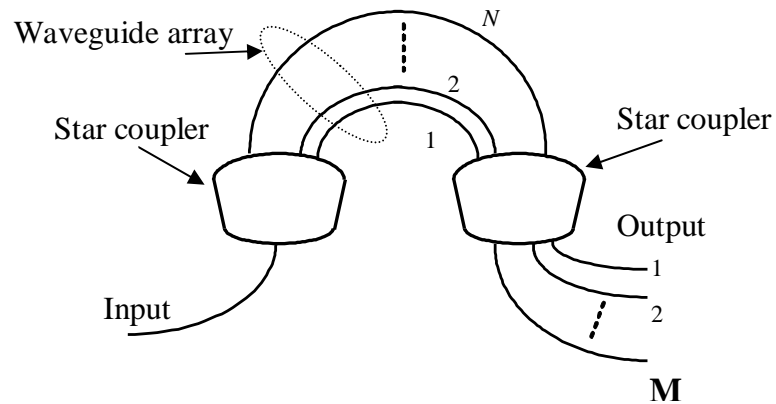


**Figure 2.13** Illustration of an Arrayed Waveguide Grating structure.

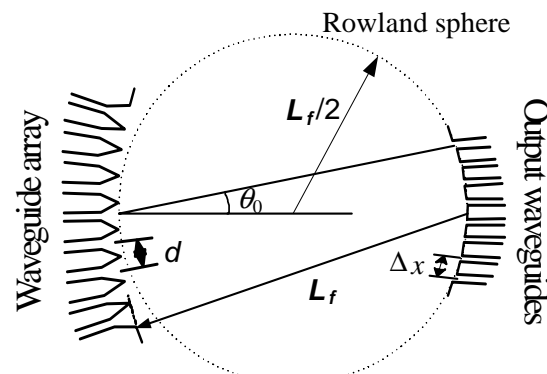


**Figure 2.14** Configuration of the star coupler.

Obviously, from equation (2.19), the constructive interference wavelength at the central output waveguide  $\lambda_0$  is

$$\lambda_0 = \frac{n_c \cdot \Delta L}{m} \quad (2.20)$$

On the other hand, also from equation (2.19), we can easily get the angular dispersion with respect to wavelength  $\lambda$ , in the vicinity of  $\theta_0 = 0$ , as

$$\frac{d\theta}{d\lambda} = -\frac{m}{n_s d} \frac{n_g}{n_c} \quad (2.21)$$

where  $n_g$  is the group index that is defined as

$$n_g = n_c - \lambda \frac{dn_c}{d\lambda} \quad (2.22)$$

Based on equation (2.21), the wavelength separation between two adjacent output waveguides can be found as:

$$\Delta\lambda = \frac{\Delta x}{L_f} \left( \frac{d\theta_0}{d\lambda} \right)^{-1} = \frac{\Delta x}{L_f} \frac{n_s d}{m} \frac{n_c}{n_g} = \frac{\Delta x}{L_f} \frac{\lambda_0 d}{\Delta L} \frac{n_s}{n_g} \quad (2.23)$$

Since AWG is based on multi-beam interference, the spectral resolution of the output signal is primarily determined by the number of the arrayed waveguides between the two star couplers. A larger number of waveguides provides better spectral resolution.

## 2.6. Optical Switches

From figure 2.7 and figure 2.9, we can see that OADMs and OXCs are essentially optical switches in a general sense. Optical networks rely heavily on the

functionalities of all kinds of optical switches. Different applications in an optical network require different switch times and numbers of switch ports. The switching applications in an optical network include provisioning, protection switching, packet switching and external modulation [1]. The required switch times range from milliseconds to picoseconds. The number of switch ports may vary from two ports to several hundreds to thousands of ports.

In addition to the switching time and number of ports, there are other important parameters to be considered for optical switches. Those parameters include extinction ratio, insertion loss, crosstalk, and polarization-dependent loss (PDL). The extinction ratio is the ratio of the output power in the “on” state to the output power in the “off” state. The insertion loss is the power lost because of the presence of the switch. The crosstalk is the ratio of the power at the output port from the desired input to the power at the same output port from all the other inputs. PDL is due to the loss in some components depending on the polarization state of the input signal.

For large optical switches, the considerations should include the number of switch elements required, loss uniformity, the number of waveguide crossovers and blocking characteristics, etc. Large switches consist of multiple switch elements and the number of the elements is an important factor that determines the cost and the complexity of the switch. It is also desired to achieve uniform loss for different input port and output port combinations in an optical switch. For integrated optical switches using planar lightwave circuits, the connections between components must be made in a single layer by means of waveguides and this will cause crossovers between

waveguides in some architectures, which causes power loss and crosstalk. Less waveguide crossovers ensure better performance for an optical switch. As for the definition of blocking or nonblocking of a switch, the switch is said to be nonblocking if any unused input port can be connected to any unused output port. Otherwise, the switch is blocking.

### 2.6.1 Large Optical Switch Architectures

#### 2.6.1.1 Crossbar

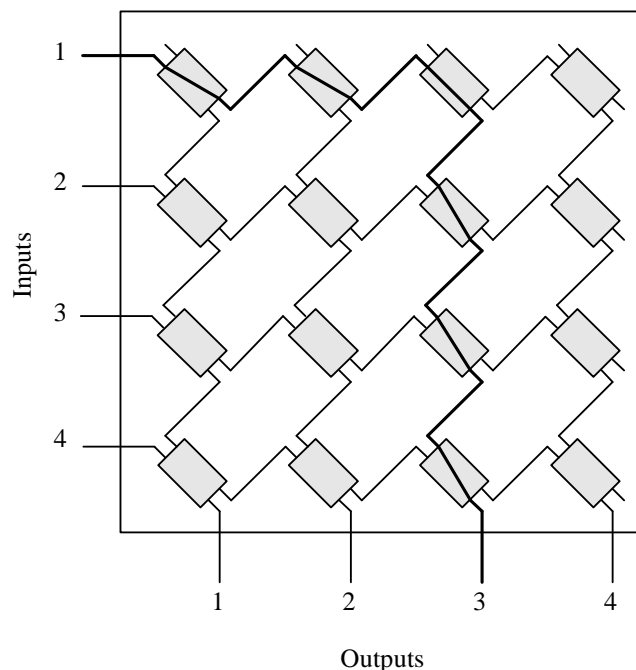


**Figure 2.15** A  $4 \times 4$  crossbar switch realized using 16  $2 \times 2$  switches. (after [1])

There are several large optical switch architectures proposed so far. The basic one is called Crossbar. The crossbar architecture consists of a group of  $2 \times 2$  switches and is, in general, nonblocking. An  $n \times n$  crossbar requires  $n^2$   $2 \times 2$  switches. The shortest path length is 1 and the longest path length is  $2n - 1$  in this architecture. This large path length difference is one of the main drawbacks of this architecture since the loss distribution will not be uniform. Figure 2.15 shows a  $4 \times 4$  crossbar switch, which uses 16  $2 \times 2$  switches. The settings of the  $2 \times 2$  switches for the connection from input port 1 to output port 3 is shown in the figure. As we can see, the switch can be fabricated without any crossovers between waveguides.

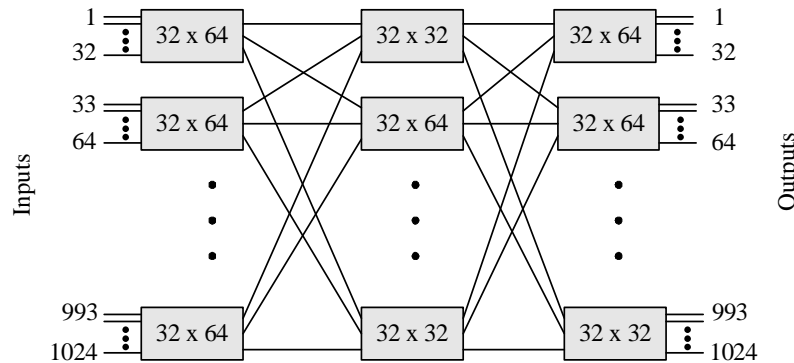


**Figure 2.16** A strict-sense nonblocking three-stage  $1024 \times 1024$  Clos architecture switch. (after [1])

### 2.6.1.2 Clos

The second optical switch architecture introduced here is called Clos, which provides a strict-sense nonblocking switch and is widely used in practice to build large port count switches. Figure 2.16 shows a three-stage 1024-port Clos switch. The architecture has loss uniformity between different input-output combinations and the number of required switch elements is significantly reduced compared to the crossbar architecture.

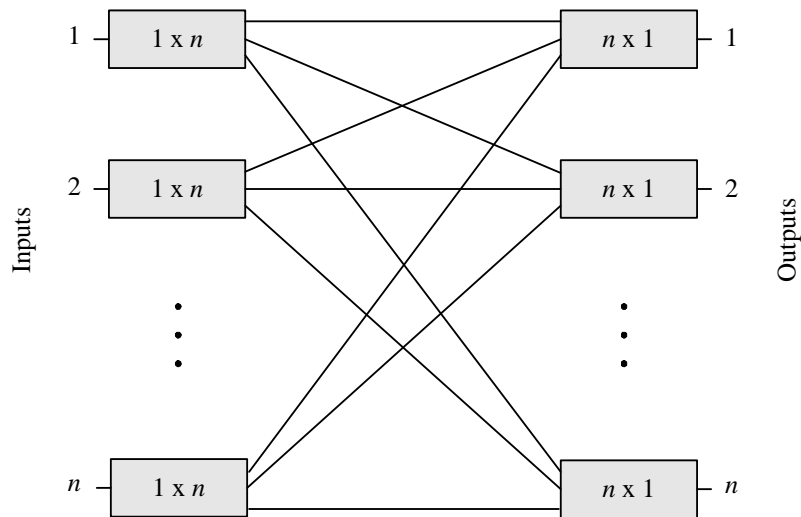


**Figure 2.17** A strict-sense nonblocking Spanke architecture  $n \times n$  switch. (after [1])

### **2.6.1.3 Spanke**

Figure 2.17 shows another switch architecture which is called Spanke. The Spanke architecture is very popular for building large switches. It can be seen from the figure that an  $n \times n$  switch consists of  $n 1 \times n$  switches at the input side and  $n n \times 1$  switches at the output side. This is also a strict-sense nonblocking architecture. Instead of counting the number of  $2 \times 2$  switches, a  $1 \times n$  switch or an  $n \times 1$  switch can be made from a single switch unit, which reduces the cost significantly. Also it is obvious that all connections only pass through two switch elements, which provides much lower insertion loss than the multistage designs. Moreover, the optical path length between any two-switch combinations can be made exactly the same so that the loss uniformity can be realized.

Besides the architectures mentioned above, there are other switch architectures such as Beneš and Spanke- Beneš. These architectures both have their unique advantages and disadvantages. More details can be found from [1].

## **2.6.2 Optical Switch Technologies**

There are many different technologies to realize optical switches, such as Bulk Mechanical Switches, Micro-Electro-Mechanical System (MEMS) Switches, Thermo-Optic Silica Switches, Bubble-Based Waveguide Switches, Liquid Crystal Switches, Electro-Optic Switches, and Semiconductor Optical Amplifier Switches, etc [1]. Here we will particularly introduce the MEMS since this type of switch is very popular and still developing. Also, MEMS are widely used in current optical communication systems. Then we will briefly introduce the Thermo-Optic Switch

since it will easily lead us to the switch mechanism and architecture proposed in this dissertation.

### 2.6.2.1 Micro-Electro-Mechanical System (MEMS) Switches

Micro-Electro-Mechanical Systems (MEMS) is the integration of mechanical elements, sensors, actuators, and electronics on a common silicon substrate through micro-fabrication technology [21]. In the context of optical switches, MEMS usually refers to miniature movable mirrors fabricated in silicon, with dimensions ranging from a few hundred micrometers to a few millimeters [1]. By using standard semiconductor manufacturing processes, arrays of micro mirrors can be made on a single silicon wafer. These mirrors can be deflected to face different directions by using techniques such as electromagnetic, electrostatic, or piezoelectric methods.

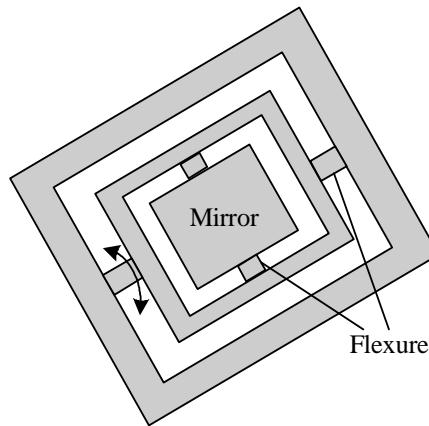


**Figure 2.18** An analog beam steering mirror. (after [1])

There are many different mirror structures that can be used. The simplest mirror structure is a 2D mirror, which can deflect between two positions. However 3D mirrors are more flexible, but fabrication is more complicated. Figure 2.18 shows a 3D mirror structure. By rotating the mirror on two distinct axes (flexures), the mirror can be turned to face any desired direction. This characteristic can be used to realize  $1 \times n$  switch function.

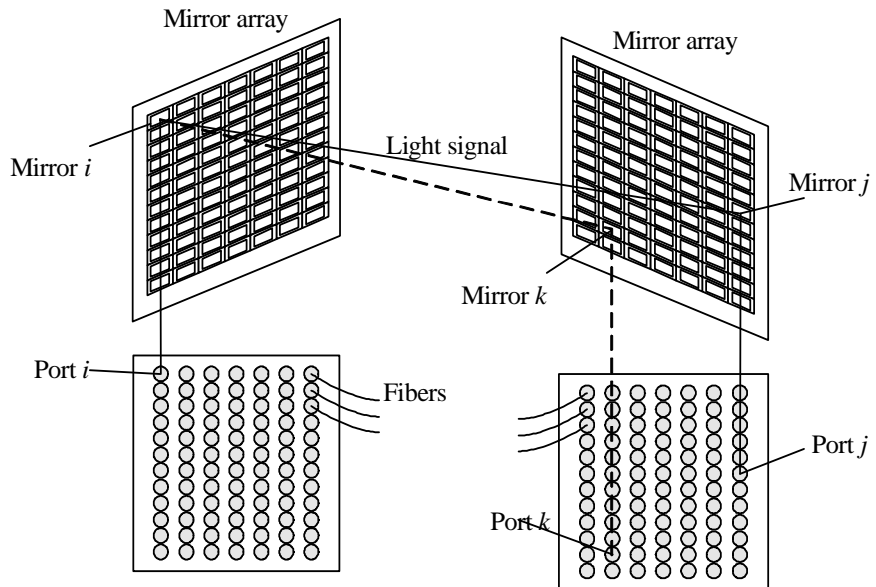


**Figure 2.19** An  $n \times n$  switch built using two arrays of analog beam steering MEMS mirrors. (after [1])

Figure 2.19 shows a large  $n \times n$  switch by using two arrays of analog beam steering mirrors. One can see that this structure corresponds to the Spanke

architecture as was mentioned above. Each array has  $n$  mirrors and each mirror is associated with one port. At the input side, a signal is coupled to the associated mirror, which can be deflected to face any of the mirrors in the output array. To make a connection from port  $i$  to port  $j$ , one can deflect both mirror  $i$  and mirror  $j$  so that they point to each other. The signal is coupled to mirror  $i$  from the input port  $i$  at input side and coupled to output port  $j$  from mirror  $j$  at the output side. If one wants to switch from the output port  $j$  to output port  $k$ , one can simply deflect mirrors  $i$  and  $k$  so that they face each other. In this process, the beam from mirror  $i$  will scan over some other mirrors in the output array. But this will not cause additional crosstalk since there is no connection established before the two mirrors point to each other.

MEMS switches are very popular right now. This 3D MEMS analog beam steering mirror technology provides many advantages for optical switch construction. The switch can have compact size, low loss, good loss uniformity, negligible dispersion, no interference between different beams, extremely low power consumption and has the best potential for building large-scale optical switches. However, mechanical optical switches have intrinsic problems such as limited lifetime, large size (compared to WDM optical technology) and most importantly relatively slow switching speed. They have switch times around 10 ms. This switch time may be enough for optical circuit switch but not for optical packet switch, which requires switching time at nanosecond level, and this probably can never be done by any mechanical means.

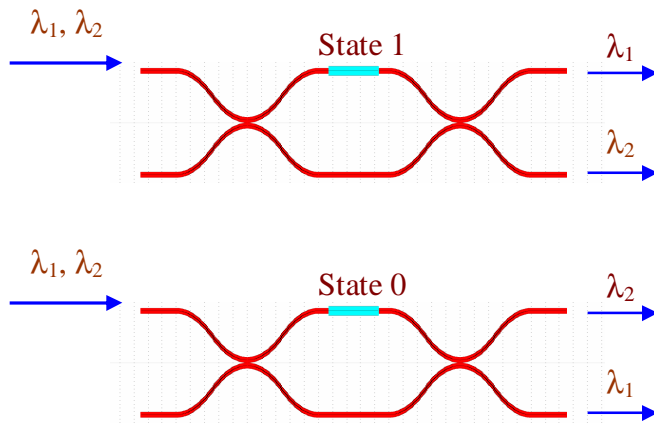


**Figure 2.20** Mach-Zehnder Interferometer As Thermo-Optical Switch.

### 2.6.2.2 Thermo-Optic Switches

Another approach to making an optical switch is to use thermo-optic technology. The simplest thermo-optic switch is essentially an integrated optical Mach-Zehnder Interferometer (MZI). The MZI is composed of optical waveguides whose refractive index is a function of the temperature. Instead of changing the length of one arm, the refractive index of the optical waveguide of one arm is changed by varying the temperature of the waveguide. This change of refractive index has been discussed in section 2.5.3. In this way, the relative phase difference between the two arms can be adjusted so that the input signal can be switched from one output port to the other. Figure 2.20 shows this thermo-optic switch, which usually is made by silica or polymer waveguides. The shortcoming of the thermo-optic switch, however, is its relatively poor crosstalk. Also, the speed of thermal tuning is relatively slow in the

millisecond level, which is obviously not fast enough for optical packet switch applications.

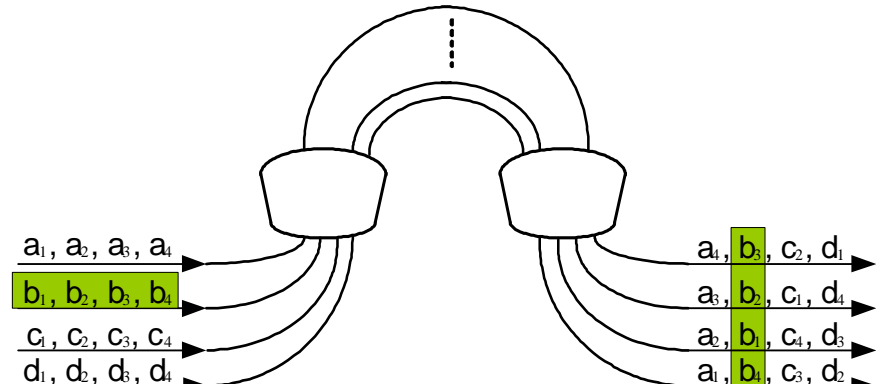
## 2.7. WDM Optical Switches

So far, we have introduced optical network architectures, WDM network elements, basic optical components and some optical switch structures. Now we are going to discuss the design of optical switches based on WDM optical technologies. In this section, we would rather discuss this topic in a more general way, including the designs of wavelength routers, filters, ADMs and all-optical switches.

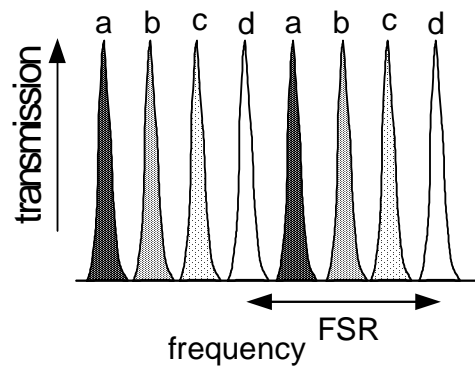
### 2.7.1 Design of Passive Waveguide Devices

#### 2.7.1.1 Design of Passive AWG Wavelength Routers

Wavelength routers based on planar lightwave circuits were first reported by Dragon [22][23]. The concept can also be used to design devices such as add-drop multiplexers and wavelength switches [8]. Figure 2.21 illustrates the functionality of an  $N \times N$  wavelength router. The router has  $N$  input and  $N$  output ports. Each  $N$  input port carries  $N$  different frequencies (or wavelengths). The  $N$  frequencies carried by input port 1 are distributed among output ports 1 to  $N$  in such a way that output port 1 carries frequency  $N$  and port  $N$  frequency 1. The  $N$  frequencies carried in port 2 are distributed in the same way except that they were cyclically rotated by 1 port compared with the ones distributed from input port 1, as shown in the figure. In this way each output port receives  $N$  different frequencies, one from each input port.



(a)



(b)

**Figure 2.21** Schematic diagram illustrating the operation of a wavelength router: (a) Interconnectivity scheme ( $a_i$  denotes the signal at input port  $a$  with frequency  $i$ ); and (b) Frequency response. (FSR= Free Spectral Range) (After Ref. [8])

The wavelength router is obtained by designing the input and the output side of AWG symmetrically, i.e., with  $N$  input and  $N$  output ports. For the condition of cyclical rotation of the input frequencies along the output ports, it is essential that the frequency response is periodical as shown in figure 2.21(b), which implies that the

FSR should be equal to  $N$  times the channel spacing. This can be obtained by choosing [8]

$$\Delta L = \frac{c}{n_g N \Delta f_{ch}} \quad (2.24)$$

where  $\Delta L$  is the length difference between adjacent arrayed waveguides,  $n_g$  is the group index of the waveguide mode,  $N$  is the number of frequency channels and  $\Delta f_{ch}$  is the channel spacing.

The advantage of this device is that it routes wavelength signals fast and in fixed paths. Also the device is compact and passive. The disadvantage is the lack of the switching capability and it can handle only a limited number of wavelength channels.

### **2.7.1.2 Passive Wavelength-Selective Switches and Add-Drop Multiplexers (ADM)**

AWG can be applied to design add-drop multiplexers that were introduced earlier in this chapter. Figure 2.22(a) shows a configuration of this application, which was proposed in [24]. This design is basically a single AWG  $N \times N$  multiplexer but with loop-back optical paths connecting each output port with its corresponding input port. One input port and its corresponding output port are reserved as common input and output ports for the transmission line. After the signals with  $N$  equally spaced wavelengths are applied into the common input port, they are first demultiplexed into the  $N$  output ports and then  $N-1$  output signals are looped back to the opposite input ports and automatically multiplexed again into the common output port. This

functionality is guaranteed due to its symmetric design of AWG  $N \times N$  router with  $N$  input ports and  $N$  output ports. Wavelength add/drop is accomplished with a  $2 \times 2$  switch on each loop back path.

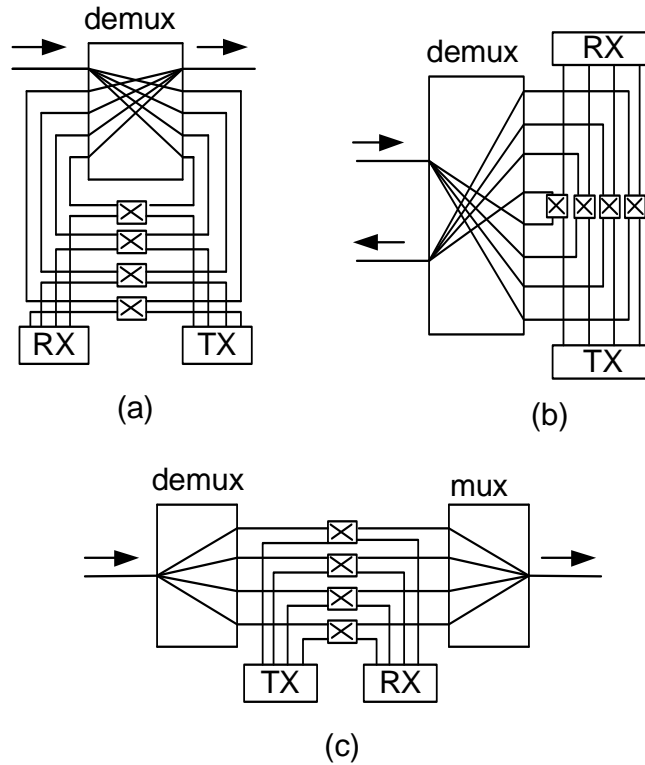


**Figure 2.22** Three different ADM configurations: (a) loop-back, (b) fold-back, and (c) cascaded demux/mux. (After Ref. [6])

An inevitable disadvantage of the loop-back configuration is the crosstalk of the input signals coupled directly into the main output port. This problem can be solved by a fold-back configuration that is shown in figure 2.22(b) [25], where the

crosstalk cannot directly reach the output port since it is on the same side as the input port.

A third approach of ADM with AWG is shown in figure 2.22(c), where two separate AWG multiplexers are used. The requirements of this configuration are to put the two AWG multiplexers close enough and to make sure that they have identical transfer functions for the interested wavelength range. Compare this configuration with the two other configurations shown above, we see that those other two configurations do not have this AWG transfer function match requirement since there is only one AWG multiplexer used in both cases.

### **2.7.2 Design of Carrier Controlled Simple Waveguide Devices**

In planar lightwave circuits, the optical waveguides can be made with semiconductor materials. The refractive indices of the waveguides can be tuned through carrier injection. In this way, electrically controlled optical phase shift can be introduced and the tuning speed can be faster.

#### **2.7.2.1 Proposed Carrier Controlled Mach-Zehnder Interferometer Optical Switch**

Here we use figure 2.20 again. It shows a Mach-Zehnder interferometer structure that is used as a simple optical switch or wavelength router. Instead of changing the phase delay between two optical arms by thermal method as we discussed above, we can make the Mach-Zehnder interferometer with semiconductor materials and change the refractive index of one of the arms through carrier injection.

The detailed mechanism of carrier-induced index change will be discussed in Chapter 4. Here we only introduce several optical circuit configurations that utilize this effect.

### 2.7.2.2 Ladder-Type Carrier Controlled Tunable Wavelength Filter

A novel InGaAsP-InP based tunable filter with a ladder-type structure was proposed by Matsuo *et al* [26]. The device consists of multiple multi-mode interference (MMI) couplers, a waveguide array (crossing waveguides), and input and output waveguides. The electrodes with the same length are put on the input and output waveguides as shown in figure 2.23. Each crossing waveguide is connected to the input and output waveguides through MMI couplers. The lights from the output waveguide and from the crossing waveguide interfere in the coupler that combines them.

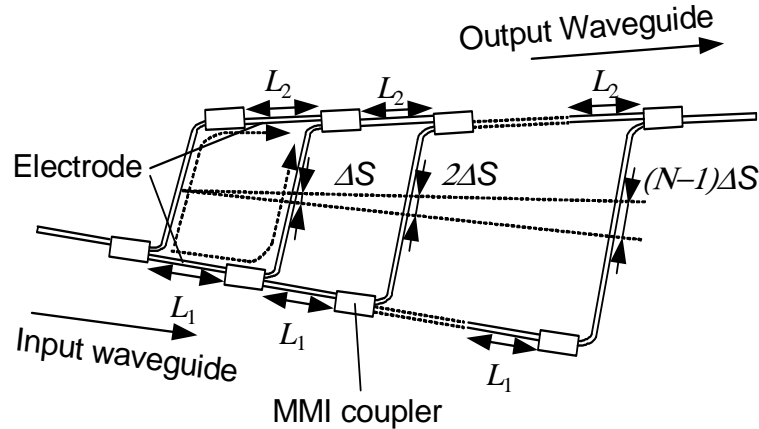


**Figure 2.23** Schematic diagram of a tunable filter with a ladder-type structure.  
(Ref. [26])

The crossing waveguides are designed such that the length difference between two adjacent waveguides is  $\Delta S$ . Let  $L_1 = L_2$  and all the couplers have the same length. Then all the couplers in the output waveguide have the same transmission peak wavelength. The peak wavelength of the filter is

$$\lambda_0 = \frac{n_{\text{eff}} \Delta S}{m} \quad (2.25)$$

where  $n_{\text{eff}}$  is the effective refractive index of the waveguide and  $m$  is the diffraction order. The diffraction order strongly affects the 3-dB bandwidth of the filter in the way that the 3-dB bandwidth becomes narrower when it is increased.

When the refractive index in the input waveguide is reduced by carrier injection, the optical path difference (OPD) between the output waveguide and the crossing waveguides decreases. According to equation (2.25), this makes the peak wavelength shorter. Similarly, reducing the refractive index in the output waveguide increases the OPD, which makes the peak wavelength longer. The peak wavelength change is given by

$$\Delta\lambda_0 = \frac{\Delta n_{\text{eff}} L_{1\text{or}2}}{m} \quad (2.26)$$

where  $\Delta n_{\text{eff}}$  is the change of refractive index caused by carrier injection. So the actual tunable wavelength range is  $2(\Delta\lambda_0) = 2(\Delta n_{\text{eff}})L_{1\text{or}2}/m$ . Equation (2.26) indicates that increasing  $L_1$ ,  $L_2$  or  $\Delta n_{\text{eff}}$  increases the wavelength shift while increasing of diffraction order decreases the shift. As it was pointed out above that a large diffraction order means a sharp peak in transfer function, there is a trade off between a narrow 3-dB

bandwidth and a wide tunable wavelength range. Also, there is a limitation in increasing  $L_1$  and  $L_2$  when the size of a practical device is considered.

The InGaAsP-InP material tunable filter with a ladder-type structure proposed by Matsuo has 15 crossing waveguides and a diffraction order of  $m = 20$ . The free spectral range (FSR) is 74.4 nm and the total tunable range is 58 nm. The switching time for two particular wavelengths that correspond to injecting currents 0 and 20 mA is less than 10 ns.

The crucial points for the design of this kind of filter include the proper power distribution of MMI (or waveguide-made) couplers and the optimum number of crossing waveguides in the whole device. These are very important since the interference conditions have to be satisfied.

### 2.7.2.3 Proposed Carrier Controlled Semiconductor AWG Tunable Filter

Widely tunable optical filters are needed in local area networks or tunable light source applications [26]. As we have mentioned before, each semiconductor material can have its refractive index changed with carrier injection. By using this property of semiconductor material, we can also design carrier controlled AWG filters.

#### A. Single-Wavelength Filter

Here we consider an AWG with one input and one output waveguide, as shown in figure 2.24(a), where  $\lambda_0, \lambda_1, \lambda_2, \dots, \lambda_n$  are the input wavelengths among which  $\lambda_0$  is the central wavelength. To be convenient, both central waveguides in the

input side and output side of the previous design are chosen as the input port and output port. Based on the previous analysis in section 2.5.3, it is quite obvious that the output wavelength would be the central wavelength  $\lambda_0$  designed for this device. All the other wavelengths are filtered out.

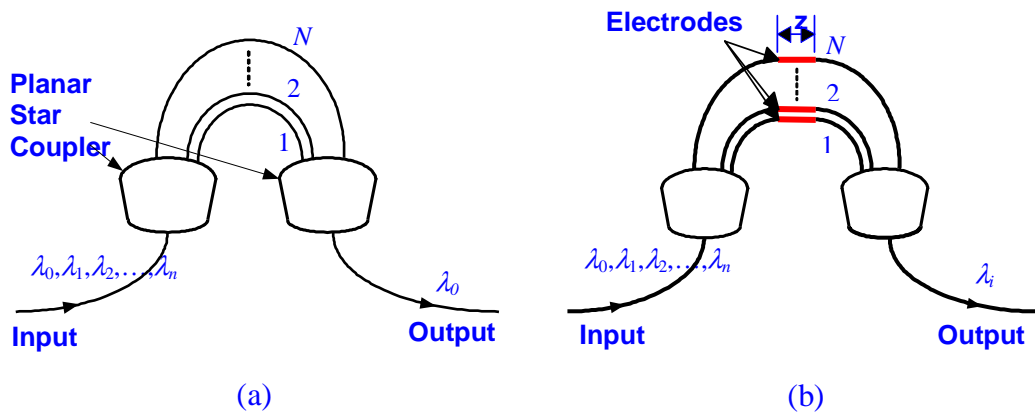


**Figure 2.24** (a) AWG Functioning As a Filter. (b) Electrode Controlled AWG Filter.

### B. Same Length Electrode Controlled AWG Tunable Filter

The output wavelength for the filter in figure 2.24(a) is fixed ( $\lambda_0$ ). To realize an adjustable wavelength filter, we can add electrodes to the arrayed waveguides in the design as shown in figure 2.24(b). We first consider the case when all the electrodes have the same length and let this length be  $z$ . As we know, the effective refractive index of arrayed waveguides will be changed after electrical voltages are

applied to the electrodes. Let the change of the refractive index of waveguide  $j$  among  $N$  arrayed waveguides be  $dn_{cj}$ , and also control the current injection in such a way that

$$\Delta dn_{cj} = dn_{cj} - dn_{c(j-1)} = \text{constant} \quad (2.27)$$

for all  $j$ ,  $j = 1, 2, \dots, N$ , where  $\Delta dn_{cj}$  is the difference between the changes of effective refractive indices of two adjacent arrayed waveguides. We denote this constant as

$$\Delta dn_c$$

$$\Delta dn_c = \Delta dn_{cj} \quad (2.28)$$

Thus based on equation (2.19), we can get the new equation of AWG that satisfies the phase match condition with current injection for this design

$$n_c \cdot \Delta L + \Delta dn_c \cdot z = m\lambda' \quad (2.29)$$

where  $\lambda'$  is the wavelength that passes the filter. Compare equation (2.29) with equation (2.20), we can get

$$\Delta dn_c \cdot z = n_c \cdot \Delta L \cdot (\lambda' - \lambda_0) / \lambda_0 = -n_c \cdot \Delta L \cdot (1 - \lambda' / \lambda_0) \quad (2.30)$$

where  $\lambda_0$  is the designed central wavelength. We see that the signal with wavelength  $\lambda'$  will pass the filter after electrical voltages are applied to the electrodes and equation (2.30) is satisfied, while all the signals with other wavelengths will be blocked.

### C. Different Length Electrode Controlled AWG Tunable Filter

We can also design electrodes with different lengths  $z_j$ . This is shown in figure 2.25, where the lengths of electrodes are designed as

$$z_1 - z_2 = z_2 - z_3 = \dots = z_{n-1} - z_n = \Delta z \quad (2.31)$$

We can design both  $\Delta z > 0$  (figure 2.25(a)) and  $\Delta z < 0$  (figure 2.25 (b)). Since we know that the carrier-induced change of refractive index is negative, which will be shown in Chapter 4, the first design shown in figure 2.25(a) actually increases the OPD between two adjacent arrayed waveguides while the second design shown in figure 2.25(b) decreases the OPD.

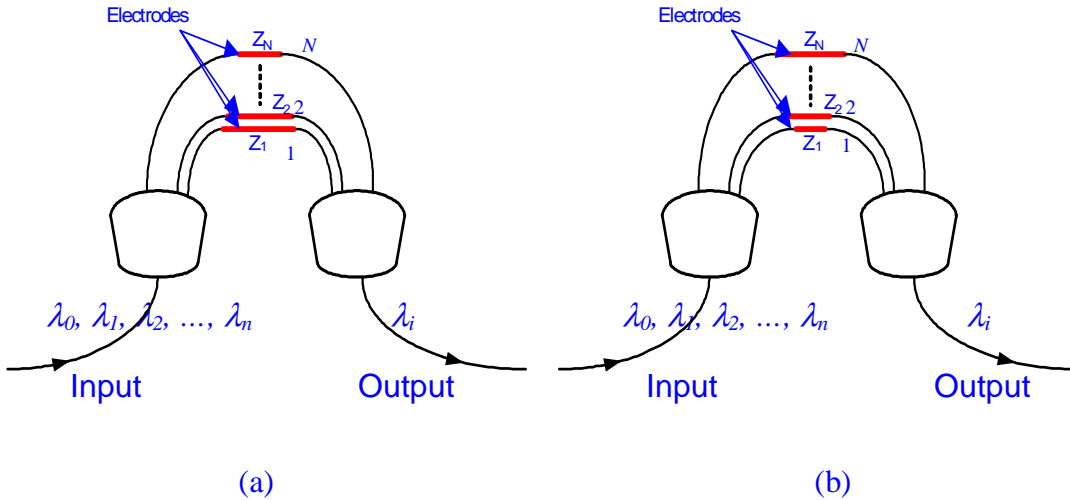


**Figure 2.25** Electrode Controlled AWG Filter, with different lengths of electrodes.

In both cases, the optical path length (OPL) of a particular ( $j$ -th) waveguide in the waveguide array is

$$OPL_j = n_c L_j + \Delta n_{cj} \cdot z_j \quad (2.32)$$

where  $n_c$  is the effective refractive index in the arrayed waveguides,  $L_j$  is the length of  $j$ -th waveguide,  $\Delta n_{cj}$  is the change of the refractive index after carrier injection is

applied. For simplicity, we can let  $\Delta n_{cj} = \Delta n_c = \text{constant}$ . Under this condition, we can get the new equation of AWG that satisfies the phase match condition with carrier injection for this design as

$$n_c \cdot \Delta L - \Delta n_c \cdot \Delta z = m\lambda' \quad (2.33)$$

where  $\Delta z$  is defined in equation (2.31). Compare equation (2.33) with (2.20), we have

$$-\Delta n_c \cdot \Delta z = m \cdot (\lambda' - \lambda_0) = \frac{n_c \cdot \Delta L}{\lambda_0} \cdot \Delta \lambda \quad (2.34)$$

where  $\Delta \lambda = \lambda' - \lambda_0$ . Thus

$$\Delta \lambda = -\frac{\Delta n_c}{n_c} \cdot \frac{\Delta z}{\Delta L} \cdot \lambda_0 \quad (2.35)$$

Equation (2.35) gives the wavelength range of the filter. As an example, for GaN material that we will discuss in Chapter 5, we have  $n_c = 2.312$ ,  $\Delta n_c = -0.18$  at  $\lambda_0 = 1550$  nm and carrier density  $N = 6 \times 10^{19} \text{ cm}^{-3}$ . For our designed AWG, we have  $\Delta L$  equal to  $64.79 \mu\text{m}$ . If we take  $\Delta z = 75 \mu\text{m}$ , then  $\Delta \lambda$  is about 140 nm.

From equation (2.35), we see that the larger is  $\Delta z$ , the larger will  $\Delta \lambda$  be. Compare the two designs in figure 2.25, it is shown that figure 2.25(b) gives a better design for wide range adjustable filter since it is easier to realize a large  $\Delta z$  in this design.

### 2.7.3 Design of Carrier Controlled AWG All-Optical Switch

Making devices with functionality of all optical switching is the final goal of this research. Currently we only focus on the designs based on AWG structures.

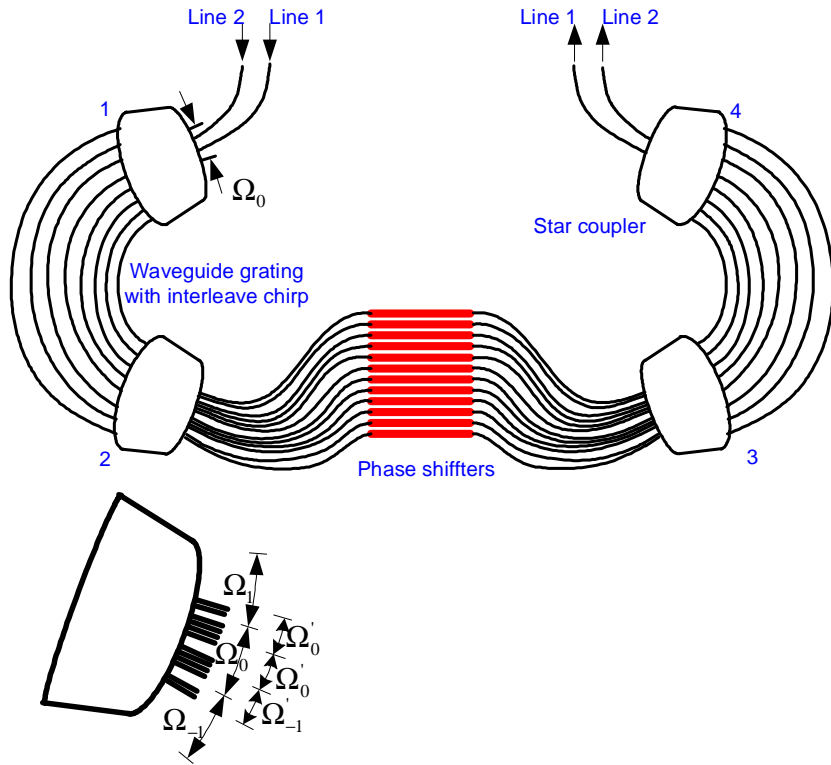


**Figure 2.26** Schematic diagram of the interleave cross connect. The inset in the lower left corner illustrates the Brillouin zones for star coupler 2. (Ref. [27])

### 2.7.3.1 Carrier Controlled Wavelength All-Optical Switch

A device consisting of two interleave-chirped AWG routers connected by waveguides with phase shifters was proposed by Doerr [27]. Figure 2.26 shows an example with two lines inputs and two lines outputs for this configuration. In the example, the interleave chirp consists of adding an additional path length of  $\lambda_c/4$  on every other grating arm, where  $\lambda_c (= \lambda_c/n)$  is the wavelength of interest in the waveguide. In general, an AWG router forms a radiation pattern on the output surface

of the output star coupler by the signals from arrayed waveguides. The radiation pattern has angular Brillouin zones  $\Omega_i$  of order  $i$  and width  $2\gamma$ . The width of the Brillouin zone is equal to the angular period of the radiation pattern formed by the point sources put at the star coupler interface replacing the arrayed waveguides. When every other grating arm has an additional path length  $\lambda_c/4$ , two images are formed in each Brillouin zone  $\Omega_i$ . The inset in figure 2.26 shows a four-channel application, where two images with each having four channels are formed in Brillouin zone  $\Omega_0$ . So the FSR is reduced by a factor 2. New Brillouin zones  $\Omega'_i$  are defined as shown in the figure.

The images are collected by the nominal equal-length waveguides with phase shifters. As shown in the figure, only  $\Omega'_{-1}$ ,  $\Omega'_1$  and  $\Omega'_0$  are connected since they contain almost all the power. The two input lines on the other side of input star coupler 1 are separated by  $\gamma$  and so are the two output lines on output star coupler 4. A channel entering one of the input ports can be switched into either one of the two output ports by controlling the relative phases in the three connecting waveguides for this channel. For example, channel 1 is controlled by phase shifters 3, 7 and 11 (counted from bottom to top). The switching is actually based on a generalized Mach-Zehnder interferometer, consisting of the waveguides in the two AWG arrays and the connecting waveguides.

The switching is actually a swap of the same channel in two input lines. If a channel from input line 1 is switched into output line 2, then the same channel from input line 2 has to be switched into output line 1. However, if one does not keep the

same channels (wavelengths) in different input lines, one can realize the full scale switching. For example, if we put channel 1 ( $\lambda_1$ ) and 2 ( $\lambda_2$ ) in input line 1 and channel 3 ( $\lambda_3$ ) and 4 ( $\lambda_4$ ) in input line 2, we can switch any channel to either output lines by controlling the relative phase shifters for that channel.

So far, this device has been demonstrated for 2 lines  $\times$  2 lines, 6 channel  $\times$  200 GHz spacing in InP [28]. We will focus on GaN/AlGaN material applications for 2 lines  $\times$  2 lines switching of the signals with same wavelength. Then, we will do explorations in  $N \times N$  ( $N > 2$ ) applications for the switching of the signals with different wavelengths in each line. In a similar way, devices with  $N$  ( $N > 2$ ) input ports and  $N$  output ports can be designed by employing an interleave chirp in each AWG router to produce  $N$  images in each  $\Omega_i$  with enough waveguides to collect all of them. If the channels or wavelengths in any input line are different than the channels in any other lines, one can switch any channel in any line to any other lines by adjusting the phase shifters properly. By doing this, an all-optical wavelength switch is realized.

A  $1 \times N$  Wavelength Switch can be realized with the same method as mentioned above. A switch with 1 input and 8 outputs will be investigated. The input part consists of only one input port instead of  $N$  input ports. The  $N$  channels with  $N$  different wavelengths all are inputted through the common input port. By adjusting the corresponding phase shifters, any wavelength channel can be switched to any one of the  $N$  output ports. The details of this design will be discussed in Chapter 3.

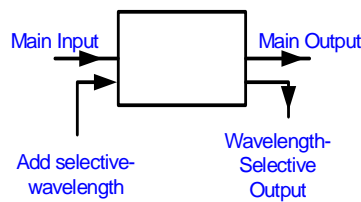
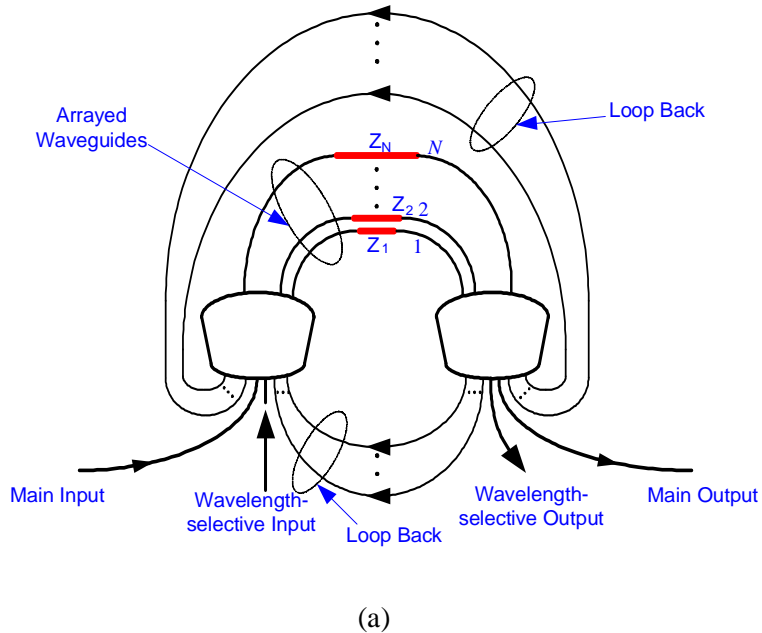


**Figure 2.27** Carrier Controlled Loop-Back Add-Drop Switch. (a) Schematic Diagram, (b) Corresponding Black Box.

### 2.7.3.2 Carrier Controlled Wavelength Add-Drop Switch

Based on the previous review, we propose a carrier controlled loop-back add-drop switch as shown in figure 2.27. The device is based on the ideas of passive

wavelength-selective switches and add-drop multiplexers in section 2.7.1 and carrier controlled semiconductor AWG filter in section 2.7.2. Figure 2.27(a) shows this design. In the figure, all the outputs except for the main output and the one next to main output are connected with their corresponding inputs. With the control of electrodes applied to the arrayed waveguides, one can get the specific selected wavelength signal at the wavelength-selective output, while all the other signals from main input will be all transferred into the main output because of the symmetric design of the AWG device.

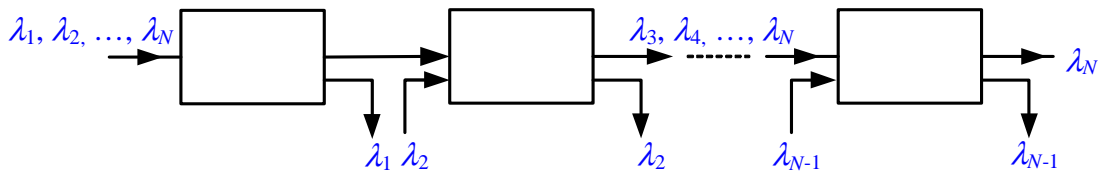


**Figure 2.28**  $1 \times N$  Wavelength Switch Network.

## 2.8. Design of All-Optical Switch Networks

After investigating the single pieces of the devices in section 2.7.3, it is worth doing further research in the designing of switch networks. For example, we can design a  $1 \times N$  switch network as in figure 2.28, where the switch block is the one shown in figure 2.27(b). One can compare the functionality of this design with the one in section 2.7.3.1.

Since we would have  $2 \times 2$  switch for same wavelength channels and  $N \times N$  switches for different wavelength channels, it would be reasonable to do further investigations to realize any wavelength  $N \times N$  switching.

## 2.9. Conclusion

In this chapter, we started from the introduction of telecommunications network architecture. Then we gave a brief introduction of the second generation of optical networks, discussed the network elements and their applications. To realize the functionalities of those elements, especially the OXC, we reviewed the basic components and their applications in an optical network. Then we briefly introduced some large optical switch architectures and technologies. Based on that, we particularly reviewed the principles of AWG and its applications. After that, we proposed some possible architectures that can be realized with AWG principles.

### **3. Design of WDM Cross Connect Based on Interleaved AWG (IAWG) and a Phase Shifter Array**

#### **3.1. Introduction**

In the previous chapter, we have discussed that wavelength division multiplexing (WDM) technique has been widely applied in the fiber-optic networks, it effectively utilizes wide wavelength windows of the fiber and provides an additional degree of freedom in optical networking [3]. In WDM systems, it is critical to develop optical devices that can optically route wavelength channels from any input port to any output port and thus to fully realize non-blocking  $N \times N$  optical switch functionality.

In chapter 2, we have briefly introduced arrayed waveguide gratings (AWG), which have been used as WDM optical multiplexers (MUX) and demultiplexers (DEMUX). In practical applications, refractive index tuning of arrayed waveguides between the two star couplers in an AWG has been introduced to adjust and optimize the transfer function of the device and it can also be used to perform WDM switching with proper device structure design [6][7][29]. In silica-based AWGs, this index tuning can be accomplished by locally heating each individual waveguide branch. However this thermal coefficient-based tuning is usually too slow for an optical packet switch. To overcome the speed limit of thermal tuning, AWG devices are also made by semiconductor materials, such as GaAs and InP. In these devices, refractive indices of branch waveguides can be changed by carrier injection. In general, the

speed of carrier-induced index change can be in the order of sub-nanosecond, which is many orders of magnitude faster than thermal tuning and therefore it can potentially be used to support an all-optical packet switch in the future.

In chapter 2, we have reviewed several different designs and device structures, which have been proposed to realize AWG-based optical switches [6][7][27], where a unique waveguide-interleaved-AWG (IAWG) structure was used. A  $2 \times 2$  non-blocking wavelength switch was demonstrated by using this approach and it can be expanded to realize the switch size of  $N \times N$ . However, this  $N \times N$  switch illustrated in [6] is not truly “any-to-any”, instead it is in a cyclical fashion [27], therefore, a truly any-to-any non-blocking optical switch cannot be directly realized using the structure proposed in [27]. In addition, a general design rule of interleaved AWGs is not available so far, although it is necessary in the designing of different IAWGs. Also, from a switch architecture point of view, a truly any-to-any  $N \times N$  non-blocking switch can be constructed by a group of  $1 \times N$  switches [30][1] using the Spanke architecture as introduced in chapter 2. So it is also necessary to fully investigate the design of  $1 \times N$  switch for a single wavelength using IAWG-based planar lightwave circuit (PLC) and its applications to construct truly any-to-any  $N \times N$  wavelength switch.

In this chapter, we will utilize the Spanke architecture to realize a fully functional non-blocking  $N \times N$  WDM switch. From chapter 2, we have known that the Spanke architecture is based on the combination of  $2n$  ( $1 \times N$ ) optical switches. We will show how to realize this  $1 \times N$  optical switch by using IAWGs. We will

present a detailed description of a self-consistent design rule of  $1 \times N$  all optical switches. We will present the numerical results to illustrate the device characteristics such as transfer functions and the extinction ratio of the switch. Then a detailed design example of a  $1 \times 4$  non-blocking WDM switch will be given and the phase assignment at each phase shifter will be provided for various routing states. We will also propose and investigate a simplified structure of a  $1 \times N$  WDM all-optical switch based on a single IAWG with total reflection at the end of each phase shifter. Design considerations and device characteristics are discussed. It is also important to note that the proposed  $1 \times N$  switch structure is a planar lightwave circuit (PLC) with no waveguide crossing, therefore it can be monolithically integrated to create sophisticated optical devices with more functionalities.

### **3.2. An Approach of an $N \times N$ All Optical Switch**

It is well known that any-to-any  $N \times N$  non-blocking wavelength switches are indispensable for optical networks. However, the design of a true any-to-any  $N \times N$  optical switch using PLC technology is not an easy task because of its complexity and it has not been demonstrated so far. One modular approach to solve this problem is to combine a group of  $1 \times N$  optical switches. This has been shown in the Spanke architecture in chapter 2. To illustrate this architecture more clearly, figure 3.1 shows a  $4 \times 4$  non-blocking wavelength switch, which consists of eight  $1 \times 4$  wavelength switches with four of them at the input side and four of them at the output side. For

each  $1 \times 4$  optical switch at the input side, it switches the input signal of any of the four wavelengths  $\lambda_1$ ,  $\lambda_2$ ,  $\lambda_3$  and  $\lambda_4$  into any one of its four output ports. Similarly, each output  $1 \times 4$  optical switch combines the four received wavelength channels together and feeds them into the output fiber. Since optical switch functionality is determined by the four input  $1 \times 4$  switches, the four output switches are performing a redundant operation and can simply be replaced by four  $1 \times 4$  optical star couplers. However, with this simplified option, there will be a  $10\log(N)$  dB intrinsic combining loss for the optical signal because the power combiner is not wavelength selective.

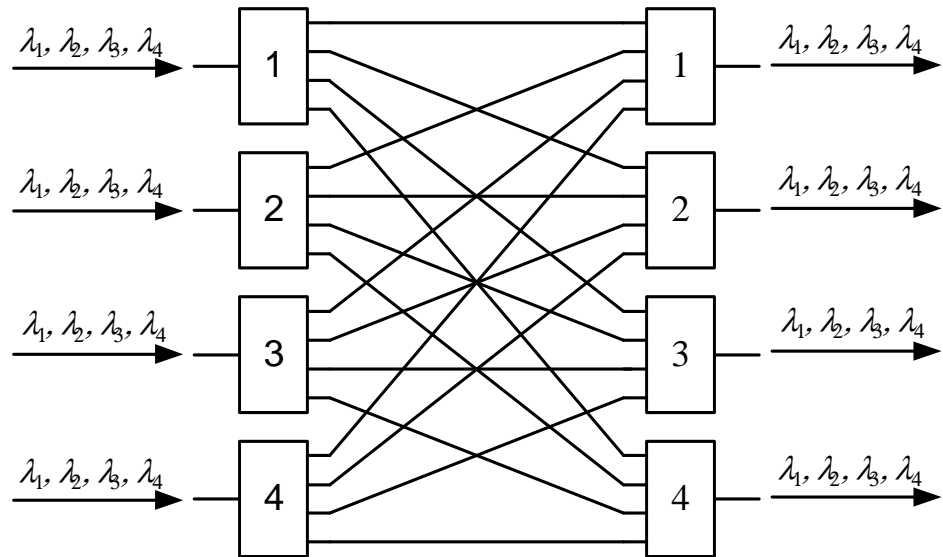


**Figure 3.1** The scheme of  $4 \times 4$  all-optical switch.

Since  $1 \times N$  wavelength switches are fundamental building blocks to realize this any-to-any  $N \times N$  non-blocking wavelength switch, the focus will be on the development of a general design rule for a  $1 \times N$  wavelength switch in the following sections.

### 3.3. The Scheme of the $1 \times N$ All-Optical Switch

The scheme of a  $1 \times N$  all-optical switch is presented in figure 3.2. This optical switch consists of two IAWGs and is very similar to the one Doerr suggested [27], as we have reviewed in subsection 2.7.3.1. Instead of having two or more input ports at the input side as suggested by Doerr, figure 3.2 has only one input port while still having  $N$  output ports. In this figure, star coupler 1 and 2 form the input  $N$ -interleaved AWG ( $N$ -IAWG). Star coupler 3 and 4 form the output  $N$ -IAWG. Between the two  $N$ -IAWGs are  $N$  subsets of phase shifters. Each subset has  $N$  phase shifters. The input  $N$ -IAWG is designed in such a way that the input signal with wavelength  $\lambda_i$  is directed into all  $l_{ij}$  phase shifters, where  $l_{ij}$  is the index of phase shifters,  $i = 1, 2, \dots, N$  is the index of ports in each Brillouin zone (BZ) and  $j = 1, 2, \dots, N$  is the index of BZs as shown in figure 3.2. Moreover, the  $N$ -IAWG is designed such that there is the same amount of signal power of wavelength  $\lambda_i$  entering each  $l_{ij}$  phase shifter. In this way, the routing of the input signal of wavelength  $\lambda_i$  can be totally controlled by all  $l_{ij}$  phase shifters so that  $1 \times N$  switching

functionality can be realized. The switching functionality will be further explained in the next section.

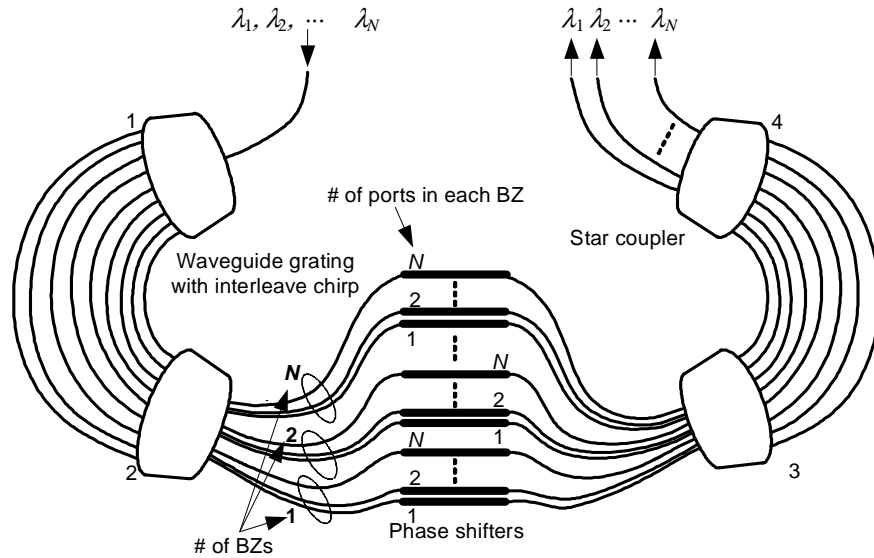


**Figure 3.2** Schematic diagram of  $1 \times N$  all-optical switch.

### 3.4. Design of the N-IAWG

#### 3.4.1. Functionality of N-IAWG

In section 3.3, we mentioned that  $N$ -IAWG is designed in such a way that the input signal with wavelength  $\lambda_i$  is directed into all the output waveguides that connect with  $l_{ij}$  phase shifters. To be convenient, we also use  $l_{ij}$  to denote these corresponding output waveguides. Moreover, for optimum operation, the amount of signal power entering each such waveguide should be the same.

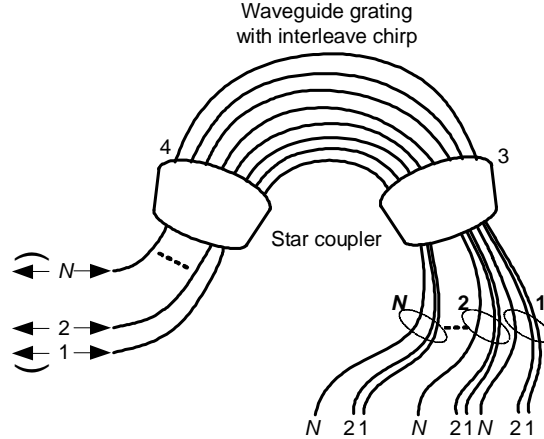


**Figure 3.3** Schematic diagram of  $N$ -IAWG.

The above condition was mentioned for the  $N$ -IAWG that has only one input port as in figure 3.2. It can be extended to a general  $N$ -IAWG that has  $N$  input ports as shown in figure 3.3. When the separation between the input ports at star coupler 4 are arranged properly, the  $N$ -IAWG can direct the signal of wavelength  $\lambda_i$  into the same  $l_{ij}$  output waveguides at star coupler 3, no matter which input port at star coupler 4 is chosen. Moreover, the amount of the power entering into each of these output waveguides at star coupler 3 is the same.

Based on the above description, we can see that for a signal at wavelength  $\lambda_i$ , no matter which input port at star coupler 4 it enters, the output power always distributes evenly among the same  $l_{ij}$  output waveguides of star coupler 3, but the phase distribution depends on the chosen input port. Because of reciprocity, if we

input a signal of wavelength  $\lambda_i$  into all those  $l_{ij}$  waveguides at star coupler 3, each with equal power, we can direct the signal into any one of the output ports at star coupler 4 by adjusting the phase of each input properly. This explains the switching functionality of figure 3.2. More details about this switching functionality will be given later.

### 3.4.2. From AWG to IAWG

Similar to an AWG, an IAWG has an input star coupler and an output star coupler. However, the path length difference between adjacent grating waveguides for an IAWG deviates from that of an AWG to create a wavelength-dependent focusing effect. To illustrate how to obtain the path length differences in IAWG, we can start with the central phase matching equation of a conventional AWG as shown in figure 2.13 [20][31]:

$$n_s d \sin(\theta_i) + n_c \cdot \Delta L + n_s d \sin(\theta_0) = m\lambda \quad (3.1)$$

Where  $m$  is the grating order,  $n_c$  is the effective refractive index of the arrayed waveguide,  $n_s$  is the effective index of the slab in the output star coupler,  $\Delta L$  is the path length difference between two adjacent waveguides in the array,  $d$  is the separation of adjacent waveguides at the star coupler,  $\theta_i$  is the angle of  $i$ -th input port to the direction of the central input port,  $\theta_0$  is the diffraction angle in the output star coupler and  $\lambda$  is the output wavelength. Compared with equation (2.20), we have included the term related to the input side into equation (3.1) for general purpose.

From equation (3.1), the angular width  $\Delta\theta$  of the Brillouin zone (BZ), which was defined in section 2.7.3., can be found as [32]:

$$\Delta\theta = \frac{\lambda}{n_s d} \quad (3.2)$$

The angular separation between  $-\Delta\theta/2$  and  $\Delta\theta/2$  is commonly referred to as the central Brillouin zone. Only the output in the central BZ is generally of concern for an AWG since most of the signal energy is concentrated in this area.

An  $N$ -IAWG varies the path length difference between the adjacent grating waveguides so that each original BZ in an AWG is split into  $N$  equally spaced new BZs [27]. Based on equation (3.2), we can find that the angular separation between two adjacent BZs in an  $N$ -IAWG is,

$$\Delta\theta_I = \frac{\lambda}{n_s d} \cdot \frac{1}{N} \quad (3.3)$$

The subscript  $I$  in equation (3.3) indicates interleave. Ideally the  $N$  BZs of an  $N$ -IAWG split from the central BZ of an AWG should have the same amount of output power according to the condition for optimum operation of  $N$ -IAWG as we mentioned above. Each should have output power  $1/N$  if the output power in the central BZ of the AWG is normalized. Because most of the output power is concentrated in this area [27], these  $N$  new BZs play important roles in the devices consisting of  $N$ -IAWGs.

### 3.4.3. AWG Multiple-Beam Interference Condition

Although the general concept was discussed in the above section, the design of an  $N$ -IAWG is not an easy task. Now we start presenting a general rule to design an  $N$ -IAWG. To simplify the explanation, we illustrate the design rule through the process of constructing a 4-IAWG as shown in figure 3.4, where figure 3.4(b) shows that the central BZ of an AWG is split into four new BZs for the 4-IAWG. We start with a conventional AWG, which has  $M$  waveguides in the arrayed grating. We then divide these  $M$  waveguides into four subsets with the  $p$ -th subset composed of waveguides  $p, p+4, p+8, p+12, \dots$ , where  $p = 1, 2, 3, 4$ . In this arrangement, removing any three of the four subsets, the remaining subset is still an AWG but with path length difference  $4\Delta L$  between adjacent waveguides and with waveguide separation  $4d$  at the input and output star couplers. With a single wavelength ( $\lambda_0$ ) signal entering this remaining subset, the central phase match condition of this new AWG can be obtained from equation (3.1)

$$n_s(4d) \sin(\theta_i) + n_c \cdot (4\Delta L) + n_s(4d) \sin(\theta_0) = m' \lambda_0 \quad (3.4)$$

where  $m'$  is the grading order of this new AWG. Therefore the angular separation between two adjacent BZs at the output of the star coupler of this reduced AWG is,

$$\Delta\theta' = \frac{\lambda_0}{n_s(4d)} \quad (3.5)$$

Comparing equation (3.5) with equations (3.2) and (3.3), we can see that the BZ of a subset AWG has the same angular width as a 4-IAWG, which is 1/4 that of the original AWG. For each of the four subset AWGs, the radiation patterns are the same

in all the four new BZs denoted as  $\Omega_{-1}$ ,  $\Omega_0$ ,  $\Omega_1$  and  $\Omega_2$  as shown in Figure 3.4(b).

Since these 4 subsets combine only to form the original AWG, when all the 4 subsets exist, there is only one maximum for the output field pattern in the entire angular region of  $\Omega_{-1}$ ,  $\Omega_0$ ,  $\Omega_1$  and  $\Omega_2$ , which is the central BZ of the original AWG. This maximum output value happens in  $\Omega_0$ . This leads to the conclusion: when the input is at wavelength  $\lambda_0$ , the signals from the four subsets of the arrayed waveguides add constructively in  $\Omega_0$  and destructively in  $\Omega_{-1}$ ,  $\Omega_1$  and  $\Omega_2$ .

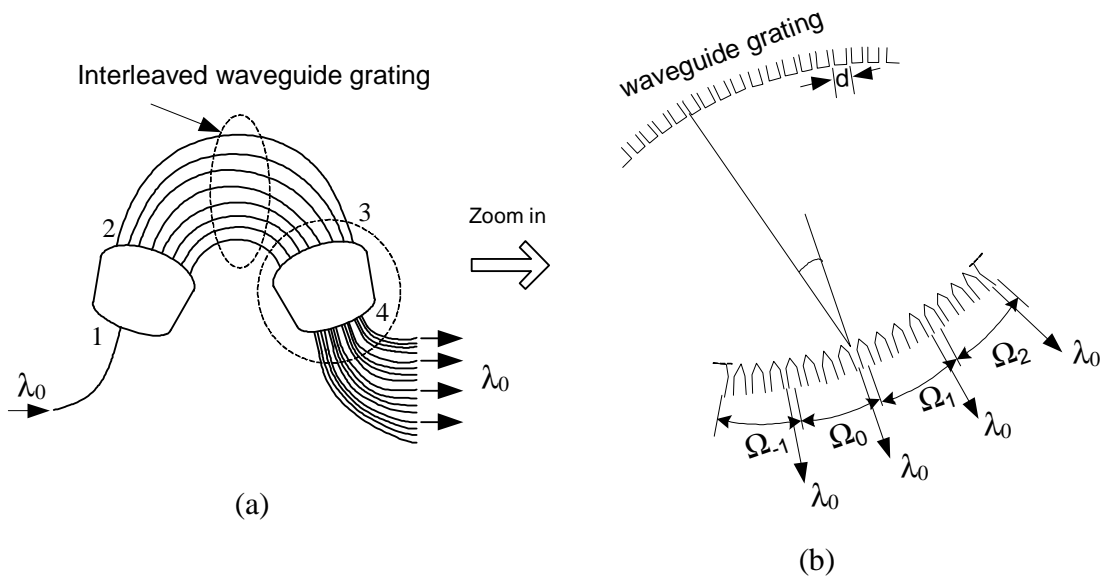


**Figure 3.4** Diagram of output port distribution for an  $N$ -interleaved AWG. (a) An  $N$ -interleaved AWG, where  $N = 4$ ; (b) Close-up of the output star coupler, where  $\Omega_i$  ( $i = -1, 0, 1, 2$ ) denotes the new Brillouin zones of this 4-IAWG. These new BZs were split from the central BZ of a conventional AWG before it was interleaved.

### 3.4.4. Vector Illustration of the AWG Multiple-Beam Interference Condition

**Table 3.1** Initial Vector Information for Constructing a 4-IWG

BZ	Vector Addition
$\Omega_0$	<p>Diagram illustrating vector addition for BZ <math>\Omega_0</math>. Four vectors <math>\vec{A}_{1,0}</math>, <math>\vec{A}_{2,0}</math>, <math>\vec{A}_{3,0}</math>, and <math>\vec{A}_{4,0}</math> originate from a common point labeled <math>0</math>.</p>
$\Omega_1$	<p>Diagram illustrating vector addition for BZ <math>\Omega_1</math>. Four vectors <math>\vec{A}_{1,1}</math>, <math>\vec{A}_{2,1}</math>, <math>\vec{A}_{3,1}</math>, and <math>\vec{A}_{4,1}</math> originate from a common point labeled <math>0</math>.</p>
$\Omega_2$	<p>Diagram illustrating vector addition for BZ <math>\Omega_2</math>. Four vectors <math>\vec{A}_{1,2}</math>, <math>\vec{A}_{2,2}</math>, <math>\vec{A}_{3,2}</math>, and <math>\vec{A}_{4,2}</math> originate from a common point labeled <math>0</math>.</p>
$\Omega_{-1}$	<p>Diagram illustrating vector addition for BZ <math>\Omega_{-1}</math>. Four vectors <math>\vec{A}_{1,-1}</math>, <math>\vec{A}_{2,-1}</math>, <math>\vec{A}_{3,-1}</math>, and <math>\vec{A}_{4,-1}</math> originate from a common point labeled <math>0</math>.</p>

To systematically investigate the pattern of optical field distribution at the output of the second star coupler of a conventional AWG, a vector representation can be used. Let's take subset  $p$  of the arrayed waveguides and denote its optical field output in BZ  $\Omega_q$  as a vector  $\vec{A}_{p,q}$ , where  $p = 1, 2, 3, 4$  and  $q = -1, 0, 1, 2$  in our above example. We have

$$\sum_{p=1}^4 \vec{A}_{p,q} = \begin{cases} 0 & q = -1, 1, 2 \\ 4 \cdot \vec{A}_{1,0} & q = 0 \end{cases} \quad (3.6)$$

More specifically, the above vector additions are illustrated in table 3.1, where the relative phase angles between the vectors are considered and the vectors  $\vec{A}_{1,q}$  are treated as the references.

From table 3.1, we can see that although each subset of bridge waveguides by itself would project the same amount of output power in each of these new BZs,  $\Omega_q$ , the combination of the four subsets creates only one maximum which is located in BZ  $\Omega_0$  as the result of the vector addition of four field components in each BZ. If the optical field magnitude created by each subset is  $A_0 = |\vec{A}_{p,q}|$ , the maximum output optical power in  $\Omega_0$  will be  $16A_0^2$ .

### 3.4.5. Additional Lengths to Arrayed Waveguides for Constructing 4-IAWG

In subsection 3.4.2, we mentioned that we could vary the path length difference between the adjacent gratings to obtain an  $N$ -IAWG. For a conventional AWG, this path length difference is [31]

$$\Delta L = \frac{m\lambda_0}{n_c} \quad (3.7)$$

**Table 3.2** Vector Information of a Constructed 4-IAWG

BZ	Vector Addition
$\Omega_0$	
$\Omega_1$	
$\Omega_2$	
$\Omega_{-1}$	

where  $m$  is the order of the array,  $\lambda_0$  is the center operating wavelength of the device and  $n_c$  is the effective index of the arrayed waveguide. Now we will show how to find the additional waveguide lengths in addition to the  $\Delta L$  in equation (3.7) to construct an  $N$ -IAWG. We still use the 4-IAWG as an example. By rotating all the  $\vec{A}_{2,q}$  vectors in table 3.1 by 180 degrees, the results of the vector additions turn out to be as in table 3.2. From table 3.2, it is shown that this  $\pi$  phase change makes the output power equally split among the four BZs and the output power at each BZ be  $4A_0^2$ , which is 1/4 of the maximum power shown in table 3.1.

To rotate all the vectors  $\vec{A}_{2,q}$  in table 3.1 by 180 degree means to change the phase of the output vector from subset 2 waveguides by  $\pi$ . This can be realized by adding additional length  $\lambda_{0c}/2$  to all the waveguides of subset 2, where  $\lambda_{0c} = \lambda_0/n_c$ . Furthermore, it can be easily seen that a 4-IAWG can be realized by adding an additional length  $\lambda_{0c}/2$  to all the waveguides in any one of the four subsets while keeping the waveguides in three other remaining subsets unchanged.

The procedure can be further simplified. In the above process, all four BZs were considered in finding the additional waveguide lengths. Since the initial value of the sum of all the vectors in each of the BZs  $\Omega_{-1}$ ,  $\Omega_1$  and  $\Omega_2$  is zero, the magnitudes of the vector summations in these three BZs will always be the same as long as each of vectors  $\vec{A}_{2,q}$  turns a same amount of angle in each of these BZs. This fact tells us that only one of these three BZs needs to be considered together with BZ  $\Omega_0$  in the designing of a 4-IAWG. This will be further explained later.

### 3.4.6. General Design Rule of N-IAWG

Based on the above example, a general rule in designing an  $N$ -IAWG can be deduced. Firstly, one can divide the  $M$  arrayed waveguides in the AWG into  $N$  subsets. In each subset,  $N\cdot\Delta L$  is the path length difference between adjacent waveguides and  $N\cdot d$  is the arrayed waveguide separation at the input and output star couplers. Secondly, one can find the initial vector information as in table 3.1. As mentioned above, it is only needed to consider one more BZ, say  $\Omega_1$ , besides the central BZ  $\Omega_0$ , where the maximum initial output power  $N^2 A_0^2$  exists. Then initially, the sum of the vectors in BZ  $\Omega_0$  and  $\Omega_1$  are

$$\vec{V}_{\Omega_0} = \sum_{p=1}^N \vec{A}_{p,0} = N \cdot \vec{A}_{1,0} \quad (3.8a)$$

$$\vec{V}_{\Omega_1} = \sum_{p=1}^N \vec{A}_{p,1} = 0 \quad (3.8b)$$

So one can get the similar graphs as shown in table 3.1. Thirdly, one rotates any pair of vectors  $\vec{A}_{p,0}$  and  $\vec{A}_{p,1}$  by the same angle  $\delta_p$ , where  $p = 2, \dots, N$ . We then rotate as many pairs as necessary until the following condition is met

$$\vec{V}_{\Omega_0} = \sum_{p=1}^N \vec{A}_{p,0} = \sum_{p=1}^N \vec{A}_{p,1} = \vec{V}_{\Omega_1} = \sqrt{N} \cdot \vec{A}_{1,0} \quad (3.9)$$

At this point, one can record all the angular values,  $\delta_p$ , and the additional length needed for the waveguides in Subset  $p$  can be calculated as

$$\Delta L_{\text{add}} = \frac{\delta_p}{2\pi} \cdot \lambda_{0c} \quad (3.10)$$

where  $\delta_p$  is in radians. Since  $0 \leq \delta_p < 2\pi$ ,  $\Delta L_{\text{add}}$  is always less than  $\lambda_{0c}$ . Finding  $\Delta L_{\text{add}}$  values is essential in the design of an  $N$ -IAWG.

### 3.4.7. Output Port Arrangement

From the above description,  $\Omega_0$  is always used as the central BZ. This means the output ports on the second star coupler have to be arranged in accordance with the locations of BZs as illustrated in figure 3.4(a). Figure 3.4(b) is a detailed description of the output star coupler, where if  $N$  is an odd number, the distribution of waveguides is symmetrical about the center of the output star coupler, while if  $N$  is an even number there is one extra output port on one side in comparison to the other side.

**Table 3.3** Multiple sets of additional waveguide lengths [ $\lambda_c$ ] in the design of an  $N$ -IAWG

$N$	Calculated Additional Arrayed Waveguide Lengths [ $\lambda_c$ ]
2	1/4, 0
3	1/3, 0, 0
	2/3, 0, 0
4	1/2, 0, 0, 0
	1/4, 1/2, 1/4, 0
	3/4, 1/2, 3/4, 0
5	0, 2/5, 1/5, 2/5, 0
	0, 3/5, 4/5, 3/5, 0
	0, 1/5, 3/5, 1/5, 0
	0, 4/5, 2/5, 4/5, 0
6	1/12, 1/3, 3/4, 1/3, 1/12, 0

	11/12, 0, 1/4, 2/3, 1/4, 0
	3/4, 2/3, 3/4, 0, 5/12, 0
	1/4, 1/3, 1/4, 0, 7/12, 0
	1/12, 0, 3/4, 1/3, 3/4, 0
	11/12, 2/3, 1/4, 2/3, 11/12, 0
7	0, 1/7, 3/7, 6/7, 3/7, 1/7, 0
	0, 2/7, 6/7, 5/7, 6/7, 2/7, 0
	0, 3/7, 2/7, 4/7, 2/7, 3/7, 0
	0, 4/7, 5/7, 3/7, 5/7, 4/7, 0
	0, 5/7, 1/7, 2/7, 1/7, 5/7, 0
	0, 6/7, 4/7, 1/7, 4/7, 6/7, 0
8	0, 3/4, 1/2, 0, 1/2, 3/4, 0, 0
	1/8, 1/4, 5/8, 0, 5/8, 1/4, 1/8, 0
	0, 0, 1/4, 1/2, 0, 1/2, 1/4, 0
	1/8, 0, 3/8, 1/2, 1/8, 1/2, 3/8, 0
	0, 1/4, 0, 0, 1/2, 1/4, 1/2, 0
	1/8, 1/4, 1/8, 0, 5/8, 1/4, 5/8, 0
	7/8, 3/4, 3/8, 0, 3/8, 3/4, 7/8, 0

### 3.4.8. Comparison with Previous Results

The general rule discussed above can be used to calculate the additional lengths  $\Delta L_{\text{add}}$  needed in arrayed waveguides of an AWG to transfer it into an  $N$ -IAWG for any  $N$  value. Generally, multiple sets of additional lengths can be obtained with the general design rule for a particular  $N$ . Table 3.3 shows the examples of the additional lengths that were calculated by using this general rule for  $N = 2, 3, 4, 5, 6$ ,

7, 8. All these values have been verified as good for constructing their respective  $N$ -IAWGs.

Also shown in table 3.4 is another special set of additional lengths given by Doerr in [27] where there is not a systematic design rule provided. Comparing Doerr's result with our simulation results presented in table 3.3, it can be found that Doerr's result is clearly only one of the solutions that can be obtained by using the general design rule. For example, Doerr's result of  $(3/4, 1/3, 3/4, 0, 1/12, 0)$  for  $N = 6$ , is the same as our simulation result of  $(1/12, 0, 3/4, 1/3, 3/4, 0)$  for  $N = 6$ .

**Table 3.4** Comparisons between the distributions of additional waveguide lengths [ $\lambda_c$ ] in the design of IAWG

$N$	Additional Waveguide Lengths [ $\lambda_c$ ] From [4]
2	1/4, 0
3	1/3, 0, 0
4	1/2, 0, 0, 0
5	1/5, 3/5, 1/5, 0, 0
6	3/4, 1/3, 3/4, 0, 1/12, 0
7	1/7, 3/7, 6/7, 3/7, 1/7, 0, 0
8	1/4, 1/2, 0, 1/2, 1/4, 0, 0, 0

This further confirms that the general rule gives us a way to find the additional length distribution in arrayed waveguides needed for constructing an  $N$ -IAWG. The fact that there are multiple sets of additional length distributions for each  $N$  value

benefits the design of an  $N$ -IAWG in that the optimum set of additional lengths can be chosen.

### 3.4.9. Verification of Equal Vector Magnitudes in BZs of N-IAWG

In subsection 3.4.5, it was mentioned that the magnitudes of the vector summations in BZs  $\Omega_{-1}$ ,  $\Omega_1$  and  $\Omega_2$  are the same as long as each of vectors  $\vec{A}_{2,q}$  turns a same amount of angle. This is obvious in the structure of 4-IAWG that was discussed above. In this subsection, this consequence of equal vector magnitudes in BZs will be verified for 5-IAWG in a relatively general way so that its method can be applied to any  $N$ -IAWG for any values of  $N$ .

As in the case of 4-IAWG, to construct a 5-IAWG, we can divide the  $M$  arrayed waveguides of a conventional AWG into five subsets with the  $p$ -th subset composed of waveguides  $p, p+5, p+10, p+15, p+20$ , where  $p = 1, 2, 3, 4, 5$ . In this arrangement, removing any four from the five subsets, the remaining subset is still an AWG but with path length difference  $5\Delta L$  between adjacent waveguides in the array and with waveguide separation  $5d$  at the input and output star couplers.

Similarly, let a single wavelength ( $\lambda_0$ ) signal enter this remaining subset, the central phase match condition of this new AWG would be

$$n_s(5d)\sin(\theta_i) + n_c \cdot (5\Delta L) + n_s(5d)\sin(\theta_0) = m' \lambda_0 \quad (3.11)$$

And the angular separation between two adjacent BZs at the output of the star coupler of this reduced AWG is,

$$\Delta\theta' = \frac{\lambda_0}{n_s(5d)} \quad (3.12)$$

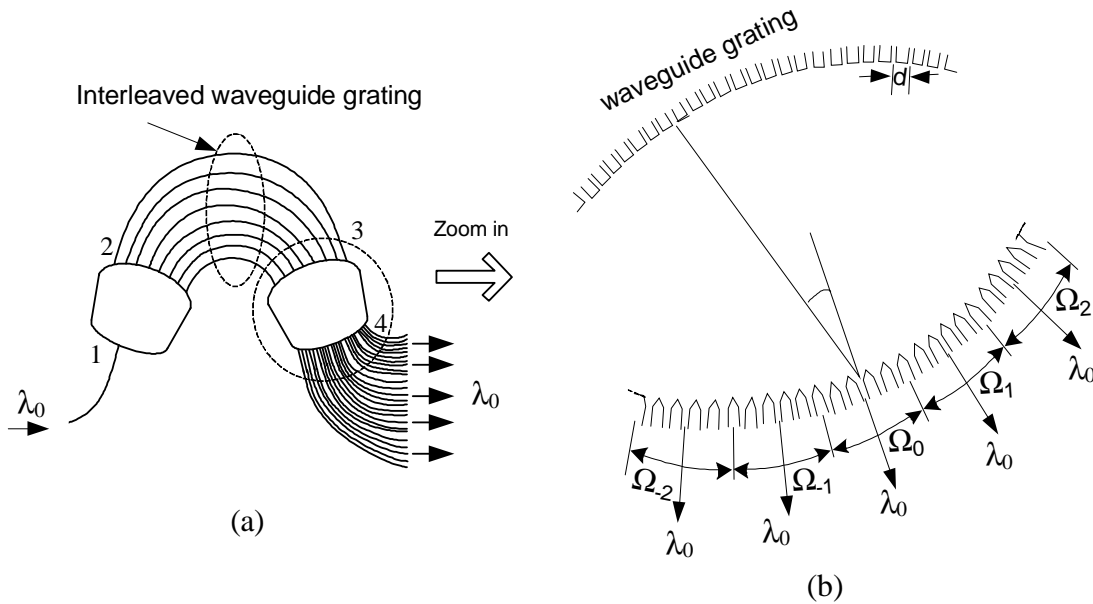


**Figure 3.5** (a) Diagram of output port distribution for a 5-interleaved AWG. (b) Close-up of the output star coupler, where  $\Omega_i$  ( $i = -2, -1, 0, 1, 2$ ) denotes the new BZs of this 5-IAWG. These new BZs were split from the central BZ of a conventional AWG before it was interleaved.

We can see that the BZ of a subset AWG has the same angular width as a 5-IAWG, which is 1/5 that of the original AWG. Similar to the case of 4-IAWG, for each of the five subset AWGs, the radiation patterns are the same in all the five new BZs denoted as  $\Omega_{-2}$ ,  $\Omega_{-1}$ ,  $\Omega_0$ ,  $\Omega_1$  and  $\Omega_2$  as in Figure 3.5b. Since these five subsets combine only to form the original AWG, when all the five subsets exist, there is only

one maximum for the output field pattern in the combining angular region of  $\Omega_{-2}$ ,  $\Omega_{-1}$ ,  $\Omega_0$ ,  $\Omega_1$  and  $\Omega_2$ , which is the central BZ of the original AWG. This maximum output value happens in  $\Omega_0$ . This leads to the conclusion, the signals from the five subsets of the arrayed waveguides add constructively in  $\Omega_0$  and destructively in  $\Omega_{-2}$ ,  $\Omega_{-1}$ ,  $\Omega_1$  and  $\Omega_2$ .

Similarly, we can have a vector representation, which is shown in the following equation

$$\sum_{p=1}^5 \vec{A}_{p,q} = \begin{cases} 0 & q = -2, -1, 1, 2 \\ 5 \cdot \vec{A}_{1,0} & q = 0 \end{cases} \quad (3.13)$$

where  $p = 1, 2, 3, 4, 5$  and  $q = -2, -1, 0, 1, 2$  in this case. These vector additions are illustrated in table 3.5, where the relative phase angles between the vectors are considered and the vectors  $\vec{A}_{1,q}$  are treated as the references.

From table 3.5, if the optical field magnitude created by each subset is  $A_0 = |\vec{A}_{p,q}|$ , the maximum output optical power in  $\Omega_0$  will be  $25A_0^2$ . The optical powers in other BZs are all equal to zeros just as in the case of 4-IAWG.

Our result in subsection 3.4.8 shows that if we keep the arrayed waveguide lengths in the first and fifth subsets, add additional lengths of  $(2\lambda_{0c})/5$  to all the waveguides in the second and fourth subsets and add additional lengths of  $\lambda_{0c}/5$  to all the waveguides in the third subset, the output optical powers in the five BZs will be

the same, which is equal to  $5A_0^2$ , which is 1/5 of the maximum power shown in table 3.5. Thus a conventional AWG is turned into a 5-IAWG.

**Table 3.5** Initial Vector Information of Constructing a 5-IAWG

BZ	Vector Addition
$\Omega_0$	
$\Omega_1$	
$\Omega_2$	
$\Omega_{-1}$	
$\Omega_{-2}$	

As we know, adding additional lengths of  $\lambda_{0c}/5$  to the waveguides of the third subset is equivalent to turning all the vectors  $\vec{A}_{3,q}$  by  $\alpha$  radians, and adding additional lengths of  $(2\lambda_{0c})/5$  to the waveguides in the second and fourth subsets is equivalent to turning all the vectors  $\vec{A}_{2,q}$  and  $\vec{A}_{4,q}$  by  $2\alpha$  radians, where  $\alpha = 2\pi/5$ .

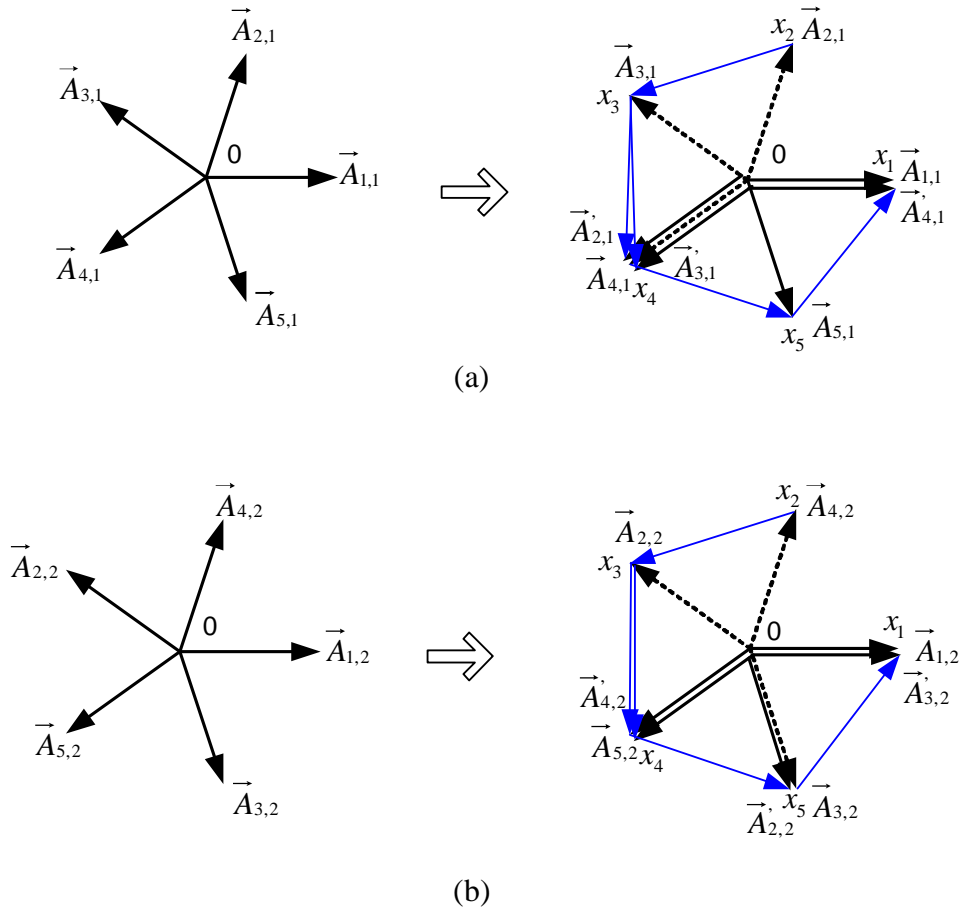


**Figure 3.6** (a) The changes of the signal vectors in BZ  $\Omega_1$  when an AWG changes to a 5-IAWG; (b) The changes of the signal vectors in BZ  $\Omega_2$  when an AWG changes to a 5-IAWG.

Now let's verify that the optical powers are the same in BZs  $\Omega_1$  and  $\Omega_2$  after the vectors are turned the above angles. Figure 3.6 shows the changes of the signal vectors in BZs of  $\Omega_1$  and  $\Omega_2$ . Figure 3.6a shows that vectors  $\vec{A}_{2,1}$ ,  $\vec{A}_{3,1}$  and  $\vec{A}_{4,1}$  are changed to  $\vec{A}'_{2,1}$ ,  $\vec{A}'_{3,1}$  and  $\vec{A}'_{4,1}$ . From equation (3.13) we know that

$$\vec{A}_{1,1} + \vec{A}_{2,1} + \vec{A}_{3,1} + \vec{A}_{4,1} + \vec{A}_{5,1} = 0 \quad (3.14)$$

So we have

$$\vec{A}_{1,1} + \vec{A}'_{2,1} + \vec{A}'_{3,1} + \vec{A}'_{4,1} + \vec{A}_{5,1} = (\overrightarrow{x_2x_3} + \overrightarrow{x_3x_4}) + \overrightarrow{x_3x_4} + (\overrightarrow{x_4x_5} + \overrightarrow{x_5x_1}) \quad (3.15)$$

Where

$$\vec{A}'_{2,1} - \vec{A}_{2,1} = (\overrightarrow{x_2x_3} + \overrightarrow{x_3x_4}) \quad (3.16a)$$

$$\vec{A}'_{3,1} - \vec{A}_{3,1} = \overrightarrow{x_3x_4} \quad (3.16b)$$

$$\vec{A}'_{4,1} - \vec{A}_{4,1} = (\overrightarrow{x_4x_5} + \overrightarrow{x_5x_1}) \quad (3.16c)$$

Let

$$\overrightarrow{x_2x_3} = \vec{V}_0, \quad (3.17)$$

We have

$$\overrightarrow{x_3x_4} = \vec{V}_0 e^{j\alpha}, \quad \overrightarrow{x_4x_5} = \vec{V}_0 e^{j2\alpha}, \quad \overrightarrow{x_5x_1} = \vec{V}_0 e^{j3\alpha}, \quad (3.18)$$

Combine equations (3.18) and (3.15),

$$\begin{aligned} \vec{A}_{1,1} + \vec{A}'_{2,1} + \vec{A}'_{3,1} + \vec{A}'_{4,1} + \vec{A}_{5,1} &= (\vec{V}_0 + \vec{V}_0 e^{j\alpha}) + \vec{V}_0 e^{j\alpha} + (\vec{V}_0 e^{j2\alpha} + \vec{V}_0 e^{j3\alpha}) \\ &= \vec{V}_0 (1 + 2e^{j\alpha} + e^{j2\alpha} + e^{j3\alpha}) \end{aligned} \quad (3.19)$$

Similarly, from figure 3.6b, we can get

$$\begin{aligned}
\vec{A}_{1,2} + \vec{A}_{2,2} + \vec{A}_{3,2} + \vec{A}_{4,2} + \vec{A}_{5,2} &= (\overrightarrow{x_3x_4} + \overrightarrow{x_4x_5}) + \overrightarrow{x_5x_1} + (\overrightarrow{x_2x_3} + \overrightarrow{x_3x_4}) \\
&= (\vec{V}_0 e^{j\alpha} + \vec{V}_0 e^{j2\alpha}) + \vec{V}_0 e^{j3\alpha} + (\vec{V}_0 + \vec{V}_0 e^{j\alpha}) \\
&= \vec{V}_0 (1 + 2e^{j\alpha} + e^{j2\alpha} + e^{j3\alpha})
\end{aligned} \tag{3.20}$$

So from (3.19) and (3.20), we can see that

$$\vec{A}_{1,1} + \vec{A}_{2,1} + \vec{A}_{3,1} + \vec{A}_{4,1} + \vec{A}_{5,1} = \vec{A}_{1,2} + \vec{A}_{2,2} + \vec{A}_{3,2} + \vec{A}_{4,2} + \vec{A}_{5,2} \tag{3.21}$$

This verifies that the optical powers are the same in BZs  $\Omega_1$  and  $\Omega_2$  after the vectors are turned their relative angles. If we look at figure 3.6 clearly, we can see that the result in equation (3.21) can be obtained directly from the figure.

Furthermore, by using the same vector method, we can get

$$\sum_{p=1}^5 (\vec{A}_{p,q} - \vec{A}_{p,q}) = \sqrt{5} \cdot |\vec{A}_{1,0}| \quad \text{for } q = 1, 2, 3, 4, 5 \tag{3.22}$$

This verifies that optical powers are all the same in BZs of the 5-IAWG. By using this same method, we can verify that the optical powers are split evenly among the BZs of an  $N$ -IAWG. This guarantees that the functionality of an  $N$ -IAWG is feasible.

### 3.4.10. Verification of N-IAWG with Numerical Simulation

In the above sub-sections, the general design rule has been given out, and multiple sets of additional lengths are calculated and compared with a special set of additional lengths presented by Doerr. In this subsection, numerical simulations will be applied to verify that the additional lengths applied to the arrayed waveguides do change an AWG to an IAWG. Again the 4-IAWG as shown in figure 3.4 is taken as an example. In the simulation, the 4-IAWG is designed for four channels with channel wavelengths 1549.2 nm, 1549.6 nm, 1550.0 nm and 1550.4 nm. The

wavelength  $\lambda_0$  used to design the 4-IAWG was 1550.0 nm, and a signal with constant spectrum between 1549.2-1550.8 nm as the input. Since the amplitude distribution of a star coupler is a Gaussian distribution [33], the intensity distribution at the output side of the first star coupler in 4-IAWG, which is position 2 in figure 3.4, is also a Gaussian, which can be expressed as

$$I(m) = I_0(\sigma, M, m) \quad (3.23a)$$

where  $I_0$  is a discrete Gaussian distribution, which is expressed as

$$I_0(\sigma, M, m) = \frac{1}{\sigma\sqrt{2\pi}} \exp\left[-\frac{\left(m - \frac{M}{2}\right)^2}{2\sigma^2}\right] \quad (3.23b)$$

In the application,  $m = 1, 2, \dots, M$ , is the index of the waveguides in the array.  $M$  is the total number of the waveguides in the array.  $\sigma$  is the standard variance of the distribution. In the design example of 4-IAWG, the following values are chosen:  $M = 64$ ,  $\sigma = \sigma_0 = 0.36*(W/2)$ , where  $W = 63D_0$  is the width of the output range of the star coupler with  $D_0$  as the output waveguide separation.

Matlab programs had been composed, and simulations had been run. The simulation results are shown in figure 3.7. Figure 3.7a shows the output powers of the four output ports for wavelength  $\lambda_0 = 1550$  nm. It is quite clear that these four outputs have exactly the same powers at the same wavelengths with peak value at  $\lambda_0 = 1550$  nm. Figure 3.7b, 3.7c and 3.7d show the output powers of three other channels from 12 other output ports as shown in figure 3.4a. Each channel relates to four output

ports. It can be seen that all these simulation results have verified the design of 4-IAWG.

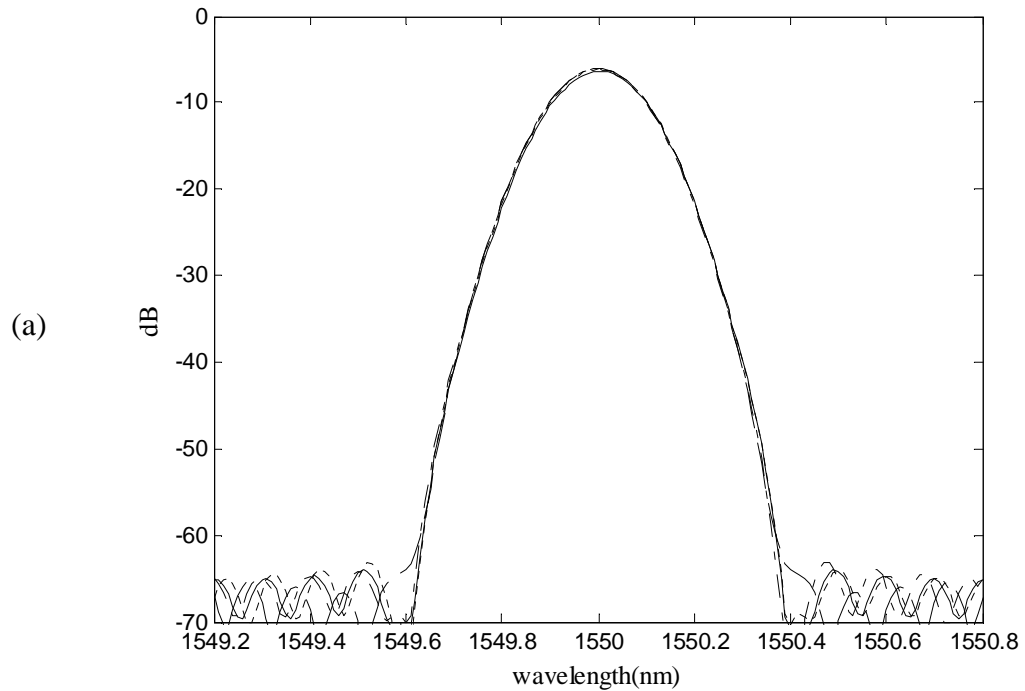


**Figure 3.7** Verification of 4-IAWG. The output powers at its related four output ports are exactly the same for each channel. (a) Central channel with wavelength  $\lambda_0 = 1550$  nm, (b) Channel of wavelength 1549.2 nm, (c) Channel of wavelength 1549.6 nm, (d) Channel of wavelength 1550.4 nm.

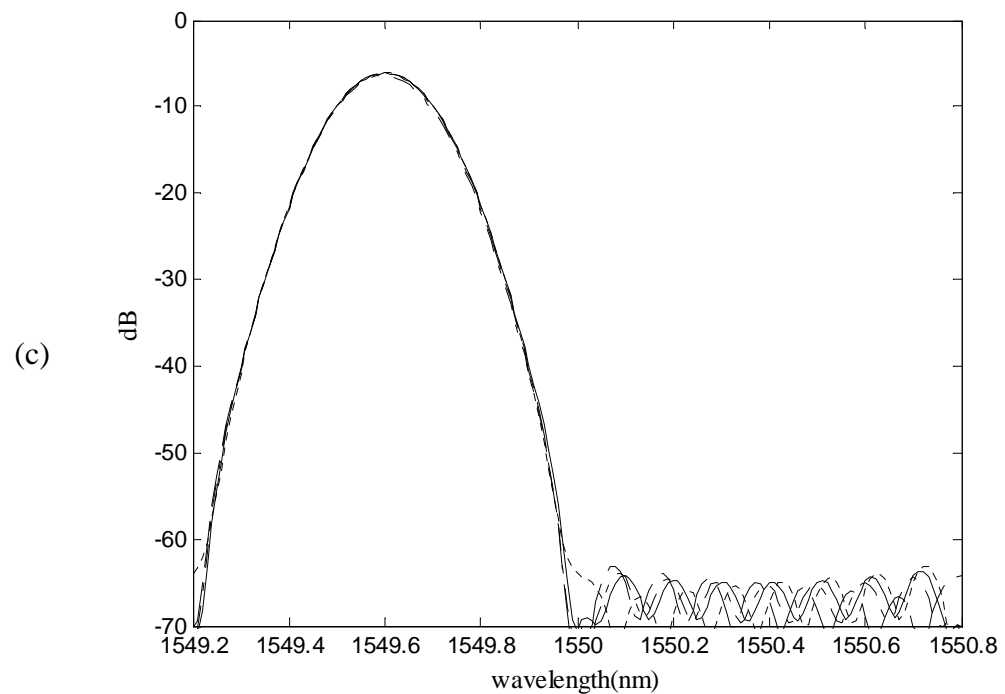
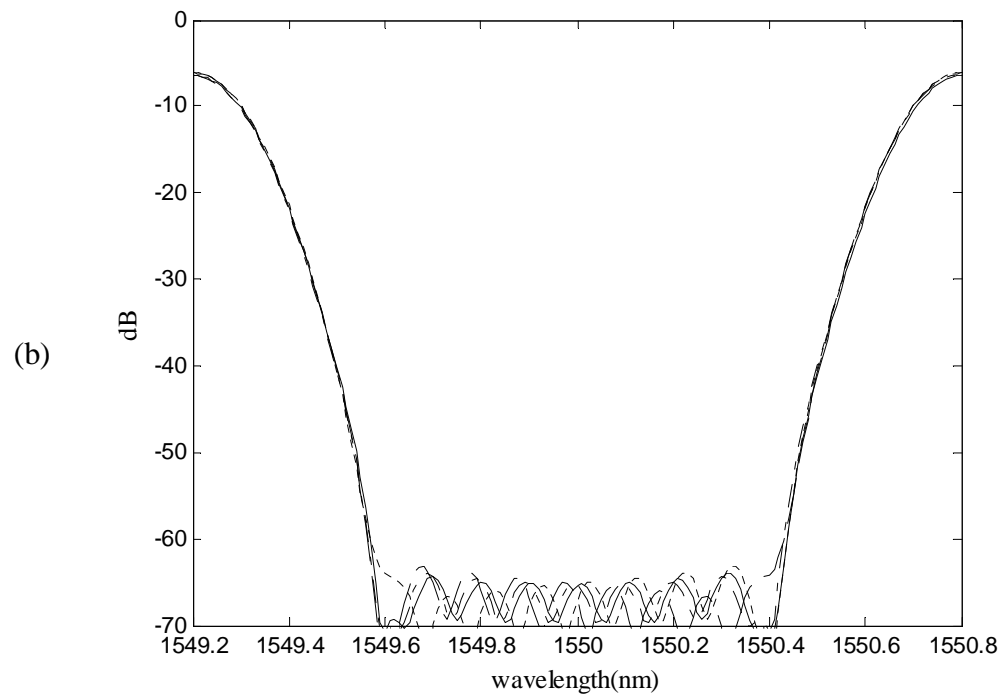


**Figure 3.7** (b) and (c)

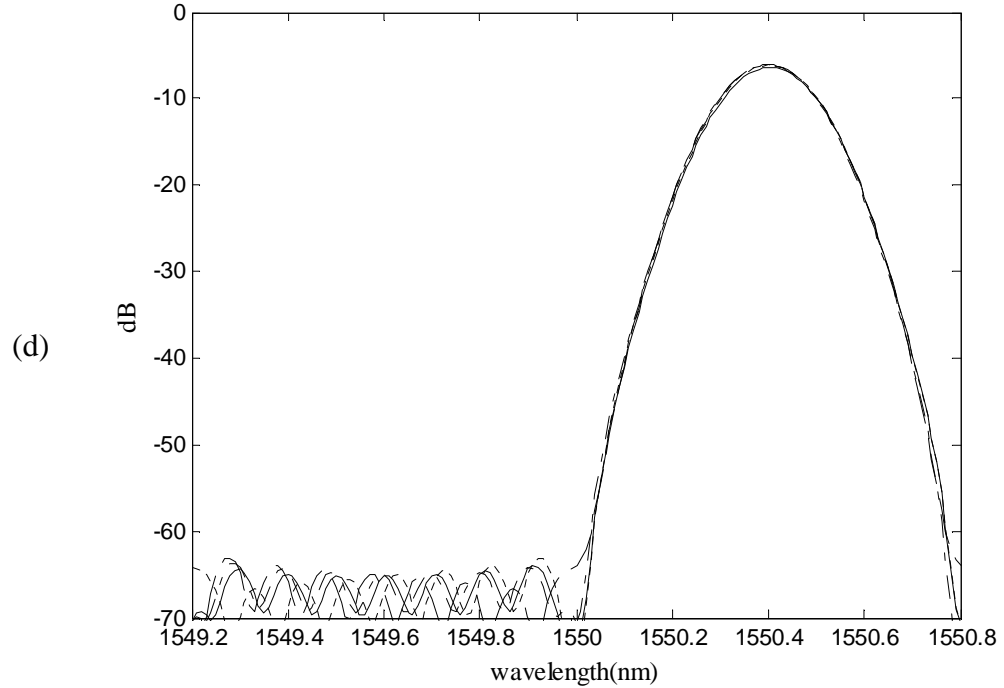


**Figure 3.7 (d)**

### 3.4.11. Transfer function of an N-IAWG

Since the design of an  $N$ -IAWG has been verified, it is time to find its transfer function. With the intensity Gaussian distribution at the star coupler as shown in equation (3.23), the output amplitude at one of the output ports of an  $N$ -IAWG can be expressed as,

$$A_{\text{IAWG}}(l, \lambda) = C(l) \cdot \sum_{m=1}^M A(m) B(m) \exp\left\{jk \cdot \left[L_0 + (m-1) \cdot \Delta L + ADDL(m-1)\right] \cdot N_c\right\} \\ + \left[P(x_1(0), (m-1)) + Q((m-1), x_2(l))\right] \cdot N_s \} \quad (3.24)$$

where  $l$  is the position index of the output ports at the second star coupler,  $\lambda$  is the channel wavelength,  $L_0$  is the length of the shortest waveguide in the waveguide array,  $N_c$  is the refractive index of waveguide while  $N_s$  is the refractive index of the slab region of the star coupler.  $\Delta L$  is the path length difference between adjacent arrayed waveguides of a traditional AWG.  $ADDL$  gives the additional lengths added to the arrayed waveguides in AWG to obtain IAWG.  $A(m)$  is the amplitude distribution at the input side of the arrayed waveguides,  $B(m)$  is the modification factor for the output of the arrayed waveguides transmitting to the output ports at the second star coupler.  $C(l)$  is the modification factor to the output at the  $l$ -th output port of the second star coupler due to Gaussian distribution.  $P(x_1, m)$  is the path length from the input port at  $x_1$  through the first star coupler to the  $m$ -th arrayed waveguide.  $Q(m, l)$  is the path length from the  $m$ -th arrayed waveguide through the second star coupler to the  $l$ -th output port. Here  $m$  is 0 for the shortest waveguide in the array. According to [33], we have

$$P(x_1, m) = R_0 - \frac{(2m-1)x_1 d}{2R_0} \quad (3.25)$$

$$Q(m, x_2) = R_0 - \frac{(2m-1)x_2 d}{2R_0} \quad (3.26)$$

where,  $x_1$  and  $x_2$  denotes the positions of the input port and output port on the relative star couplers,  $d$  is the arrayed waveguide separation,  $R_0$  is the radius of curvature of the star coupler. The distribution factors in equation (3.24) are expressed as

$$A(m) = B(m) = [I_0(\sigma_0, M, m)]^{1/2} \quad (3.27)$$

$$C(l) = \left[ (\sigma_0 \sqrt{2\pi}) \cdot I_0(\sigma_0 / 2, M, l) \right]^{1/2} \quad (3.28)$$

where equation (3.27) is due to the principle of reciprocity. The distribution  $C(l)$  is normalized and the half width as in equation (3.28) is due to the Rowland structure of the star coupler. Equation (3.24) can be written as

$$\begin{aligned} A_{\text{IAWG}}(l, \lambda) = & C(l) \cdot \sum_{m=1}^M I(m) \exp \left\{ jk \cdot \left[ [L_0 + (m-1) \cdot \Delta L + ADDL(m-1)] \cdot N_c \right. \right. \\ & \left. \left. + [P(x_1(0), (m-1)) + Q((m-1), x_2(l))] \cdot N_s \right] \right\} \end{aligned} \quad (3.29)$$

Define a function of an IAWG as

$$\begin{aligned} B_{\text{IAWG}}(l_1, l_2, \lambda) = & C(l_1) \cdot C(l_2) \cdot \sum_{m=1}^M I(m) \exp \left\{ jk \cdot \left[ [L_0 + (m-1) \cdot \Delta L + ADDL(m-1)] \cdot N_c \right. \right. \\ & \left. \left. + [P(x_1(l_1), (m-1)) + Q((m-1), x_2(l_2))] \cdot N_s \right] \right\} \end{aligned} \quad (3.30)$$

Then

$$A_{\text{IAWG}}(l, \lambda) = B_{\text{IAWG}}(0, l, \lambda) \quad (3.31)$$

### 3.4.12. Extinction Ratio Versus the Interleaved Number N

In our definition, extinction ratio is the difference between the maximum value (dB) of the central peak and the maximum value (dB) of the side lobes as shown in figure 3.7. Extinction ratio versus the interleaved number  $N$  for a single wavelength channel was calculated. The result is shown in table 3.6. From table 3.6, we see that the extinction ratio does not change very much with the changes of the number of the interleaves. This can be explained by the multi-beam interferences at

the output star coupler. It is obvious that the total number of waveguides at the input side of the output star coupler remains the same although the interleaves are different. It is still the same number of waveguides that join the interferences at each output port of the output star coupler. The extinction ratio thus remains the same. This is a very important result. It means we can design as many numbers of interleaved AWG as possible.

**Table 3.6** Extinction ratio ( $ER$ ) versus the interleaved number  $N$

$N$	1	2	4	5	6	7	8
$ER$ (dB)	64.0	61.5	57.0	60.5	58.9	55.9	62.0

### 3.5. Realization of a $1 \times N$ All Optical Switch

#### 3.5.1. The Transfer Function of a $1 \times N$ All-Optical Switch

Since a  $1 \times N$  All-Optical Switch consists of two  $N$ -IAWGs and the transfer function of a single  $N$ -IAWG is shown in equation (3.29), we can similarly get the transfer function of the  $1 \times N$  All-Optical Switch. With the result in equation (3.29), the output signal amplitude at one of output ports of star coupler 2 in figure 3.2 can be expressed as

$$A_{2\text{out}}(l, \lambda) = A_{\text{IAWG}}(l, \lambda) \quad (3.32)$$

After the signal output from the  $l$ -th output port of the first  $N$ -IAWG going through its connected phase shifter, the complex amplitude of the signal becomes

$$A_{3\text{out}}(l, \lambda) = A_{2\text{out}}(l, \lambda) \exp[j \cdot \Delta\theta(l, \lambda)] \quad (3.33)$$

This is the signal amplitude at the entrance of star coupler 3 as designated in figure 3.2.  $\Delta\theta(l, \lambda)$  is the phase change caused by the  $l$ -th phase shifter to the signal of wavelength  $\lambda$ . This will be discussed further later.

The output signal from the  $l$ -th phase shifter contributes an output at the  $n$ -th output port of star coupler 4, which can be expressed as

$$B_{\text{out}}(l, n, \lambda) = A_{3\text{out}}(l, \lambda) \cdot B_{\text{IAWG}}(l, n, \lambda) \quad (3.34)$$

Adding contributions of the signals from all the phase shifters, the total output at the  $n$ -th output port of star coupler 4 for the signal of wavelength  $\lambda$  can be expressed as

$$A_{4\text{out}}(n, \lambda) = \sum_{l=1}^{N \cdot N} B_{\text{out}}(l, n, \lambda) \quad (3.35)$$

Equations (3.32)-(3.35) give out the transfer function of a  $1 \times N$  All-Optical Switch.

### 3.5.2. Switching Functionality Verification and Phase Change Information

The functionality of an  $N$ -IAWG has been explained in subsection 3.4.1. To realize the  $1 \times N$  switching functionality with the structure of figure 3.2, all we need to do is to verify that it is possible to switch a signal with one specific wavelength  $\lambda_i$ ,  $i = 1, 2, \dots, N$ , to any one of the output ports from the single input port. This is because signals with different wavelengths are controlled by different sets of phase shifters. Switching a signal of specific wavelength with a specific set of phase shifters

will not affect the signals of other wavelengths. According to the description in section 3.4, the realization of the switching functionality is due to the symmetry of the structure of figure 3.2. For a single wavelength channel, all we need to do is to collect the phase information at its  $N$  related output ports of star coupler 2 and the phase information we needed at the  $N$  related input ports of star coupler 3 to direct the signal to a specific output port at star coupler 4.

Now if we let the wavelength channel  $\lambda_i$  input into the  $n$ -th output port at star coupler 4 in figure 3.2, we should be able to collect its output signal at the  $N$  related input ports of star coupler 3. We denote the phase at the  $k$ -th input port of star coupler 3 as  $\theta_n(k, \lambda_i)$ , where  $k$  is equal to  $i, N+i, 2N+i, \dots$ , or  $(N-I)N+i$ . Then we know if the same single wavelength channel is input from the only central input port of star coupler 1, the signal will be switched to the  $n$ -th output port at star coupler 4 as long as the phase at the  $k$ -th input port of star coupler 3 is  $\theta_n^*(k, \lambda_i)$ , the conjugate of  $\theta_n(k, \lambda_i)$ , for all  $k = i, N+i, 2N+i, \dots, (N-I)N+i$ . We can write these in the following equations

$$A_{2\text{out}}(k, \lambda_i) = |A_{2\text{out}}(k, \lambda_i)| \exp[j \cdot \theta_0(k, \lambda_i)] \quad (3.36)$$

$$A_{3\text{out}}(k, \lambda_i) = |A_{3\text{out}}(k, \lambda_i)| \exp[j \cdot \theta_n^*(k, \lambda_i)] \quad (3.37)$$

As long as equation (3.37) is satisfied, the signal will be switched to the  $n$ -th output port at star coupler 4. From equation (3.36) and (3.37), we can get the phase change needed in the  $k$ -th phase shifter as

$$\Delta\theta(k, \lambda_i) = \theta_n^*(k, \lambda_i) - \theta_0(k, \lambda_i) \quad (3.38)$$

where  $\lambda_i$  is the wavelength of the single channel and  $n$  denotes the destination output port of the signal.  $\theta_0(k, \lambda_i)$  in equations (3.36) and (3.38) is the phase information of channel  $\lambda_i$  at the  $k$ -th output port of star coupler 2. The arrangement of the output ports can be seen in figure 3.8 for the example of a  $1 \times 4$  switch, where only the four phase shifters related to wavelength  $\lambda_0$  are shown.

It can be seen that every single phase shifter needs an independent control signal to adjust the phase needed. Since there are  $N^2$  phase shifters as shown in figure 3.2, there are  $N^2$  degrees of freedom in our  $1 \times N$  structure.

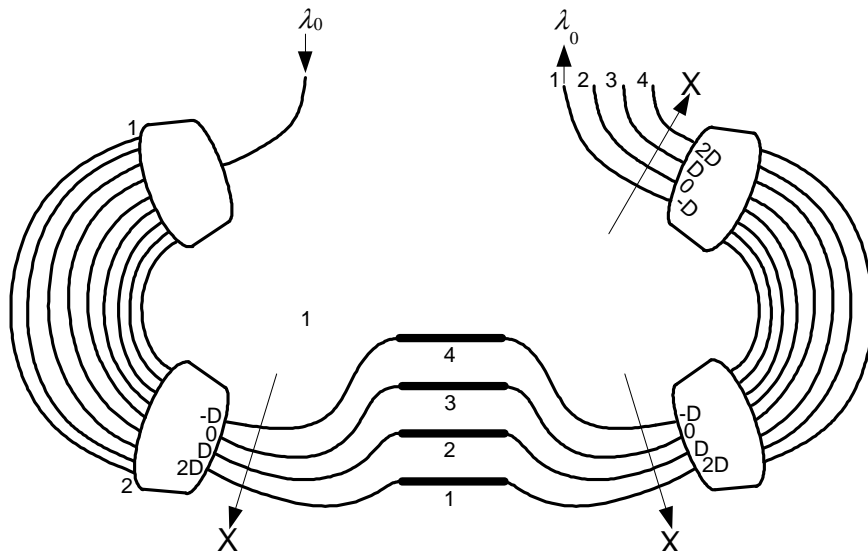


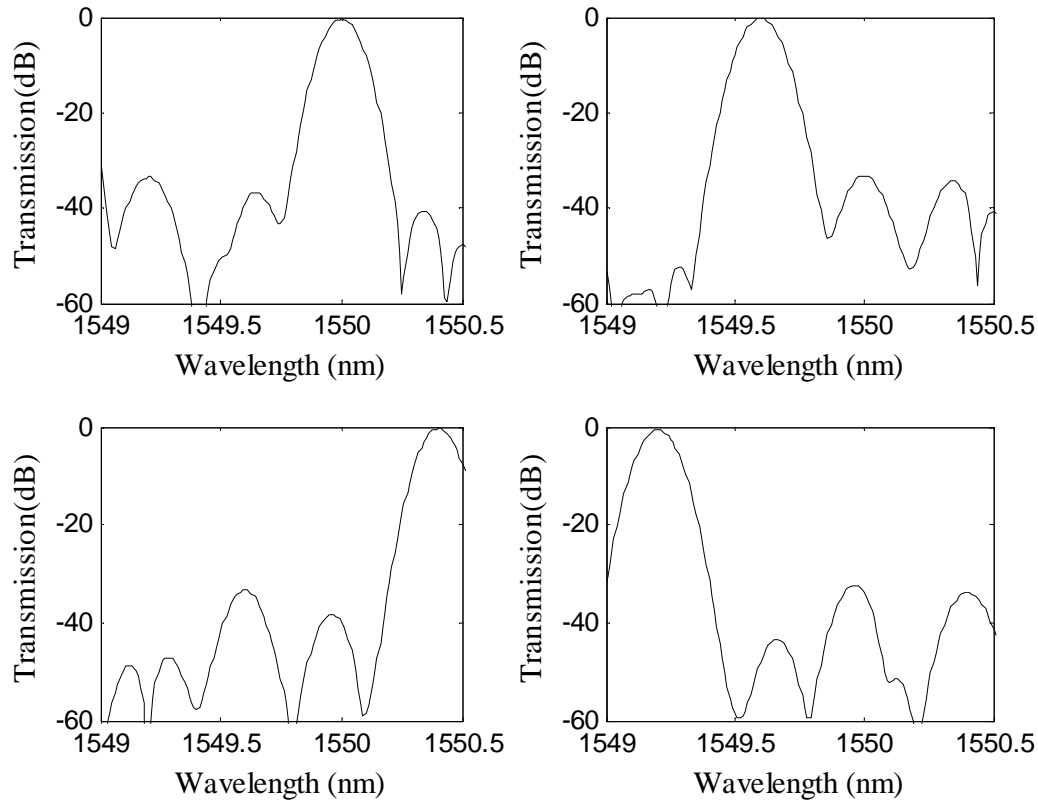
**Figure 3.8** Schematic diagram of  $1 \times 4$  switch for single channel with wavelength  $\lambda_0$ .

### **3.5.3. Simulation Verification -----An Example**

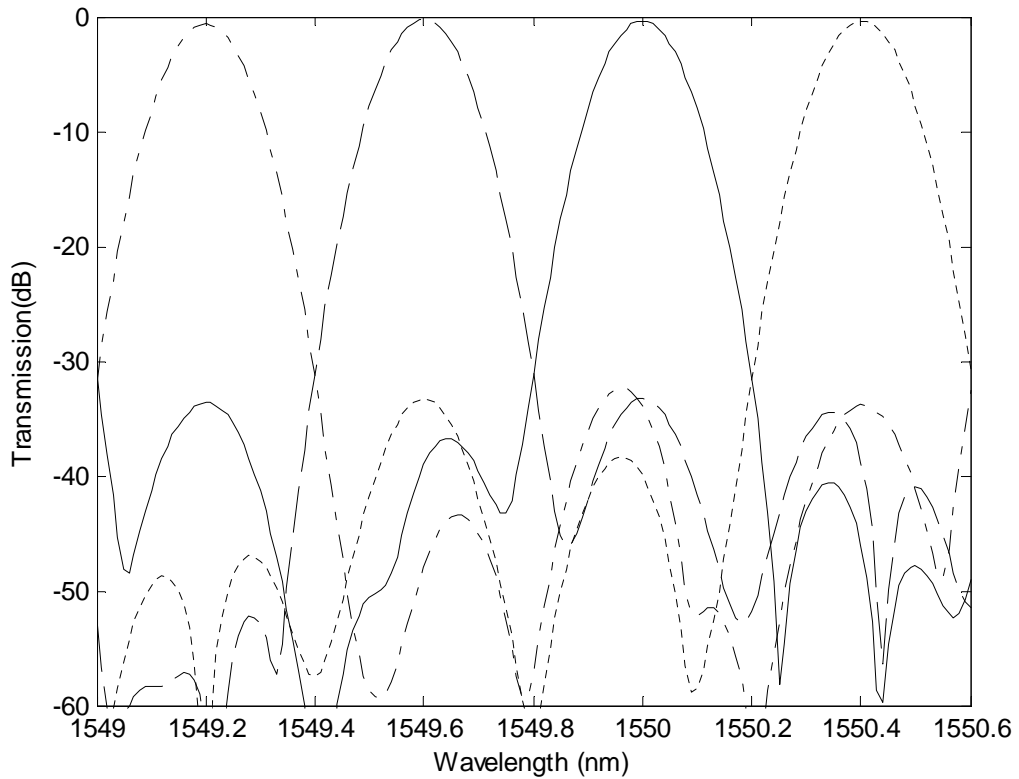
Although the above description of the structure is very reasonable, it is still important to do simulation verifications to obtain the practical requirements on the parameters. This will help us to know if the suggested structure works in real applications. We did a simulation for a  $1 \times 4$  switch. The switching functionality was verified. This specific schematic diagram of a  $1 \times 4$  switch is shown in figure 3.8. In this scheme, the input port at start coupler 1 is located at the center of the star coupler. The output ports at star coupler 2 are located at the positions of  $-D$ ,  $0$ ,  $D$  and  $2D$  as shown in the figure. The locations of the input ports and the output ports at star couplers 3 and 4 are also shown in the figure, where  $X$  is the coordinate,  $D$  is the waveguide separation. To simplify the diagram, we have only drawn four phase shifters here. These phase shifters are connected to the four output ports on the star coupler 2. These four output ports are the only ones to which the signal of wavelength  $\lambda_0$  is directed in the four new central BZs of the 4-IAWG. In our real simulation, however, all  $4 \times 4 = 16$  phase shifters were involved so that the crosstalk caused by this design could be evaluated.

Figure 3.9 shows one of our simulation results. The four channel wavelengths are 1549.2 nm, 1549.6 nm, 1550.0 nm and 1550.4 nm with a channel spacing of 0.4 nm. Figure 3.9 shows that 1550.0 nm channel was switched to output port 1 ( $-D$ ), 1549.6 nm channel to output 2 (0), 1550.4 nm channel to output 3 ( $D$ ) and 1549.2 nm channel to output 4 ( $2D$ ). For comparison, we put these graphs together in figure 3.10.

We can see from figure 3.10 that the crosstalk is about  $-32$  dB or less, which verifies that the scheme is applicable.



**Figure 3.9** Simulation result of  $1 \times 4$  switch for four wavelength channels with wavelengths  $1549.2$  nm,  $1549.6$  nm,  $1550.0$  nm and  $1550.4$  nm with a channel spacing of  $0.4$  nm. The  $1550.0$  nm channel was switched to output port 1,  $1549.6$  nm channel to output 2,  $1550.4$  nm channel to output 3 and  $1549.2$  nm channel to output 4.



**Figure 3.10** Simulation result of  $1 \times 4$  switch for four wavelength channels with wavelengths 1549.2 nm, 1549.6 nm, 1550.0 nm and 1550.4 nm with a channel spacing of 0.4 nm. The crosstalk between channels is round  $-32$  dB or less.

The values of phase changes and related refractive index changes required in the phase shifters in our simulation are presented in tables 5 and 6. Here we have assumed that the equal length waveguides are connected to the phase shifters. The relationship between phase changes and the refractive index changes is

$$\Delta n = \frac{\lambda}{2\pi(LP)} \cdot \Delta\theta \quad (3.39)$$

where  $LP$  is the length of the phase shifters. From table 3.8, we can see that the maximum refractive index change needed in a phase shifter with a length of 2 mm is  $6.918 \times 10^{-4}$  to switch the signal of wavelength 1550 nm. From our previous research [29][34], we know that the maximum possible refractive index change at wavelength 1550 nm is  $\sim 9 \times 10^{-4}$ . This result clearly verifies that the switching is realizable.

**Table 3.7** Phase changes ( $\Delta\theta$ ) needed in phase shifters for each output port selection in 1×4 all-optical switch ( $\lambda = 1550$  nm)

Output Choice	Phase shifter 1 (radians)	Phase shifter 2 (radians)	Phase shifter 3 (radians)	Phase shifter 4 (radians)
Port 1	1.659	-3.128	1.510	3.007
Port 2	0.8362	-0.8091	-2.454	2.184
Port 3	-3.128	1.510	3.007	1.362
Port 4	-0.8091	0.6874	2.184	-2.602

**Table 3.8** Refractive index changes ( $\Delta n$ ) needed in phase shifters with length  $LP = 2$  mm for each output port selection in 1×4 all-optical switch ( $\lambda = 1550$  nm)

Output Choice	Phase shifter 1	Phase shifter 2	Phase shifter 3	Phase shifter 4
Port 1	2.046e-004	-3.858e-004	1.863e-004	3.709e-004
Port 2	1.031e-004	-0.998e-004	-3.027e-004	2.694e-004
Port 3	-3.858e-004	1.863e-004	3.709e-004	1.680e-004
Port 4	-0.998e-004	0.848e-004	2.694e-004	-3.209e-004

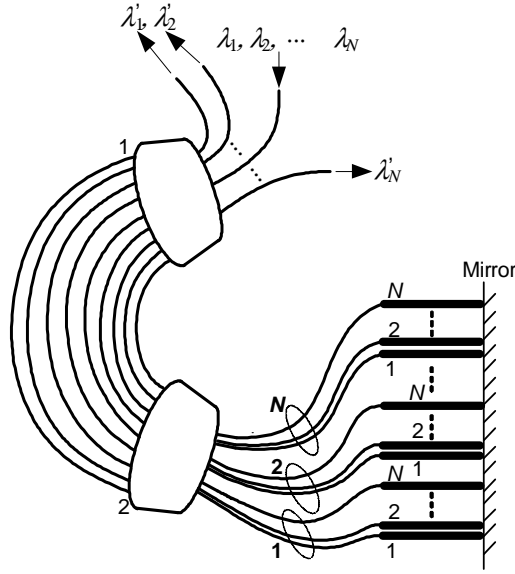


**Figure 3.11** Mirror scheme of  $1 \times N$  all-optical switch.

### 3.5.4. The Scheme of Mirror $1 \times N$ All-Optical Switch

The simulation verifies that the scheme shown in figure 3.2 works. It is based on the symmetry of the structure with two  $N$ -IAWGs. In a real application, there are always some mismatches between the two  $N$ -IAWGs caused in fabrication process. The mismatches can cause extra signal loss. To avoid this shortage, we made modifications on the scheme in figure 3.2 to simplify the structure. The new designed structure is shown in figure 3.11. Instead of using two  $N$ -IAWGs, we use just one in this new design by using a mirror as shown in the figure. The waveguides at the input side of star coupler 1 are all used for the output ports except for the central one. This central input waveguide is used as the only input port for this new design. Obviously there are only  $N-1$  output ports. So this new design essentially is a  $1 \times (N-1)$  all-

optical switch. The simplicity of the structure is the tradeoff of one less output channel. But the advantage of this scheme is quite clear. By using the same  $N$ -IAWG for input and output in the scheme shown in figure 3.11, the possible mismatch between the input and output IAWGs in the previous scheme is successfully avoided. We can always have the peak value at the output ports as long as the phase change requirements in the phase shifters are satisfied. Figure 3.12 shows a simulation result for the mirror structure for  $N = 4$ . As we mentioned above, three channels can be applied to the structure.

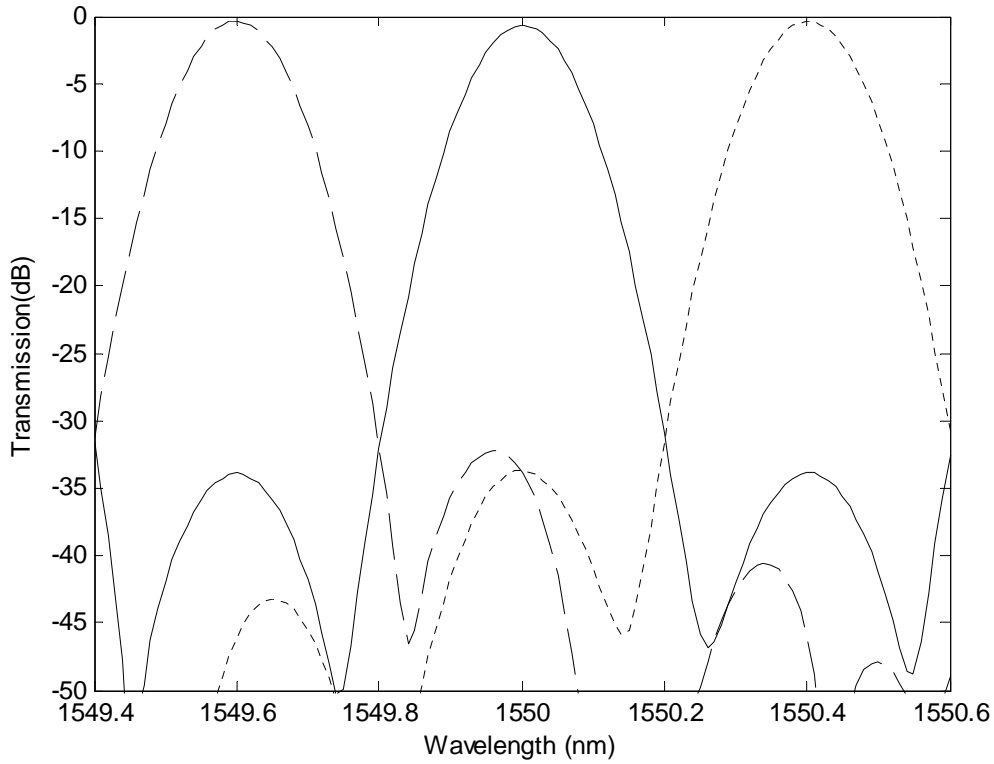


**Figure 3.12** Simulation result of the mirror scheme of  $1 \times (N-1)$  all-optical switch for  $N = 4$ .

### **3.6. Conclusion**

In this chapter, we first proposed a uniquely fully functional non-blocking  $N \times N$  WDM all-optical switch. Then we presented a complete theory or method for designing a  $1 \times N$  all optical switch, which is the key element in the designing of an  $N \times N$  WDM all-optical switch. Since the  $1 \times N$  all optical switch is an application of  $N$ -AWG, the general rule for the design of an  $N$ -IAWG was thus developed and presented. It was found that multiple solutions could be obtained by using the general rule. The comparison between the results obtained by using the general rule and the results from other papers showed that the general rule is practical and the results previously published are special cases under this general rule. It allows us to find the optimum additional lengths added to the arrayed waveguides of an AWG to construct an  $N$ -IAWG. By applying the general rule, any number of interleaved IAWGs can be developed. The  $1 \times N$  freely switching functionality for a single wavelength channel was then discussed. Various simulation results were presented and the feasibility of this proposed switch configuration was discussed. It is also important to note that the  $1 \times N$  switch building block is a planar device with no waveguide crossings so that it can be monolithically integrated into more complicated devices. Finally a unique reflective  $1 \times (N-1)$  scheme based on an  $N$ -IAWG was presented, which significantly simplifies the device configuration. A numerical simulation carried out for this structure verified its feasibility and the advantages of this structure were also discussed. The theoretical foundation established in this chapter for the design of an any-to-any  $N \times N$  optical wavelength switch is generally applicable to many material

systems and will be useful in the design of future large-scale optical integrated circuits.

## **4. Carrier Induced Refractive Index Changes in GaN/AlGaN Semiconductors**

### **4.1 Introduction**

In chapter 2, we briefly introduced the design of waveguide devices with carrier-controlled refractive indices, especially the design of carrier-controlled AWG all-optical switch. In chapter 3, we presented the scheme of  $1 \times N$  all-optical switch, which requires carrier-controlled phase shifters, which can be made from III-V semiconductors. Group III-V semiconductors are playing an increasingly important role in integrated optics, because they offer the potential for integration of sources, detectors, switches, and modulators onto the same chip [35]. Guided-wave switching and modulation can be achieved by electro-optical effect where the refractive index of the material can be controlled by the electric field across it. Also, free-carrier-induced optical switching in InGaAsP-InP has been demonstrated [36], where the optical switch was realized by using complete internal reflection, due to the free-carrier-induced refractive index decrease at some designed area. In [36], the carrier-induced refractive index of the same material system was also roughly measured, at the order of  $10^{-3}$ , with the change of the current density. In [37], optical generation of free carriers was applied to control the transmission in InGaAsP epilayers upon InP substrates. Efficient GaAs-AlGaAs depletion-mode phase modulators were fabricated in which both electric field and carrier effects were significant [38][39]. Carrier-induced refractive index changes are also important for laser design [40][41]. The

refractive index change produced by injection of free carriers in InP, GaAs, and InGaAsP have been theoretically estimated in [35], in which three basic phenomena of III-V semiconductor materials were discussed: bandfilling, band-gap shrinkage, and free-carrier absorption (plasma effect).

In this dissertation, since our attention is focused on the application of III-nitride-based photonic devices, we will first review the theory of these three important carrier effects in this chapter, and then we will utilize them to estimate the carrier-induced refractive index changes in GaN and AlGaN. As we have mentioned earlier, AlGaN semiconductors are highly transparent in the infrared area, and their refractive indices can be modified by the control of Al concentration. These materials are good candidates for planar lightwave circuits. They can be made into a fast switchable optical PHASAR to realize all-optical switches because their refractive indices are also dynamically adjustable through carrier-injection [29]. Previous studies of carrier-induced refractive index change in GaN semiconductors were mainly focused on the UV and visible wavelength regions near the bandgap; it is important to extend these studies into the infrared wavelength region for optical communications. The efficiency of carrier-induced index change is a critical parameter for switchable PHASAR applications.

## 4.2 Carrier-Induced Refractive Index Change in Semiconductors

### 4.2.1 Bandfilling

Bandfilling effect occurs when semiconductors are doped or injected with free carriers. It is, essentially, the decrease in the absorption of the photons with energies slightly above the nominal bandgap of the semiconductor. This phenomenon is also known as the Burstein-Moss effect [42][43]. In the case of n-type semiconductors, there is a low density of states in the conduction band so that a small number of electrons can fill the conduction band to an appreciable depth. With the lowest energy states in the conduction band being filled, the electrons in the valence band would require more energy than that needed to overcome the nominal bandgap to be optically excited into the conduction band, as shown in figure 4.1. Therefore, a decrease is observed in the absorption coefficient at energies slightly above the bandgap. The situation in a p-type semiconductor is similar, except that a smaller bandfilling effect happens for a given carrier concentration due to the much larger effective mass of the hole [35], which means a higher density of states.

When parabolic band structure is assumed, for a direct-gap semiconductor, as shown in figure 4.1, the optical absorption near the bandgap is given by the square-root law [35]:

$$\alpha_0(E) = \frac{C}{E} \sqrt{E - E_g} \quad (E \geq E_g)$$
$$\alpha_0(E) = 0 \quad (E < E_g) \quad (4.1)$$

where  $E = \hbar\omega$  is the photon energy,  $E_g$  is the band-gap energy, and  $C$  is a constant involving materials parameters, matrix elements between periodic parts of the Bloch states at the band edges, and fundamental constants [43]. At direct gap for III-V semiconductors, the valence bands are degenerated, due to the existence of both light- and heavy-hole bands contributing to the absorption process, as shown in figure 4.1. In this case, the equation of optical absorption near the bandgap, equation (4.1), is modified as:

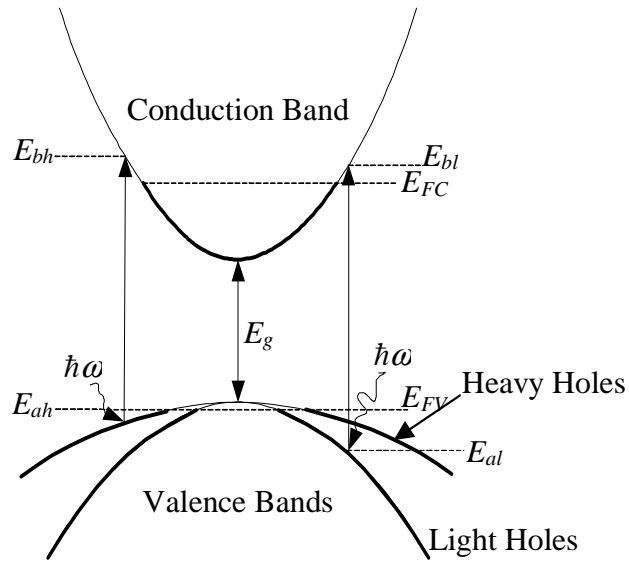


**Figure 4.1** Energy band structure and bandfilling effect for direct-gap semiconductor. Absorption of a photon can occur only between occupied valence band states and unoccupied conduction band states. (Ref. [35])

$$\alpha_0(E) = \frac{C_{hh}}{E} \sqrt{E - E_g} + \frac{C_{lh}}{E} \sqrt{E - E_g} \quad (E \geq E_g)$$

$$\alpha_0(E) = 0 \quad (E < E_g) \quad (4.2)$$

where  $C_{hh}$  and  $C_{lh}$  refer to heavy and light holes, respectively. The values of  $C$  for different materials can be estimated by fitting equation (4.1) to experimental absorption data [44].

The constants  $C_{hh}$  and  $C_{lh}$  in the above equation can be calculated from the following equations [35]:

$$C_{hh} = C \left( \frac{\mu_{ehh}^{3/2}}{\mu_{ehh}^{3/2} + \mu_{elh}^{3/2}} \right) \quad (4.3a)$$

$$C_{lh} = C \left( \frac{\mu_{elh}^{3/2}}{\mu_{ehh}^{3/2} + \mu_{elh}^{3/2}} \right) \quad (4.3b)$$

where  $\mu_{ehh}$  and  $\mu_{elh}$  are the reduced effective masses of the electron-hole pairs [43], which can be obtained from

$$\mu_{ehh} = \left( \frac{1}{m_e} + \frac{1}{m_{hh}} \right)^{-1} \quad (4.4a)$$

$$\mu_{elh} = \left( \frac{1}{m_e} + \frac{1}{m_{lh}} \right)^{-1} \quad (4.4b)$$

where  $m_e$ ,  $m_{hh}$  and  $m_{lh}$  are the effective masses of electrons, heavy holes, and light holes, respectively.

The values of  $C$ ,  $C_{hh}$  and  $C_{lh}$  are given in table 4.1 [35]. It can be seen that about two-thirds of the absorption results from heavy holes and one-third from light holes in all three materials.

**Table 4.1:** Values of Semiconductor Parameters (T = 300 K) [35]:

	InP	GaAs	In <sub>0.82</sub> Ga <sub>0.18</sub> As <sub>0.40</sub> P <sub>0.60</sub>
$E_g$ (eV)	1.34	1.42	1.08
$C(\text{cm}^{-1}\cdot\text{s}^{-1/2})$	$4.4 \times 10^{12}$	$2.3 \times 10^{12}$	$3.2 \times 10^{12}$
$C_{hh}(\text{cm}^{-1}\cdot\text{s}^{-1/2})$	$2.8 \times 10^{12}$	$1.5 \times 10^{12}$	$2.1 \times 10^{12}$
$C_{lh}(\text{cm}^{-1}\cdot\text{s}^{-1/2})$	$1.6 \times 10^{12}$	$7.8 \times 10^{11}$	$1.1 \times 10^{12}$
$\epsilon_s$	12.4	13.1	13.0
$n$	3.4	3.6	3.6
$m_e(m_0)$	0.075	0.066	0.064
$m_{hh}(m_0)$	0.56	0.45	0.51
$m_{lh}(m_0)$	0.12	0.084	0.086
$m_{dh}(m_0)$	0.60	0.47	0.53
$\mu_{ehh}(m_0)$	0.066	0.058	0.057
$\mu_{elh}(m_0)$	0.046	0.037	0.037
$N_c(\text{cm}^{-3})$	$5.2 \times 10^{17}$	$4.3 \times 10^{17}$	$4.1 \times 10^{17}$
$N_v(\text{cm}^{-3})$	$1.2 \times 10^{19}$	$8.3 \times 10^{18}$	$1.1 \times 10^{19}$
$\chi_{cr}(\text{cm}^{-3})$	$1.3 \times 10^{17}$	$7.4 \times 10^{16}$	$7.0 \times 10^{16}$
$\kappa$		0.13	

In the case of bandfilling, a state in the conduction band can be occupied by an electron, and a state in the valence band can be empty of electrons. If we denote an energy in the valence band as  $E_a$  and an energy in the conduction band as  $E_b$ , the absorption coefficient of an injected semiconductor is [35][45]:

$$\alpha(N, P, E) = \alpha_0(E)[f_v(E_a) - f_c(E_b)] \quad (4.5)$$

where  $N$  and  $P$  are the concentrations of free electrons and holes, respectively;  $\alpha_0$  represents the absorption of pure materials in the absence of injection;  $f_c(E_b)$  is the probability of a conduction band state with energy  $E_b$  being occupied by an electron; and  $f_v(E_a)$  is the probability of a valence band state with energy  $E_a$  being occupied by an electron. The values of  $E_a$  and  $E_b$  are uniquely defined for a given photon energy. In the case as shown in figure 4.1, there are two values for each because of the degeneracy of the valence band. From [35], we have:

$$E_{ah,al} = (E_g - E) \left( \frac{m_e}{m_e + m_{hh,lh}} \right) - E_g \quad (4.6a)$$

$$E_{bh,bl} = (E - E_g) \left( \frac{m_{hh,lh}}{m_e + m_{hh,lh}} \right) \quad (4.6b)$$

where the subscripts  $h$  and  $l$  refer to heavy and light holes, respectively.

The probabilities  $f_c$  and  $f_v$  in equation (4.5) are given by the Fermi-Dirac distribution functions, which were given in [35]:

$$f_c(E_{bh,bl}) = \left[ 1 + e^{(E_{bh,bl} - E_{F_c})/(k_B T)} \right]^{-1} \quad (4.7a)$$

$$f_v(E_{ah,al}) = \left[ 1 + e^{(E_{ah,al} - E_{F_v})/(k_B T)} \right]^{-1} \quad (4.7b)$$

where  $k_B$  is Boltzmann's constant, and  $T$  is the absolute temperature.  $E_{F_c}$  and  $E_{F_v}$  are the carrier-dependent quasi-Fermi levels. They can be estimated by the Nilsson approximation [35]:

$$E_{F_c} = \left\{ \ln\left(\frac{N}{N_c}\right) + \frac{N}{N_c} \left[ 64 + 0.05524 \frac{N}{N_c} \cdot \left( 64 + \sqrt{\frac{N}{N_c}} \right) \right]^{-(1/4)} \right\} k_B T \quad (4.8a)$$

$$E_{F_v} = - \left\{ \ln\left(\frac{P}{N_v}\right) + \frac{P}{N_v} \left[ 64 + 0.05524 \frac{P}{N_v} \left( 64 + \sqrt{\frac{P}{N_v}} \right) \right]^{-(1/4)} \right\} k_B T - E_g \quad (4.8b)$$

where the zero of energy is defined to be at the conduction band minimum.  $N_c$  is the effective density of states in the conduction band such that

$$N_c = 2 \left( \frac{m_e k_B T}{2\pi\hbar^2} \right)^{3/2} \quad (4.9a)$$

and  $N_v$  is the effective density of states in the valence bands such that

$$N_v = 2 \left( \frac{m_{dh} k_B T}{2\pi\hbar^2} \right)^{3/2} \quad (4.9b)$$

where  $m_{dh}$  is the density-of-states effective mass for holes such that

$$m_{dh} = \left( m_{hh}^{3/2} + m_{lh}^{3/2} \right)^{3/2} \quad (4.10)$$

We can see that bandfilling influences the optical absorption of the material. This change can be expressed as

$$\Delta\alpha(N, P, E) = \alpha(N, P, E) - \alpha_0(E) \quad (4.11)$$

where  $\alpha(N, P, E)$  is the absorption coefficient of an injected semiconductor,  $N$  and  $P$  are the concentrations of free electrons and holes, respectively,  $E = \hbar\omega$  and  $\alpha_0$

represents the absorption of pure materials in the absence of injection. Combining equations (4.2), (4.5) and (4.11) yields:

$$\begin{aligned}\Delta\alpha(N, P, E) = & \frac{C_{hh}}{E} \sqrt{E - E_g} [f_v(E_{ah}) - f_c(E_{bh}) - 1] \\ & + \frac{C_{lh}}{E} \sqrt{E - E_g} [f_v(E_{al}) - f_c(E_{bl}) - 1]\end{aligned}\quad (4.12)$$

The only materials parameters required for equation (4.12) are the effective masses of electrons and holes, the energy gap, and the fitting constant  $C$ . The values of these parameters along with other important physical parameters for InP, GaAs and InGaAsP are presented in table 4.1 [35].

Since the relationship between the refractive index  $n$  and the absorption coefficient  $\alpha$  is [35]:

$$n(E) = 1 + \frac{2c\hbar}{e^2} P \int_0^\infty \frac{\alpha(E')}{E'^2 - E^2} dE' \quad (4.13)$$

where  $c$  is the speed of light,  $e$  is the electron charge,  $E = \hbar\omega$  is the photon energy, and  $P$  indicates the principle value of the integral. The change of the refractive index caused by the injected carrier can thus be expressed as [35]:

$$\Delta n(N, P, E) = \frac{2c\hbar}{e^2} P \int_0^\infty \frac{\Delta\alpha(N, P, E')}{E'^2 - E^2} dE' \quad (4.14)$$

Equation (4.14) shows the change of the refractive index due to the bandfilling effect. Since in all cases, bandfilling decreases the absorption coefficient at a fixed energy, we thus find that the refractive index of the material also decreases due to the bandfilling effect.

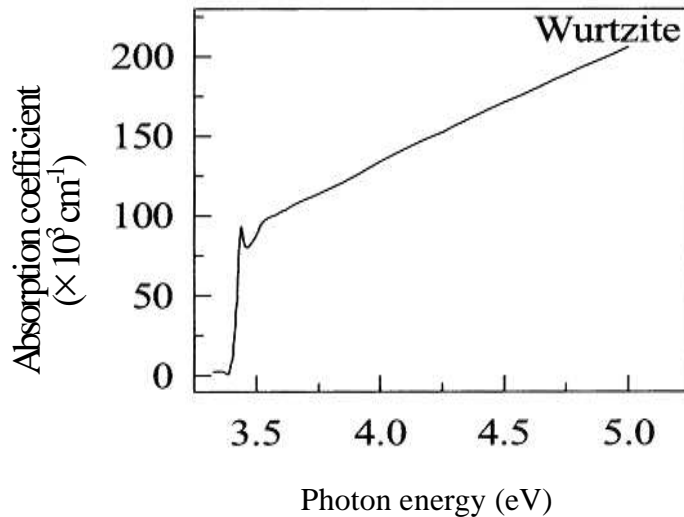


**Figure 4.2** The absorption coefficient versus the photon energy for the GaN layer grown on sapphire.  $T = 293 \text{ K}$  [46][47]

We have applied the above theory of the bandfilling effect to GaN semiconductor materials. The major material parameters of GaN used in the calculation were extracted from reference [46]. The data is shown in table 4.2. In table 4.2, parameter  $C$  is obtained by fitting equation (4.1) to the absorption coefficient versus the photon energy for the GaN layer grown on sapphire as shown in figure 4.2 [47]. The data that was not present in [46] can be calculated with the equations given above.

It was noticed that there are two dielectric constants (static and high frequency). The data for InP are 12.5 (static) and 9.61 (high frequency). The reference [35] took the first one (static) in the calculation. Similarly, the static dielectric constant was taken for our calculation. For GaN materials, the static one is

either 8.9 (Wurtzite) or 9.7 (Zinc Blende). So we have taken 8.9 for Wurtzite structure. The parameter  $\kappa = 0.13$  is based on [35], which needs to be verified in the future.

**Table 4.2:** Values of GaN Semiconductor Parameters (T = 300 K):

$E_g(\text{eV})$	3.39
$C(\text{cm}^{-1}\cdot\text{s}^{-1/2})$	$2.8 \times 10^{13}$
$C_{hh}(\text{cm}^{-1}\cdot\text{s}^{-1/2})$	$1.79 \times 10^{13}$
$C_{lh}(\text{cm}^{-1}\cdot\text{s}^{-1/2})$	$1.01 \times 10^{13}$
$\epsilon_s$	8.9
$n$	2.335
$m_e(m_0)$	0.2
$m_{hh}(m_0)$	1.4
$m_{lh}(m_0)$	0.3
$m_{dh}(m_0)$	1.49
$\mu_{ehh}(m_0)$	0.18
$\mu_{elh}(m_0)$	0.12
$N_c(\text{cm}^{-3})$	$2.2429 \times 10^{18}$
$N_v(\text{cm}^{-3})$	$4.5659 \times 10^{19}$
$\chi_{cr}(\text{cm}^{-3})$	$6.6 \times 10^{18}$
$\kappa$	0.13

The absorption coefficient versus the photon energy for the GaN layer grown on sapphire is different at different temperatures. Figure 4.3 shows this relationship at  $T = 10$  K. This data was generously provided by Dr. Wei Shan, one of the authors of [47].

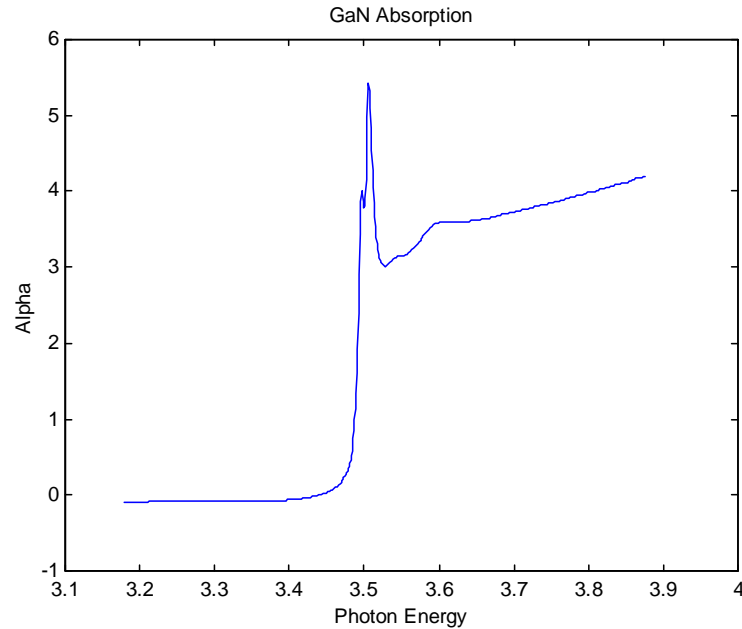


**Figure 4.3** The absorption coefficient versus the photon energy for the GaN layer grown on sapphire.  $T = 10$  K (Provided by Dr. Wei Shan)

Using equation (4.12), and assuming that  $N = P$ , at room temperature we can obtain  $\Delta\alpha$  as plotted in figure 4.4. (It was also assumed that the free-carrier density is entirely due to injection.) From the figure, we can see that the change in absorption

begins at the bandgap and decreases for energies well above the gap. Maximum values for  $\Delta\alpha$  range from  $79 \text{ cm}^{-1}$  for  $10^{16} \text{ /cm}^3$  to  $4.5 \times 10^4 \text{ cm}^{-1}$  for  $10^{19} \text{ /cm}^3$ .

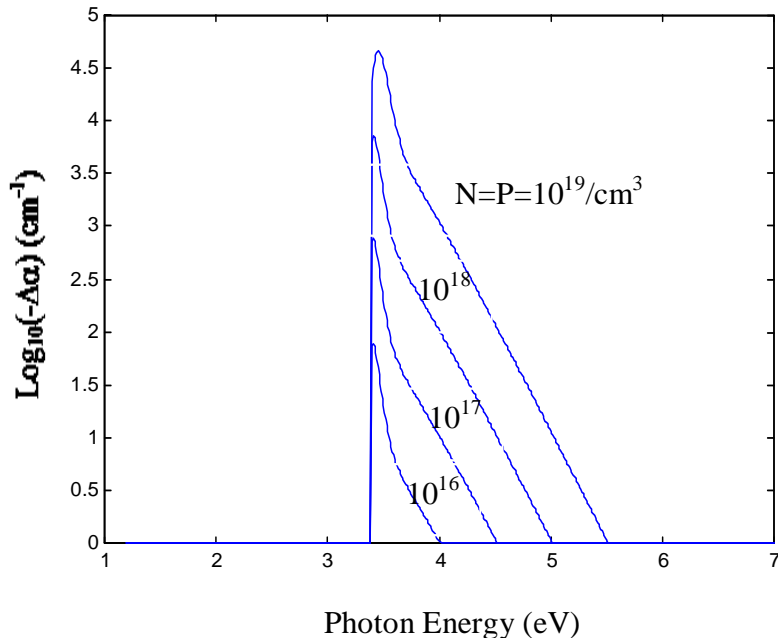


**Figure 4.4** Change in absorption due to electron-hole injection and the resulting bandfilling in GaN. Note: the vertical values are in logarithmic notation.

With  $\Delta\alpha$  being calculated as above, and under the same conditions, we can apply equation (4.14) to numerically calculate (integrate) the change of refractive index ( $\Delta n$ ) by using Simpson's rule. From equation (4.14), we can see that only when  $\Delta\alpha$  is within a few tenths of an electron volt of  $E_g$  does it make a significant contribution to  $\Delta n$ , since the decay in  $\Delta\alpha$  for energies well above  $E_g$  is amplified by

the large denominator in the integral. The results of  $\Delta n$  due to the bandfilling effect in the GaN materials are shown in figure 4.5.

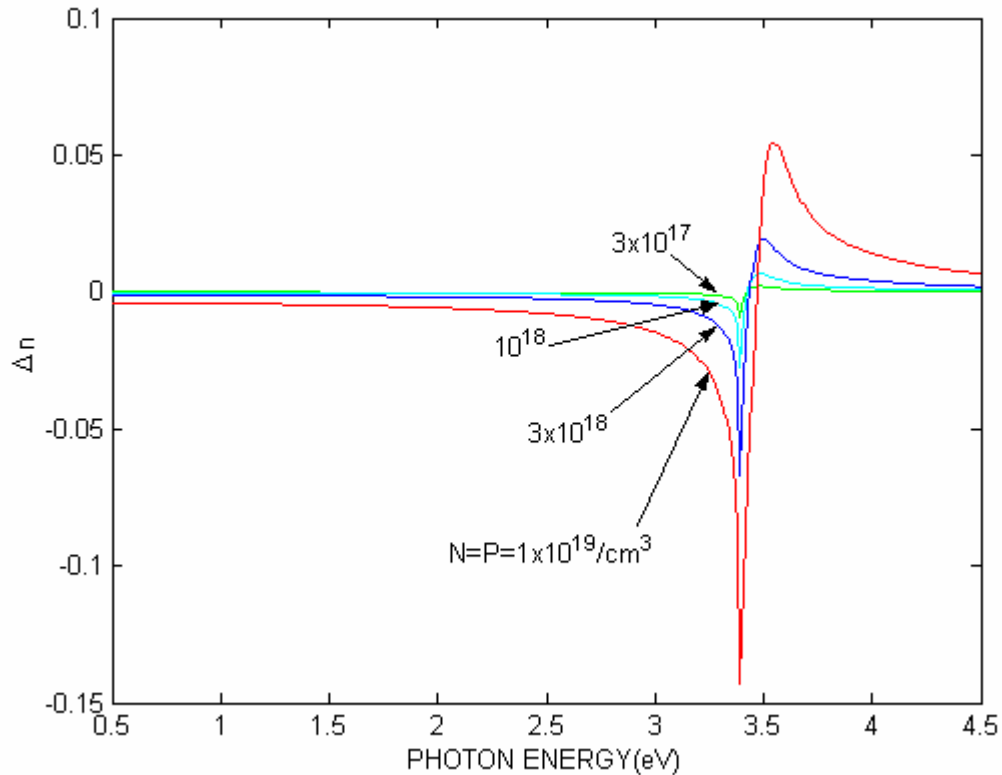


**Figure 4.5** Change in refractive index due to the bandfilling effect of GaN.  
 $N = P = 3.0 \times 10^{17}, 1.0 \times 10^{18}, 3.0 \times 10^{18}, 1.0 \times 10^{19} \text{ cm}^{-3}$ .

The sharp peaks in the  $\Delta n$  near the bandgap predicted by the theory would not be seen in experiments, because they are the results of the assumption that the unperturbed absorption follows the square-root law, abruptly going to zero at  $E_g$ . In reality, materials exhibit absorption extending to energies below the nominal bandgap.

This absorption tail, known as the Urbach edge, results from phonons, impurities, excitons, and internal electric fields [35][48]. The presence of this tail does not, however, have a significant effect on the estimation of the  $\Delta n$  for energies of long wavelength that are substantially below the bandgap.

To illustrate the change of refractive index  $\Delta n$  versus wavelength more directly, we have used figure 4.6 to show the bandfilling effect at three different carrier-injection levels:  $N = 7 \times 10^{18} \text{ cm}^{-3}$  (solid line),  $3 \times 10^{19} \text{ cm}^{-3}$  (dashed line), and  $6 \times 10^{19} \text{ cm}^{-3}$  (dotted line). From the figure, we can see that because carrier-induced index changes are largely asymmetrical around the material bandgap, the value is reduced significantly as the wavelength increases.

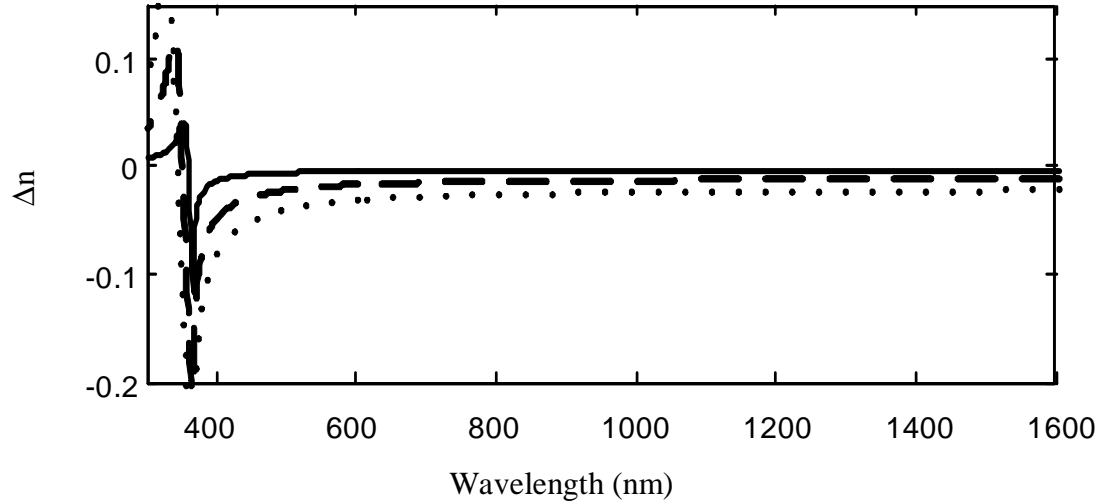


**Figure 4.6** Index change versus signal wavelength due to the bandfilling effect in GaN. Solid line:  $N = 7 \times 10^{18} \text{ cm}^{-3}$ , dashed line:  $N = 3 \times 10^{19} \text{ cm}^{-3}$ , dotted line:  $N = 6 \times 10^{19} \text{ cm}^{-3}$ . (Ref. [34])

In figure 4.7, the refractive index change as a function of carrier density of GaN for fixed photon energy of 0.8 eV, corresponding to the photon wavelength of 1550 nm, has been plotted. From figure 4.7, we see that  $\Delta n$  is linear in carrier concentration in the range of  $10^{16}$ -  $10^{18} \text{ cm}^{-3}$ . This can be expressed by

$$\Delta n(1550\text{nm}) \equiv -4.24 \times 10^{-22} \chi, \quad (4.15)$$

where  $\chi = N = P$ .

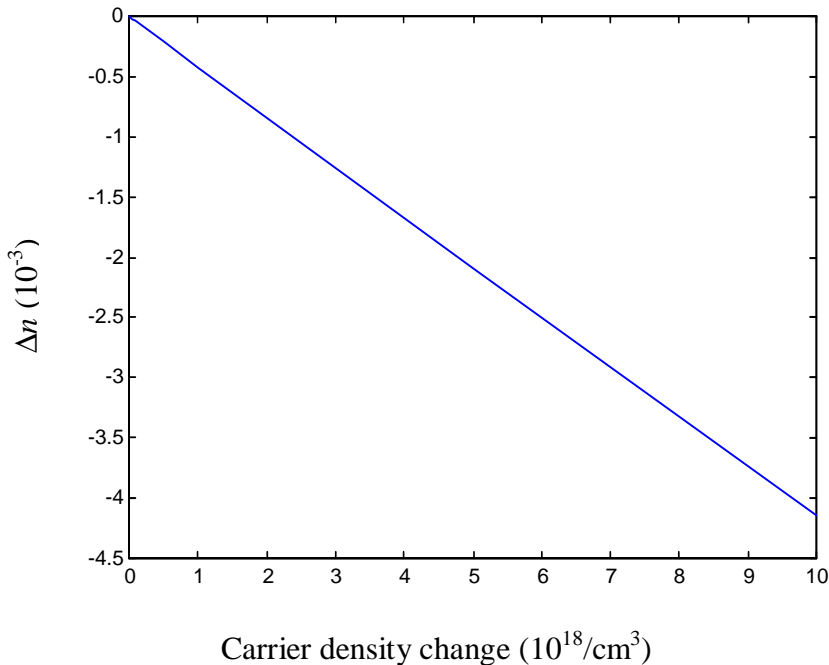


**Figure 4.7** Change of refractive index versus carrier density at 1550 nm for GaN.

#### 4.2.2 Bandgap Shrinkage

On the other hand, bandgap shrinkage is caused by injected free carriers, but not by doped carriers. The increase of free-carrier concentration decreases the energy of the conduction band and increases the energy of the valence band. This is because the electron wave functions overlap. When they overlap, a gas of interacting electrons with lower energy level is formed at the bottom of the conduction band, while a gas of interacting holes with higher level is formed at the top of the valence band. This causes the shrinkage of the bandgap, which generates a red shift of the absorption curve. The following model can be adopted for this shrinkage [35]:

$$\Delta E_g(x) = \frac{\kappa}{\epsilon_s} \left(1 - \frac{x}{x_{cr}}\right)^{1/3} \quad x \geq x_{cr}$$

$$\Delta E_g(x) = 0 \quad x < x_{cr} \quad (4.16)$$

where  $\kappa$  is a fitting parameter,  $\epsilon_s$  is the relative static dielectric constant of the semiconductor,  $x$  is the concentration of free electrons or holes, and  $x_{cr}$  is the critical concentration of free carriers. The value of  $x_{cr}$  adopted in [35] is expressed as:

$$\chi_{cr}(x) = 1.6 \times 10^{24} \left( \frac{m_e}{1.4\epsilon_s} \right)^3 \quad (4.17)$$

with  $x_{cr}$  in  $\text{cm}^{-3}$ . By using equation (4.17), a value  $\chi_{cr} \cong 7 \times 10^{16} / \text{cm}^3$  was predicted for n-GaAs. For GaN, the predicted value was  $\chi_{cr} \cong 6.6 \times 10^{18} / \text{cm}^3$ .

Basically, the bandgap shrinkage occurs when the injected free carriers have a large concentration in which the correlation effects among the free carriers become significant. The change in absorption due to shrinkage is predicted to be:

$$\Delta\alpha(\chi, E) = \frac{C}{E} \sqrt{E - E_g - \Delta E_g(\chi)} - \frac{C}{E} \sqrt{E - E_g} \quad (4.18)$$

Equation (4.18) predicts that  $\Delta\alpha$  is always positive and largest near the bandgap since  $\Delta E_g$  is negative [from equation (4.16)]. The change in refractive index caused by the bandgap shrinkage can be calculated by applying equation (4.14) to the  $\Delta\alpha$  in equation (4.18). The result for GaN with electron-hole carrier concentrations of  $7 \times 10^{18}$ ,  $3 \times 10^{19}$  and  $6 \times 10^{19} \text{ cm}^{-3}$  are given in figure 4.8.

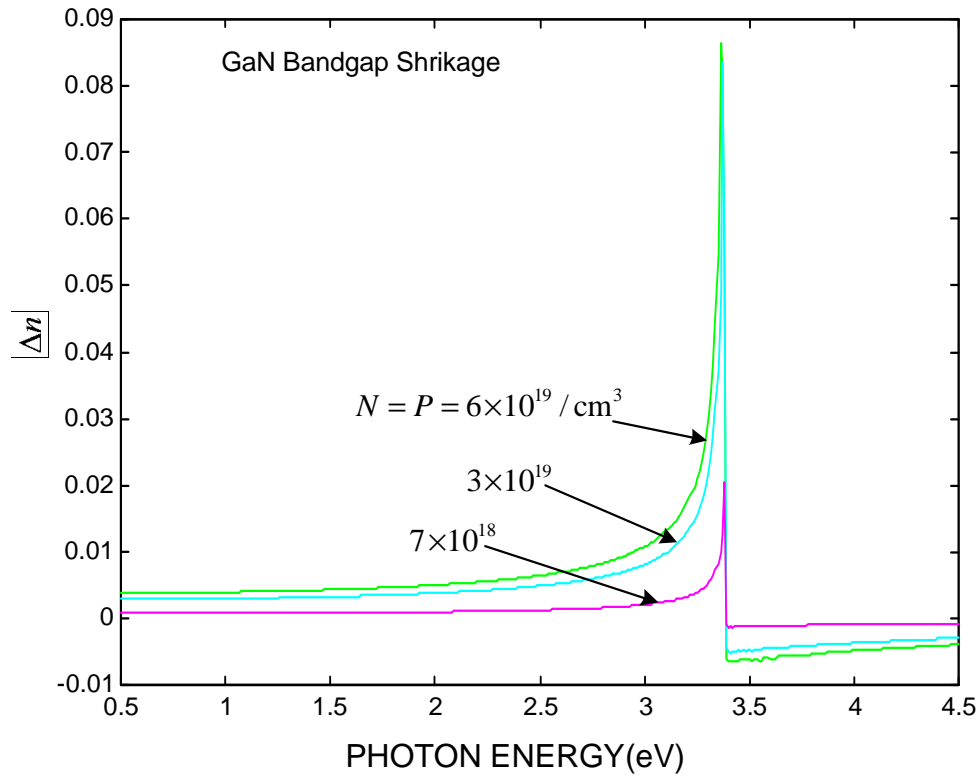


**Figure 4.8** Change of refractive index of GaN due to electron-hole injection and the resulting band-gap shrinkage [calculated from (4.18) and (4.14)].

To illustrate the change of refractive index  $\Delta n$  versus wavelength more directly in the bandgap shrinkage of GaN materials, we have used figure 4.9 to show the effect at three different carrier-injection levels:  $N = 7 \times 10^{18} \text{ cm}^{-3}$  (solid line),  $3 \times 10^{19} \text{ cm}^{-3}$  (dashed line) and  $6 \times 10^{19} \text{ cm}^{-3}$  (dotted line). From the figure, we can see that carrier-induced index changes are largely asymmetrical around the material bandgap, and the value is reduced significantly as the wavelength increases.

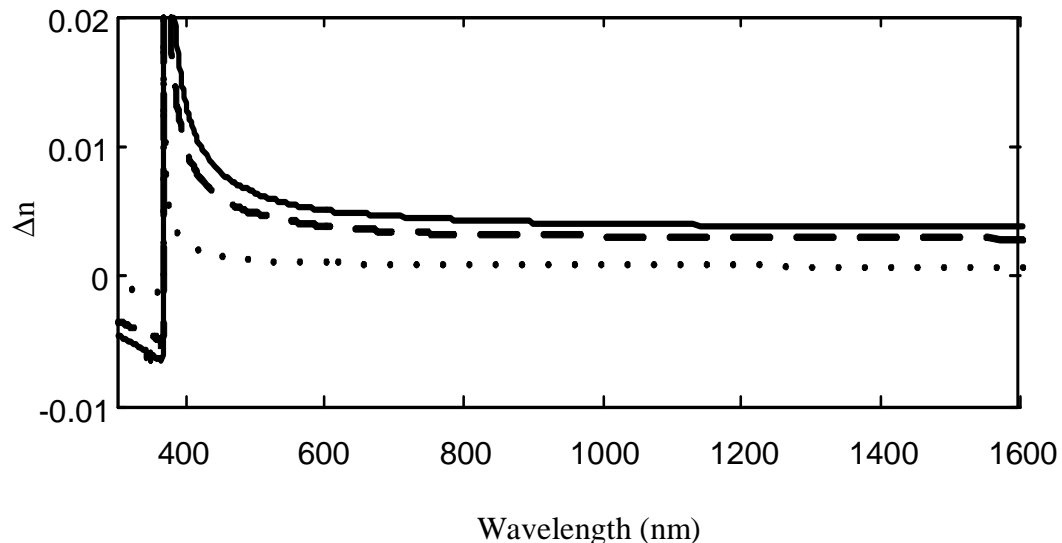


**Figure 4.9** Index change versus signal wavelength due to bandgap shrinkage effect of GaN. Solid line:  $N = 7 \times 10^{18} \text{ cm}^{-3}$ , dashed line:  $N = 3 \times 10^{19} \text{ cm}^{-3}$ , dotted line:  $N = 6 \times 10^{19} \text{ cm}^{-3}$ . (Ref. [34])

#### 4.2.3 Free-Carrier Absorption

Besides the interband absorption due to the effects of bandfilling and bandgap shrinkage, a free carrier can absorb a photon and move to a higher energy level within

a band. This is referred to as free-carrier absorption or the plasma effect. The corresponding change in refractive index is given by [35][49]:

$$\Delta n = -\left(\frac{e^2 \lambda^2}{8\pi^2 c^2 \epsilon_0 n}\right) \left( \frac{N}{m_e} + \frac{P}{m_h} \right) \quad (4.19)$$

where  $\lambda$  is the photon wavelength. Unlike the bandfilling and band-gap shrinkage calculations, a numerical integration of absorption data is not necessary in this case. Equation (4.19) can be changed into a more convenient form [35]:

$$\Delta n = \frac{-6.9 \times 10^{-22}}{n E^2} \left\{ \frac{N}{m_e} + P \left( \frac{m_{hh}^{1/2} + m_{lh}^{1/2}}{m_{hh}^{3/2} + m_{lh}^{3/2}} \right) \right\} \quad (4.20)$$

where  $n$  is the refractive index of the material;  $E = \hbar\omega$ ,  $m_e$ ,  $m_{hh}$ , and  $m_{lh}$  are the effective masses of electrons, heavy holes, and light holes, respectively; and  $N$  and  $P$  are the concentrations of free electrons and holes, respectively. It should be noted that the energy should be expressed in eV and  $N$  and  $P$  in  $\text{cm}^{-3}$  in order to use equation (4.20).

From either equation (4.19) or (4.20), we can see that the sign of  $\Delta n$  from plasma effect is always negative. This adds to the bandfilling effect for energies below the bandgap. Because of the  $\lambda^2$  dependence, as shown in equation (4.19), the plasma effect increases as the photon energy decreases below the bandgap. Figure 4.10 shows the refractive index change of GaN due to the plasma effect.

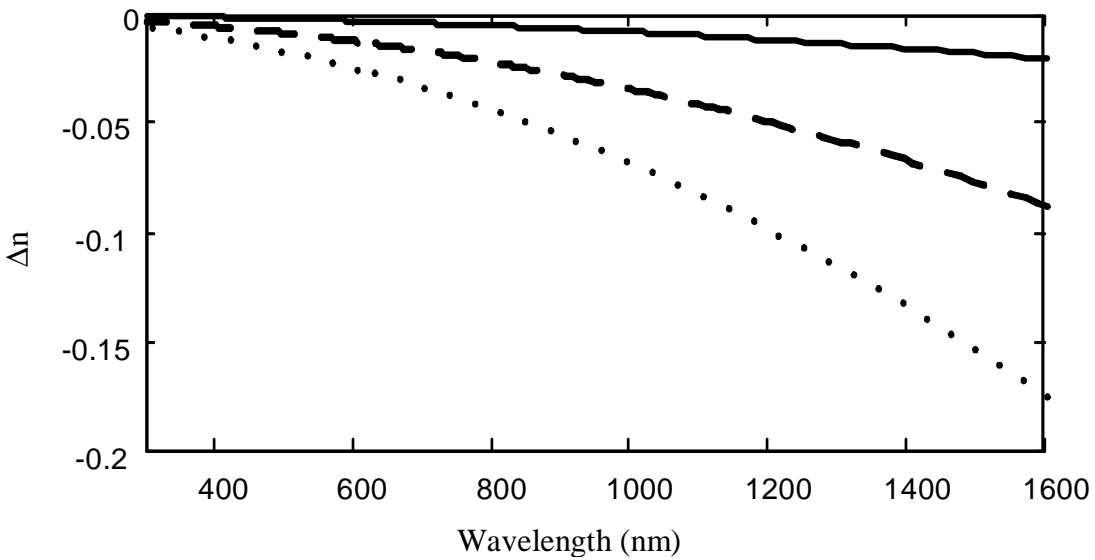


**Figure 4.10** Index change versus signal wavelength due to the plasma effect of GaN. Solid line:  $N = 7 \times 10^{18} \text{ cm}^{-3}$ , dashed line:  $N = 3 \times 10^{19} \text{ cm}^{-3}$ , dotted line:  $N = 6 \times 10^{19} \text{ cm}^{-3}$ . (Ref. [34])

#### 4.2.4 Combination of Effects

The three carrier effects mentioned above were assumed to be independent. A simple sum of the effects can be used to estimate the total change in the refractive index. Figure 4.11 shows an example of the combination of changes in the refractive index from bandfilling, band-gap shrinkage, and free-carrier absorption for injection into GaN when  $N = P = 3 \times 10^{19} / \text{cm}^3$ .

Based on the results we obtained in previous subsections, we can see that for bandfilling and bandgap shrinkage, carrier-induced index changes are large around the material bandgap, and both values are reduced significantly with the wavelength

increase. In the infrared wavelength region in which we are interested, free-carrier absorption is the dominant effect for carrier-induced refractive index change.

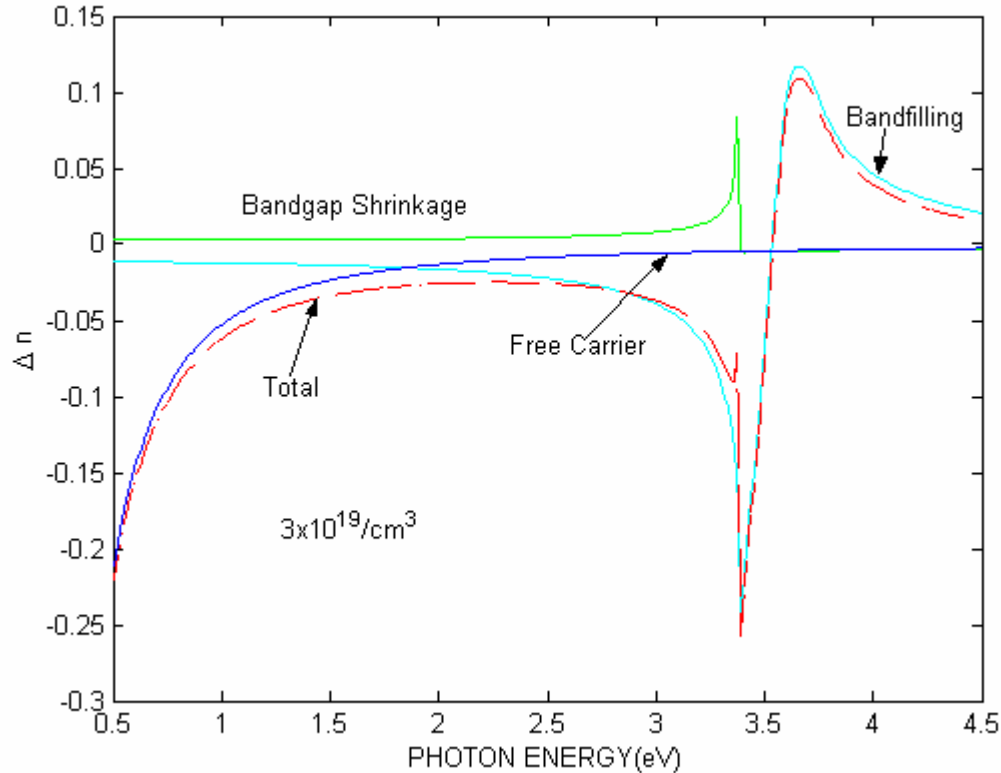


**Figure 4.11** Predicted changes in refractive index of GaN from the combination of the three effects (the dashed line).  $N = P = 3 \times 10^{19}/\text{cm}^3$ .

In previously published results for InP material [35], for carrier concentrations less than about  $10^{17}\text{cm}^{-3}$ , bandfilling dominates, yielding a negative  $\Delta n$ . Bandgap shrinkage effect is important over the range of  $10^{17} \leq \chi \leq 5 \times 10^{17} \text{ cm}^{-3}$ , approximately canceling the bandfilling and the plasma terms at wavelength  $1.3 \mu\text{m}$ . For higher

carrier concentrations, bandfilling and plasma effects dominate, yielding a large negative  $\Delta n$ . Comparing these results with our results, we noticed that the difference is because InP has a lower band-gap energy (1.34 eV), which makes bandfilling a dominant effect and bandgap shrinkage a big effect at some carrier concentrations. In our examples, GaN material has a larger band-gap energy (3.39 eV), which makes bandfilling and bandgap shrinkage mostly influential in short wavelength regions. For wavelengths in the infrared region, the photon energy is far below the bandgap energy. This makes bandfilling and bandgap shrinkage effects less influential in this region.

Our results reveal that the dominant effect is the free carrier absorption in this region.

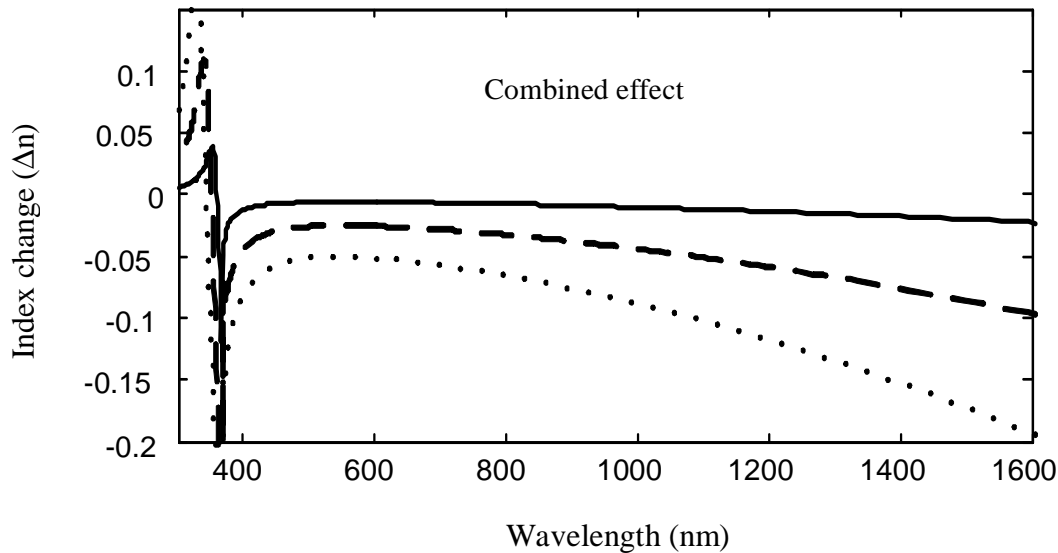


**Figure 4.12** Overall index change versus wavelength calculated at three carrier density levels:  $N = 7 \times 10^{18} \text{ cm}^{-3}$  (solid line),  $3 \times 10^{19} \text{ cm}^{-3}$  (dashed line) and  $6 \times 10^{19}$ , (dotted line).

Figure 4.12 shows the overall refractive index change versus wavelength combining all three effects. In order to investigate the feasibility of switchable optical PHASAR operating in the infrared using GaN semiconductor, we studied the carrier-induced refractive index change versus injected carrier density evaluated at wavelength 1550nm. The result is shown in figure 4.13, where a carrier density of  $2 \times 10^{18} \text{ cm}^{-3}$  causes approximately a 2% index change.

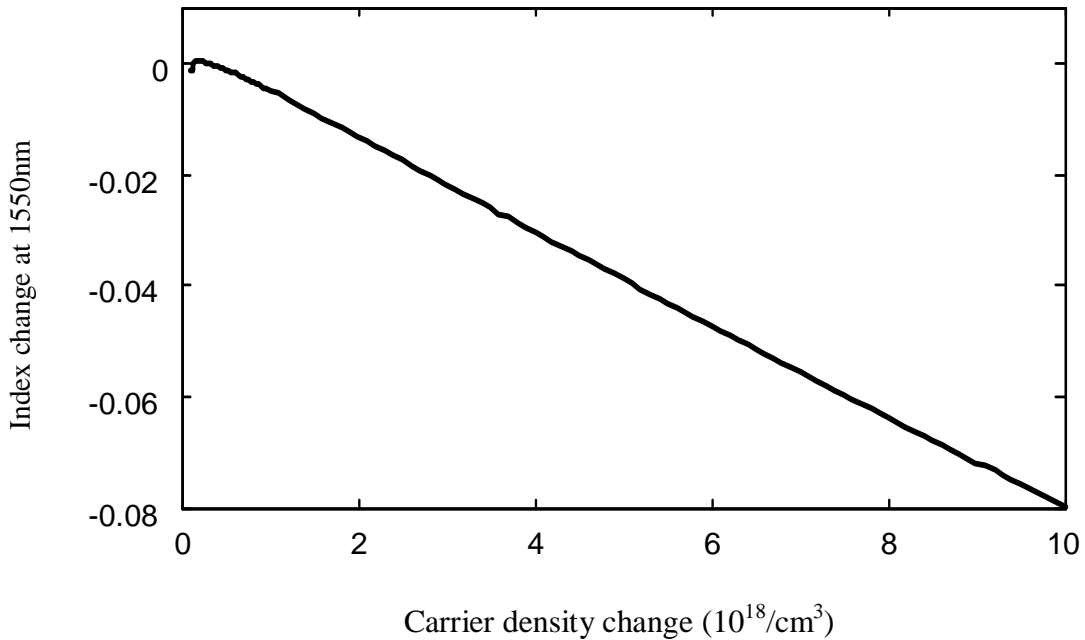


**Figure 4.13** Index change versus carrier density calculated at wavelength 1550nm.

For optical PHASAR applications, the index change of the waveguide should be large enough such that the optical length can be changed by half of the signal

wavelength. Consider a 1 mm electrode on the waveguide and the optical signal at 1550 nm wavelength. The minimum required index change should be approximately 0.0775%. According to Fig.4.13, this can be achieved by a carrier density change of  $1\times10^{18} \text{ cm}^{-3}$ , which is generally feasible.

In this chapter, we estimated theoretically the sensitivity of the carrier-induced index change in AlGaN semiconductor materials. We extended the investigation into the infrared wavelength region for application in optical communications. The numerical values obtained through this study provide us with an important guideline for optical device design. The comparative study of different contributing effects is important for future device designs and for optimizations in a variety of applications.

## **5. GaN Material Design and Experiments**

### **5.1 Introduction**

The configurations of basic optical devices have been discussed in Chapter 2 and the configurations of all-optical devices have been discussed in Chapter 3, where the details of optical materials used for constructing the devices were not considered. In Chapter 4, theoretical calculations and analysis were focused on exploring the physical characteristics of semiconductor materials. In this chapter, we will use the results shown in Chapter 4 and design functional photonic devices with GaN semiconductor materials, which belong to III-nitrides material group. III-nitrides have low attenuation in the near-infrared wavelength region due to their wide bandgaps, while as semiconductors their refractive indices can be modulated by carrier injection. III-nitrides are also well known for their ability to operate at high temperatures, high power levels and in harsh environments. These characteristics make III-nitrides the ideal candidates for tunable optical phased-array (PHASAR) devices in optical communications.

We will first summarize optical waveguide theory, in which the basic concept of a single mode waveguide and the condition required in realizing it will be presented. We will then discuss the rectangular dielectric waveguide theory in which two methods, the Marcatili's method and the effective index method, will be presented. The mode guidance conditions obtained from these two methods will be compared. The beam propagation method (BPM) will then be introduced. BPM is a

powerful numerical simulation tool to deal with mode calculations, field distributions and transmissions in waveguides with axial variations. Then a BPM software----BeamPROP with which we can design a specific single mode waveguide and other photonic devices will be introduced. Using this simulation tool, we have designed various optical devices including single mode optical waveguides, waveguide couplers and AWGs. The devices were fabricated by our collaborator at Kansas State University. We developed an experimental setup to systematically characterize these devices and compare the measured results with the theoretical predictions. Several important effects such as waveguide loss and birefringence are carefully studied and measured. In the last section of this chapter, we will briefly discuss the thermal stability of the refractive indices of GaN materials.

## 5.2 Optical Waveguide Theory

Optical waveguide is the basis for optical devices. Rectangular dielectric optical waveguide with layered structure is one of the most popular waveguide categories, which is utilized to construct complicated photonic devices in planar lightwave circuits. It is necessary to briefly review optical waveguide theory before we start to introduce device design. In this section, we will discuss general theory of optical waveguide, especially the rectangular dielectric optical waveguide.

### 5.2.1 Symmetric Dielectric Slab Waveguides

The dielectric slab waveguide theory is very important since it provides the basis for dielectric waveguide design and also guidelines for more complicated waveguide structure analysis [50]. Figure 5.1 shows a slab waveguide in which the wave propagates in the  $z$ -direction and the width of the waveguide  $w$  is much larger than the thickness  $d$ . The field dependence on  $y$  is negligible in this case. From the wave equation

$$(\nabla^2 + \omega^2 \mu \epsilon) E = 0 \quad (5.1)$$

we can find the solutions for the fields everywhere.

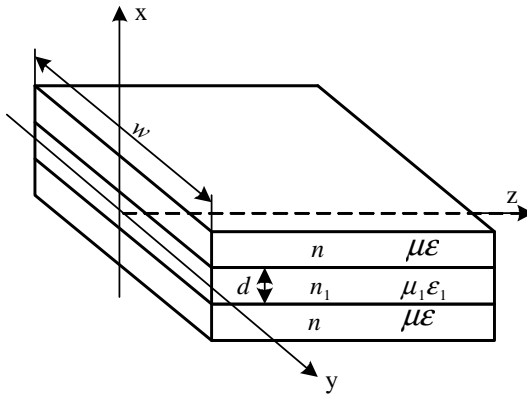


**Figure 5.1** A symmetric dielectric slab waveguide, where  $x$ - $y$  is the cross-section plane and  $z$  is the propagation direction.

We assume that the waveguide in figure 5.1 is symmetric. The permittivity and the permeability are  $\epsilon$  and  $\mu$ , respectively, for  $|x| \geq d/2$ , and  $\epsilon_1$  and  $\mu_1$  for  $|x| < d/2$ .

So we have even-mode and odd-mode solutions for this structure. For TE polarization, where  $\mathbf{E} = \hat{y}E_y$ , we can have the following equations by solving equation (5.1) [50]

$$k_x^2 + k_z^2 = \omega^2 \mu_1 \epsilon_1 \quad (\text{for } |x| < d/2) \quad (5.2)$$

$$-\alpha^2 + k_z^2 = \omega^2 \mu \epsilon \quad (\text{for } |x| \geq d/2) \quad (5.3)$$

$$\alpha \frac{d}{2} = \frac{\mu}{\mu_1} \left( k_x \frac{d}{2} \right) \tan \left( k_x \frac{d}{2} \right) \quad \text{TE even modes} \quad (5.4a)$$

$$\alpha \frac{d}{2} = -\frac{\mu}{\mu_1} \left( k_x \frac{d}{2} \right) \cot \left( k_x \frac{d}{2} \right) \quad \text{TE odd modes} \quad (5.4b)$$

where  $k_x$  and  $k_z$  are the  $x$ - and  $z$ - components of wave propagation constant  $\mathbf{k}$  respectively.  $k_z$  is the propagation constant of the guided mode in the  $z$ -direction. Due to the continuity requirement of  $k_z$  across the waveguide/cladding boundary at ( $x = \pm d/2$ ), equations (5.2) and (5.3) yield,

$$\left( \alpha \frac{d}{2} \right)^2 + \left( k_x \frac{d}{2} \right)^2 = \omega^2 (\mu_1 \epsilon_1 - \mu \epsilon) \left( \frac{d}{2} \right)^2 \quad (5.5)$$

$k_x$  and  $\alpha$ , can be found by combining equation (5.5) with either (5.4a) or (5.4b) and using graphical method on the  $(\alpha d/2) \text{ vs } (k_x d/2)$  plane. Figure 5.2 shows this graphical solution, where the radius  $R$  is obtained from equation (5.5)

$$R = \omega \sqrt{\mu_1 \epsilon_1 - \mu \epsilon} \left( \frac{d}{2} \right) = \left( k_0 \frac{d}{2} \right) \sqrt{n_1^2 - n^2} \quad (5.6)$$

where  $n_1 = \sqrt{\mu_1 \epsilon_1 / (\mu_0 \epsilon_0)}$  is the refractive index inside the guide,  $n = \sqrt{\mu \epsilon / (\mu_0 \epsilon_0)}$  is the refractive index in the cladding and  $k_0 = \omega \sqrt{\mu_0 \epsilon_0} = \omega / c$  is the free-space wave

number. After  $k_x$  and  $\alpha$  are graphically solved,  $k_z$  can be obtained either from equation (5.2) or from equation (5.3). The electric fields will have the following expressions

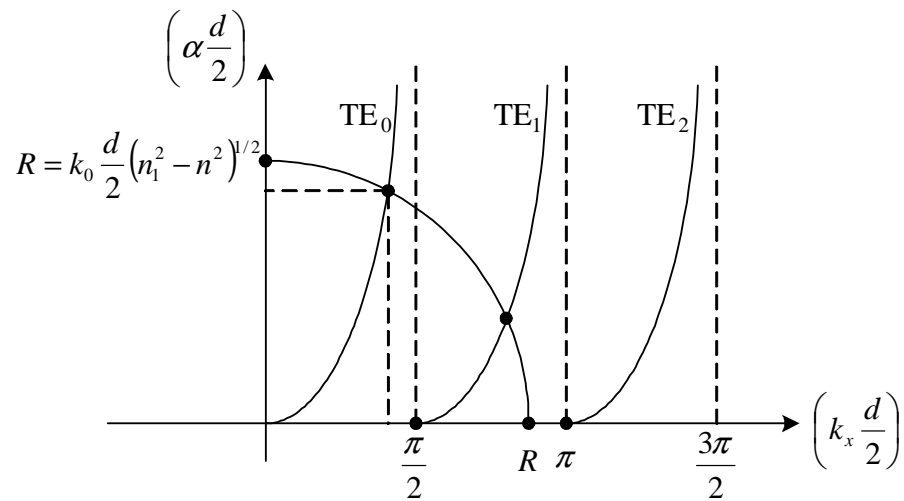


**Figure 5.2** A graphical solution for determining  $\alpha$  and  $k_x$  for the modes in symmetric dielectric slab waveguide. (after [50])

$$E_y = e^{ik_z z} \begin{cases} C_0 e^{-\alpha(x-d/2)} & x \geq \frac{d}{2} \\ C_1 \cos k_x x & |x| \leq \frac{d}{2} \\ C_0 e^{+\alpha(x+d/2)} & x \leq -\frac{d}{2} \end{cases} \quad (\text{For even modes}) \quad (5.7a)$$

Or

$$E_y = e^{ik_z z} \begin{cases} C_0 e^{-\alpha(x-d/2)} & x \geq \frac{d}{2} \\ C_1 \sin k_x x & |x| \leq \frac{d}{2} \\ -C_0 e^{+\alpha(x+d/2)} & x \leq -\frac{d}{2} \end{cases} \quad (\text{For odd modes}) \quad (5.7b)$$

where  $C_0$  and  $C_1$  are integration constants and can be determined with the boundary conditions of the electric fields.

From figure 5.2, we can see that the cutoff condition occurs at  $R = m\pi/2$  for the  $\text{TE}_m$  mode. So the  $\text{TE}_0$  mode has no cutoff frequency. When the following condition is satisfied

$$m \frac{\pi}{2} < R = k_0 \frac{d}{2} \sqrt{n_1^2 - n^2} < (m+1) \frac{\pi}{2} \quad (5.8)$$

There are  $(m + 1)$  guided TE modes in the dielectric slab.

From equation (5.8), we can see that  $(k_0 d / 2) \sqrt{n_1^2 - n^2} < \pi / 2$  is the condition for single mode operation. Under this condition, if the wavelength  $\lambda_0$  in free space and the waveguide dimension  $d$  are given, we can get the refractive index difference required for a single mode operation

$$\Delta n < \frac{1}{8n_1} \left( \frac{\lambda_0}{d} \right)^2 \quad (5.9)$$

Here we have also assumed that  $n_1$  is very close to  $n$  to get this equation. With equation (5.9), if, for example,  $\lambda_0 = d$  and  $n_1 = 3.6$ , we can get  $\Delta n < 0.035$  for single-mode operation in the waveguide.

From figure 5.2, we can also get the low-frequency limit and the high-frequency limit of  $k_z$ . At the low-frequency limit, [50]

$$k_z = \omega \sqrt{\mu \epsilon} = \frac{\omega n}{c} \quad (5.10)$$

At the high-frequency limit,

$$k_z = \omega \sqrt{\mu_1 \epsilon_1} = \frac{\omega n_1}{c} \quad (5.11)$$

The propagation constant  $k_z$  starts from  $\omega \sqrt{\mu \epsilon}$  at cutoff and increases to  $\omega \sqrt{\mu_1 \epsilon_1}$  as the frequency goes to infinity. The effective index for the guided mode is defined as

$$n_{\text{eff}} = \frac{k_z}{k_0} \quad (5.12)$$

For TM polarization, we may obtain the results by the duality principle: replacing the field solutions  $\mathbf{E}$  and  $\mathbf{H}$  of the TE modes by  $\mathbf{H}$  and  $-\mathbf{E}$ , respectively,  $\mu$  by  $\epsilon$  and  $\epsilon$  by  $\mu$ .

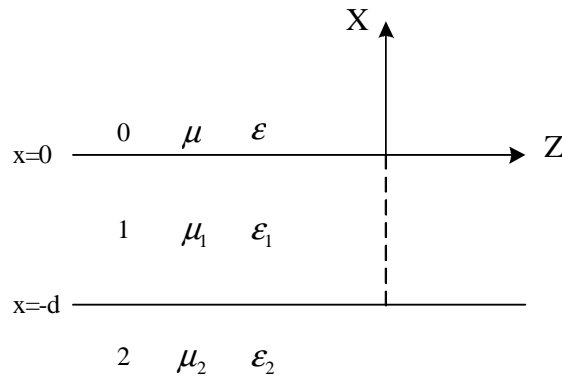


**Figure 5.3** An asymmetric dielectric slab waveguide. (after [50])

### 5.2.2 Asymmetric Dielectric Slab Waveguides

If the dielectric constant in the substrate  $\epsilon_2$  is different from that of  $\epsilon$  in the top medium or  $\mu_2 \neq \mu$ , the structure is asymmetric as is shown in figure 5.3.

In a similar method as in 5.2.1, we can get the electric field for TE polarization as

$$E_y = C_1 e^{ik_z z} \begin{cases} \cos \phi e^{-\alpha x} & x \geq 0 \\ \cos(k_x x + \phi) & -d \leq x \leq 0 \\ \cos(-k_x d + \phi) e^{+\alpha_2(x+d)} & x \leq -d \end{cases} \quad (5.13)$$

where  $C_1$  is a constant,  $\alpha$  and  $\alpha_2$  are two decay constants in region 0 and 2 in figure 5.3, respectively, and

$$-\alpha^2 + k_z^2 = \omega^2 \mu \epsilon \quad (x \geq 0) \quad (5.14a)$$

$$k_{1x}^2 + k_z^2 = \omega^2 \mu_1 \epsilon_1 \quad (-d \leq x \leq 0) \quad (5.14b)$$

$$-\alpha_2^2 + k_z^2 = \omega^2 \mu_2 \epsilon_2 \quad (x \leq -d) \quad (5.14c)$$

and

$$k_{1x} d = \tan^{-1} \frac{\mu_1 \alpha}{\mu k_{1x}} + \tan^{-1} \frac{\mu_1 \alpha_2}{\mu_2 k_{1x}} + m\pi \quad (m = 0, 1, 2, \dots) \quad (\text{TE}_m \text{ mode}) \quad (5.15)$$

For the wave to be guided in the core,  $\epsilon_1$  has to be larger than both  $\epsilon_2$  and  $\epsilon$ . When  $\epsilon_2 > \epsilon$  ( $\mu = \mu_1 = \mu_2$ ), the cutoff frequency is determined by

$$k_0 d \sqrt{n_1^2 - n_2^2} = \tan^{-1} \frac{\mu_1 \sqrt{n_2^2 - n^2}}{\mu \sqrt{n_1^2 - n_2^2}} + m\pi \quad (5.16)$$

where  $k_0 = \omega \sqrt{\mu_0 \epsilon_0} = \omega / c$ .

For TM polarization, we can again apply the duality principle. Similarly, we have the guidance condition as

$$k_{1x}d = \tan^{-1} \frac{\epsilon_1 \alpha}{\epsilon k_{1x}} + \tan^{-1} \frac{\epsilon_1 \alpha_2}{\epsilon_2 k_{1x}} + m\pi \quad (\text{TM}_m \text{ mode}) \quad (5.17)$$

### 5.2.3 Rectangular Dielectric Waveguides

#### 5.2.3.1 Marcatili's Method

By first introducing the mode theories, we are now prepared to discuss the rectangular dielectric waveguide theory. This theory is relevant because most waveguides have finite dimensions in both  $x$  and  $y$  directions.

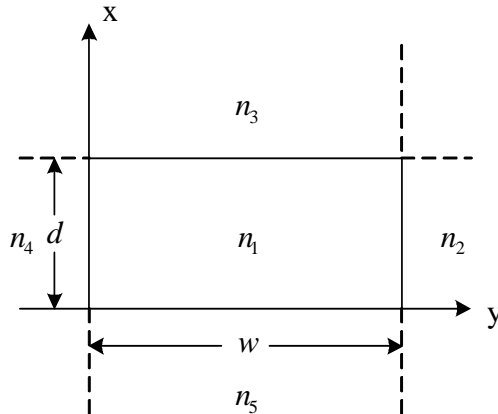


**Figure 5.4** A rectangular dielectric waveguide. (after [50])

Figure 5.4 shows a rectangular dielectric waveguide, where it is assumed  $w \geq d$ . Marcatili's method can be applied to this waveguide [51][52]. In order to obtain closed-form results, a few approximations have to be made. It was found that there are two possible mode classifications for this waveguide, which are

1.  $HE_{pq}$  modes:  $H_x$  and  $E_y$  are the dominant components.
2.  $EH_{pq}$  modes:  $E_x$  and  $H_y$  are the dominant components.

The Maxwell's equations in the following forms are used to initiate the analysis.

$$\begin{aligned} \mathbf{H} &= \frac{1}{i\omega\mu} \nabla \times \mathbf{E} \\ &= \frac{1}{i\omega\mu} \left[ \hat{x} \left( \frac{\partial}{\partial y} E_z - ik_z E_y \right) + \hat{y} \left( ik_z E_x - \frac{\partial}{\partial x} E_z \right) + \hat{z} \left( \frac{\partial}{\partial x} E_y - \frac{\partial}{\partial y} E_x \right) \right] \end{aligned} \quad (5.18)$$

$$\begin{aligned} \mathbf{E} &= \frac{1}{-i\omega\epsilon} \nabla \times \mathbf{H} \\ &= \frac{-1}{i\omega\epsilon} \left[ \hat{x} \left( \frac{\partial}{\partial y} H_z - ik_z H_y \right) + \hat{y} \left( ik_z H_x - \frac{\partial}{\partial x} H_z \right) + \hat{z} \left( \frac{\partial}{\partial x} H_y - \frac{\partial}{\partial y} H_x \right) \right] \end{aligned} \quad (5.19)$$

$$\frac{\partial}{\partial x} E_x + \frac{\partial}{\partial y} E_y + ik_z E_z = 0 \quad (5.20)$$

$$\frac{\partial}{\partial x} H_x + \frac{\partial}{\partial y} H_y + ik_z H_z = 0 \quad (5.21)$$

Here a constant permittivity in all regions is assumed. By using the above equations using the following approximate assumptions: 1) ignoring the boundary conditions for variables with small values, 2) for  $k_y \ll k_1, k_3$  and  $k_5$ , for  $HE_{pq}$  modes, the following two important guidance conditions can be found:

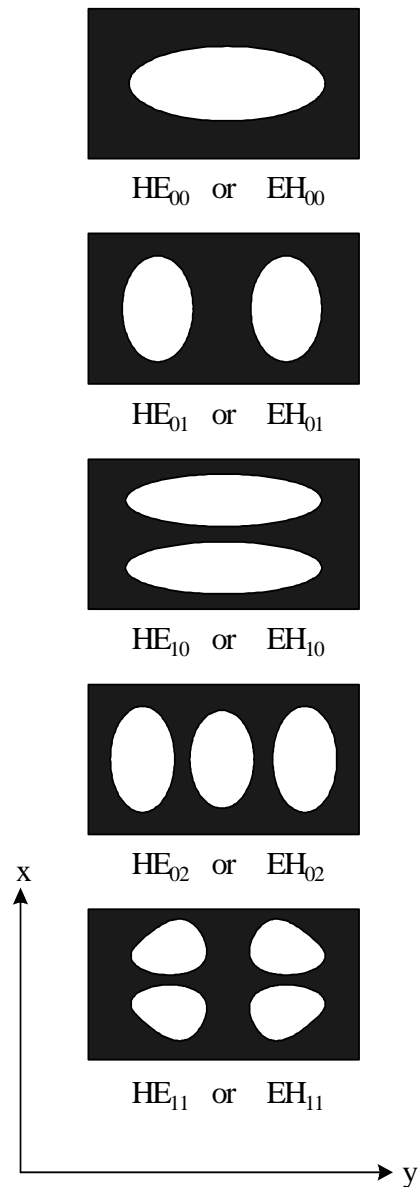


**Figure 5.5** Intensity patterns in a rectangular waveguide where  $w/d = 2$ , the refractive index of the waveguide  $n_1 = 1.5$ , and the background medium has  $n_0 = 1$ .  
(after [50])

$$k_x d = \tan^{-1} \frac{\mu_1 \alpha_3}{\epsilon_3 k_x} + \tan^{-1} \frac{\mu_1 \alpha_5}{\epsilon_5 k_x} + p\pi \quad (5.22)$$

$$k_y w = \tan^{-1} \frac{\epsilon_1 \alpha_2}{\epsilon_2 k_y} + \tan^{-1} \frac{\epsilon_1 \alpha_4}{\epsilon_4 k_y} + q\pi \quad (5.23)$$

Similarly, the following two important guidance conditions are found for  $EH_{pq}$  modes:

$$k_x d = \tan^{-1} \frac{\epsilon_1 \alpha_3}{\epsilon_3 k_x} + \tan^{-1} \frac{\epsilon_1 \alpha_5}{\epsilon_5 k_x} + p\pi \quad (5.24)$$

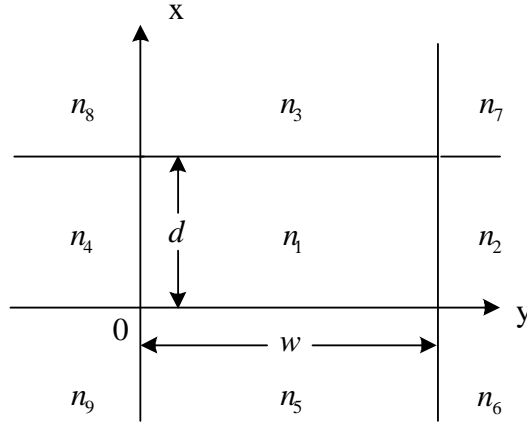
$$k_y w = \tan^{-1} \frac{\mu_1 \alpha_2}{\mu_2 k_y} + \tan^{-1} \frac{\mu_1 \alpha_4}{\mu_4 k_y} + q\pi \quad (5.25)$$

It should be noted that there were some approximations made to get the above equations [50]. The conditions include assuming  $H_x = 0$  and  $k_x \ll k_1, k_2$  and  $k_4$ . So Marcatili's method can be used to obtain the approximate field distribution and mode information. Figure 5.5 shows the intensity patterns in a rectangular waveguide where  $w/d = 2$ , the refractive index of the waveguide  $n_1 = 1.5$ , and the background medium has  $n_0 = 1$ . Only one set of intensity patterns is shown since the intensity pattern of the  $HE_{pq}$  mode is almost indistinguishable from that of the  $EH_{pq}$  mode.

### 5.2.3.2 The Effective Index Method

The Marcatili's method is essentially an approximation. In this subsection, we are going to introduce the effective index method, which is another technique to find the propagation constant of a dielectric waveguide. Now we illustrate this technique by applying it to the rectangular waveguide. The process of this method is clearly depicted in figure 5.6. Here only  $HE_{pq}$  modes are considered for the illustration.

(a) A rectangular dielectric waveguide



(b) Step one: solve for each  $y$  the effective index  $n_{\text{eff}}(y)$

i) $\frac{n_8}{n_4}$	ii) $\frac{n_3}{n_1}$	iii) $\frac{n_7}{n_2}$
$n_9$	$n_5$	$n_6$

(c) Step two: solve the slab waveguide problem using  $n_{\text{eff}}(y)$

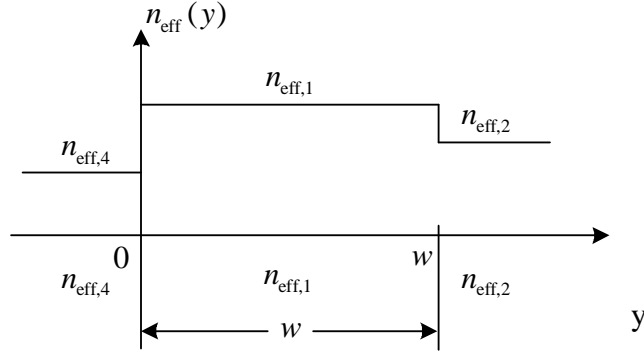


**Figure 5.6** (a) A rectangular dielectric waveguide to be solved using the effective index method. (b) Solve the slab waveguide at each fixed  $y$  and obtain an effective index profile  $n_{\text{eff}}(y)$ . (c) Solve the slab waveguide problem with the  $n_{\text{eff}}(y)$ .

(after [50])

**Step 1.** Take the second column in figure 5.6(b). It is a slab waveguide with refractive index  $n_1$  inside and  $n_3, n_5$  outside the waveguide. This is the case of asymmetric dielectric slab waveguide that we discussed in section 5.2.2. From equation (5.15), we can have the guidance condition for TE modes as

$$k_{1x}d = \tan^{-1} \frac{\mu_1\alpha_3}{\mu_3 k_{1x}} + \tan^{-1} \frac{\mu_1\alpha_5}{\mu_5 k_{1x}} + p\pi \quad (5.26)$$

From the solutions of the slab waveguide problem, we can get the propagation constant and therefore the effective index  $n_{\text{eff},1}$ .

For the first column ( $y > w$ ) and third column ( $y < 0$ ) in figure 5.6(b), we can get similar solutions as long as  $n_2 > n_6, n_7$ , and  $n_4 > n_8, n_9$ . Otherwise we can assume  $n_{\text{eff},1} \approx n_2$  and  $n_{\text{eff},4} \approx n_4$ .

**Step 2.** Solve the slab waveguide problem as shown in figure 5.6(c). Based on equation (5.17), we can get

$$k_{1y}d = \tan^{-1} \frac{\epsilon_{\text{eff},1}\alpha_2}{\epsilon_{\text{eff},2} k_{1y}} + \tan^{-1} \frac{\epsilon_{\text{eff},1}\alpha_4}{\epsilon_{\text{eff},4} k_{1y}} + q\pi \quad (5.27)$$

where  $\epsilon_{\text{eff},i} = n_{\text{eff},i}^2 \epsilon_0$ . Note this is the guidance condition for TM modes since the  $E_y$  component is perpendicular to the slab boundaries this time.

We can see that the field distribution obtained from step 1 is a function of  $x$  and  $y$ . So we can denote this as  $F(x, y)$ . The field distribution obtained from step 2 is only a function of  $y$ , which can be denoted as  $G(y)$ . Therefore, the total electric field  $E_y$  can be expressed as

$$E_y(x, y) = F(x, y)G(y) \quad (5.28)$$

Comparing equations (5.26) and (5.27) with equations (5.22) and (5.23), which were obtained with Marcatili's method, we can see that they are similar except that the effective permittivities are used in equation (5.27). Comparing with the results of numerical approach from the full-wave analysis, the results from both Marcatili's method and the effective index method agree very well. The effective index method usually has a better agreement with the numerical method, especially near cutoff [50].

### 5.3 Beam Propagation Method

The above theory only discussed the straight rectangular waveguide. However, the curvilinear directional couplers, branching and combining waveguides, S-shaped bent waveguides, and tapered waveguides are all indispensable components in constructing integrated optical circuits. So a more powerful method needs to be developed to deal with all these axial variations in waveguides. Beam propagation method (BPM) was developed for this purpose. BPM is such a powerful tool that it can be used to precisely evaluate the propagation characteristics of all those indispensable components mentioned above [53]. Not to mention that BPM can be used to design single mode waveguides, to calculate the effective refractive index in the waveguide and to illustrate the transmission along a straight waveguide. BPM is also applied to model channel-dropping filters [54], electro-optic modulators [55], multimode waveguide devices [56][57], optical delay line circuits [58][59], novel y-branches [60], optical interconnects [61], polarization splitters [62], and waveguide

polarizers [63], etc. BPM can be developed either based on the fast Fourier transform (FFT) or based on the finite difference method (FDM). Here we will briefly introduce the FDM analysis on optical waveguides.

### 5.3.1 Finite Difference Method Analysis of Planar Optical Waveguides

We start from the three-dimensional scalar wave equation, which is the basis of BPM [53]

$$\frac{\partial^2 E}{\partial x^2} + \frac{\partial^2 E}{\partial y^2} + \frac{\partial^2 E}{\partial z^2} + k^2 n^2(x, y, z) E = 0 \quad (5.29)$$

The electric field  $E(x, y, z)$  can be separated into two parts: the axially slowly varying envelope term of  $\phi(x, y, z)$  and the rapidly varying term of  $\exp(-jkn_0z)$ .

$$E(x, y, z) = \phi(x, y, z) \exp(-jkn_0z) \quad (5.30)$$

where  $n_0$  is the refractive index in the cladding. Substituting equation (5.30) into equation (5.29), we have

$$\nabla^2 \phi - j2kn_0 \frac{\partial \phi}{\partial z} + k^2(n^2 - n_0^2)\phi = 0 \quad (5.31)$$

For the lightwave propagation in slab waveguides, we can have the two-dimensional scalar wave equation from equation (5.31) [53]

$$\frac{\partial \phi}{\partial z} = -j \frac{1}{2kn_0} \frac{\partial^2 \phi}{\partial x^2} - \alpha(x, z)\phi - j \frac{k}{2n_0}[n^2(x, z) - n_0^2]\phi \quad (5.32)$$

Here,  $\partial^2 \phi / \partial z^2$  has been neglected by assuming  $|\partial^2 \phi / \partial z^2| \ll 2kn_0 |\partial \phi / \partial z|$ . This assumption is called the paraxial approximation or Fresnel approximation. Generally a differential equation of the form

$$\frac{\partial \phi}{\partial z} = A(x, z) \frac{\partial^2 \phi}{\partial x^2} + B(x, z) \phi \quad (5.33)$$

can be approximated by the finite difference method as

$$\frac{\partial \phi}{\partial z} \rightarrow \frac{\phi_i^{m+1} - \phi_i^m}{\Delta z} \quad (5.34)$$

$$A(x, z) \frac{\partial^2 \phi}{\partial x^2} \rightarrow \frac{1}{2} A_i^{m+1/2} \left\{ \frac{\phi_{i-1}^m - 2\phi_i^m + \phi_{i+1}^m}{(\Delta x)^2} + \frac{\phi_{i-1}^{m+1} - 2\phi_i^{m+1} + \phi_{i+1}^{m+1}}{(\Delta x)^2} \right\} \quad (5.35)$$

$$B(x, z) \phi \rightarrow \frac{1}{2} B_i^{m+1/2} (\phi_i^{m+1} + \phi_i^m) \quad (5.36)$$

where  $\Delta x$  and  $\Delta z$  are the calculation steps in  $x$ - and  $z$ -axis directions and subscripts  $i$  and  $m$  are sampling points along the  $x$ - and  $z$ -axis directions, respectively. The number of divisions along the  $x$ - and  $z$ -axis directions are  $N$  ( $i = 0-N$ ) and  $M$  ( $m = 0-M$ ), respectively. So  $\phi_i^m$  represents the electric field amplitude at  $x = x_i = i\Delta x$  and  $z = z_m = m\Delta z$ . Combining equations (5.32)-(5.36), we can have the following simultaneous equations:

$$-\phi_{i-1}^{m+1} + s_i^m \phi_i^{m+1} - \phi_{i+1}^{m+1} = \phi_{i-1}^m + q_i^m \phi_i^m + \phi_{i+1}^m \equiv d_i^m \quad (i = 1-n-1) \quad (5.37)$$

where

$$s_i^m = 2 - k^2 (\Delta x)^2 [(n_i^{m+1/2})^2 - n_0^2] + j \frac{4kn_0(\Delta x)^2}{\Delta z} + j2kn_0(\Delta x)^2 \alpha_i^{m+1/2} \quad (5.38)$$

$$q_i^m = -2 + k^2 (\Delta x)^2 [(n_i^{m+1/2})^2 - n_0^2] + j \frac{4kn_0(\Delta x)^2}{\Delta z} - j2kn_0(\Delta x)^2 \alpha_i^{m+1/2} \quad (5.39)$$

when the initial electric field distribution  $\phi_i^{m=0}$  ( $i = 0-N$ ) at the input position is given, the electric field profile  $\phi_i^m$  at  $z = z_m = m\Delta z$  ( $m = 1-M$ ) is successively

calculated by using equation (5.37). However, there are only ( $N - 1$ ) equations in equation (5.37) for ( $N + 1$ ) unknown variables. So the transparent boundary conditions at the input and output ends should be considered. Combing those boundary conditions into equation (5.37), we can get ( $N - 1$ ) simultaneous equations for ( $N - 1$ ) unknowns

$$-a_i\phi_{i-1}^{m+1} + b_i\phi_i^{m+1} - c_i\phi_{i+1}^{m+1} = d_i^m \quad (i = 1 - n - 1) \quad (5.40)$$

where

$$a_1 = 0, \quad b_1 = s_i^m - \exp(-j\kappa_{\text{left}}\Delta x), \quad c_1 = 1 \quad (5.41a)$$

$$a_i = 1, \quad b_i = s_i^m, \quad c_i = 1 \quad (i = 2 - N - 2) \quad (5.41b)$$

$$a_{N-1} = 1, \quad b_{N-1} = s_{N-1}^m - \exp(-j\kappa_{\text{right}}\Delta x), \quad c_{N-1} = 0 \quad (5.41c)$$

By solving equation (5.40), we can get the field distribution in the waveguide.

### 5.3.2 FDMBPM Analysis of Rectangular Waveguides

This is in three-dimensional case, so from equation (5.31), we can have

$$\frac{\partial \phi}{\partial z} = -j \frac{1}{2kn_0} \nabla^2 \phi - \alpha(x, y, z)\phi - j \frac{k}{2n_0} [n^2(x, y, z) - n_0^2]\phi \quad (5.42)$$

As in the previous section, the electric field at the grid point of  $x = i\Delta x$ ,  $y = l\Delta y$ , and  $z = m\Delta z$  is expressed by

$$\phi(i\Delta x, l\Delta y, m\Delta z) = \phi_{i,l}^m \quad (5.43)$$

By using the above notation, equation (5.42) can be approximated by the finite difference form as

$$\begin{aligned}
A(\phi_{i,l}^{m+1} - \phi_{i,l}^m) = & \frac{\phi_{i-1,l}^m - 2\phi_{i,l}^m + \phi_{i+1,l}^m + \phi_{i-1,l}^{m+1} - 2\phi_{i,l}^{m+1} + \phi_{i+1,l}^{m+1}}{2(\Delta x)^2} \\
& + \frac{\phi_{i,l-1}^m - 2\phi_{i,l}^m + \phi_{i,l+1}^m + \phi_{i,l-1}^{m+1} - 2\phi_{i,l}^{m+1} + \phi_{i,l+1}^{m+1}}{2(\Delta y)^2} \\
& + B(\phi_{i,l}^{m+1} + \phi_{i,l}^m)
\end{aligned} \tag{5.44}$$

where

$$A = \frac{j2kn_0}{\Delta z} \tag{5.45}$$

$$B = -jkn_0\alpha\left(i, l, m + \frac{1}{2}\right) + \frac{k^2}{2} \left[ n^2 \left(i, l, m + \frac{1}{2}\right) - n_0^2 \right] \tag{5.46}$$

Equation (5.44) can be solved by using alternating-direction implicit finite difference method (ADIFDM) [53]. The transparent boundary conditions are also applied.

It should be noted that the paraxial approximation (or the Fresnel approximation) has been adopted in the above FDMBPM analysis. Therefore this method is not very good for analyzing light beam propagation in a highly tilted waveguide from the initial propagation direction of the input signal. In that case, fast Fourier transform (FFT) BPM is applied since the paraxial approximation has not been used in this method. The details of FFTBPM can be found in [53].

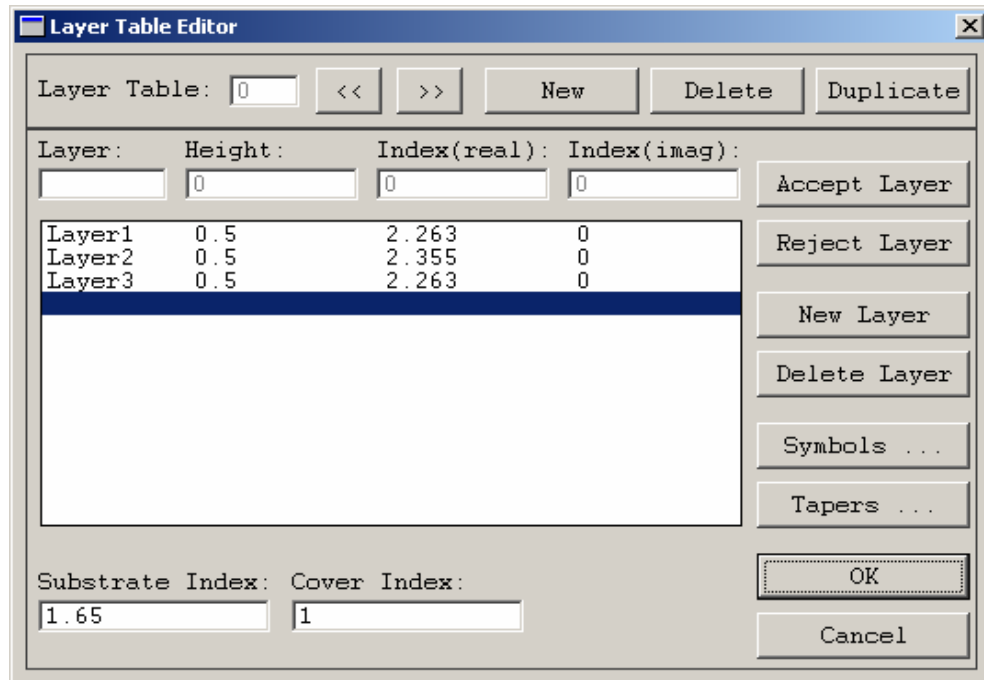
### 5.3.3 Straight Waveguide Design with BPM Software

#### 5.3.3.1 Mode Calculation with BPM Software

In the previous subsection, we introduced the basic principles of BPM. BPM is very powerful as we mentioned earlier. It can be used to do mode calculation and analyze the field distributions and transmissions in waveguides and devices. In this

subsection, we are going to briefly introduce a BPM software, *BeamPROP* with which we have designed single mode layer-structured waveguides and other optical devices. We have also run the simulations with *BeamPROP* to analyze the field distributions and the transmission along the waveguides and around the devices.

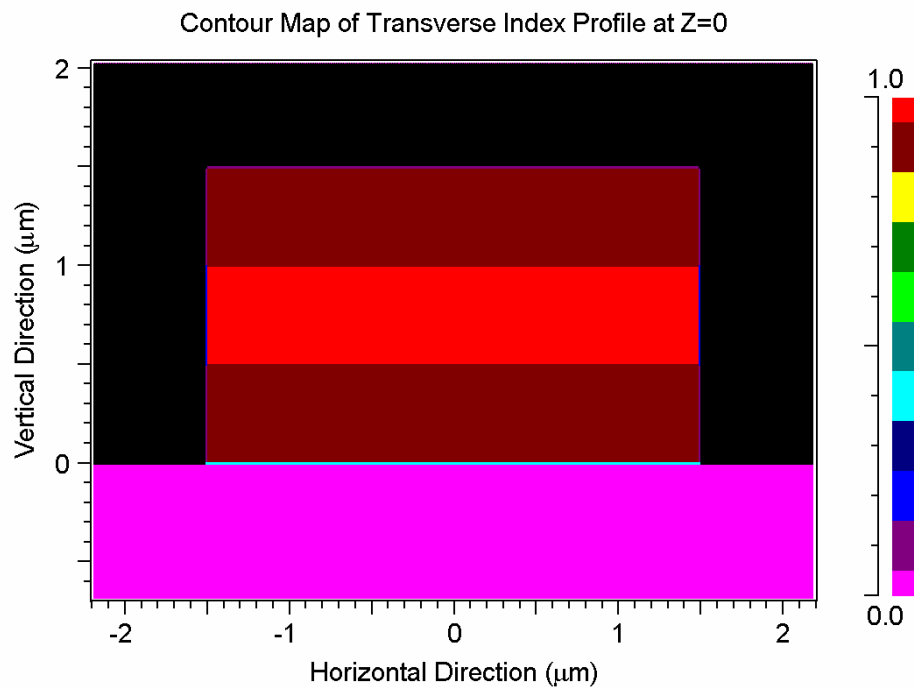
*BeamPROP* is a highly integrated CAD and simulation program for the design of photonic devices and photonic integrated circuits [64]. It incorporates advanced finite-difference beam propagation techniques for simulation, and a graphical user interface for circuit layout and analysis.



(a)

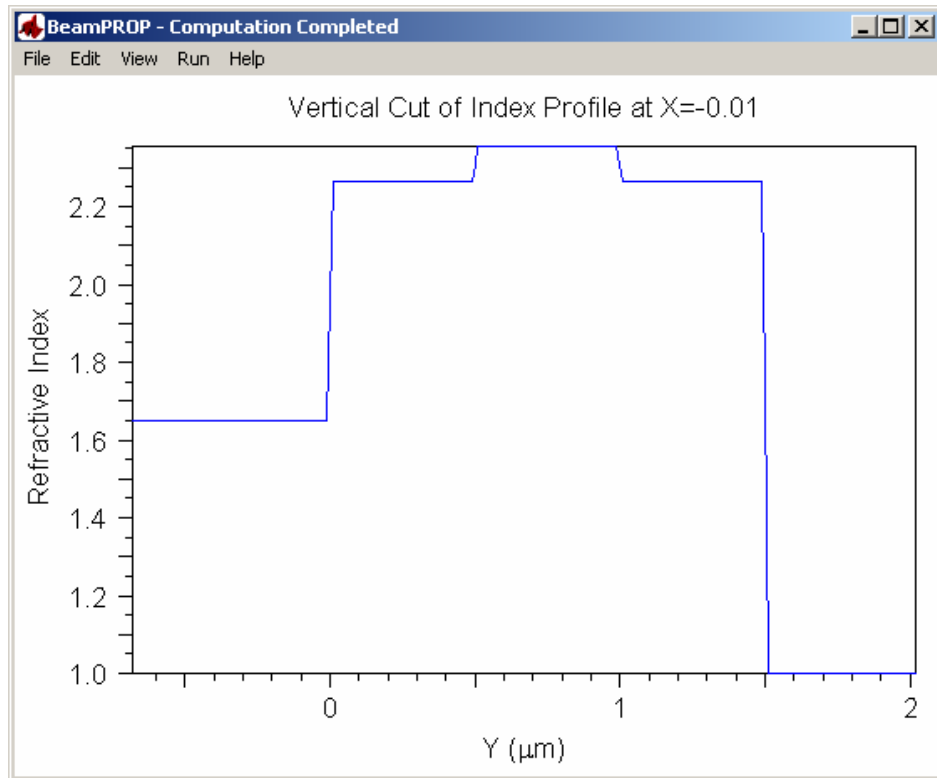
**Figure 5.7** The design of a layered rectangular waveguide with *BeamPROP*. (a) Refractive index distribution. (b) The illustration of the cross section of waveguide design. The refractive index is illustrated in different colors. (c) Vertical cut of index profile of the rectangular waveguide.

Figure 5.7 shows the design of a layer-structured rectangular waveguide with *BeamPROP*. Figure 5.7(a) shows a user-friendly window of layer table editor. From the table, we can see that the substrate of the waveguide has refractive index 1.65. This is a typical index value of Sapphire. The first, second and third layer has refractive index 2.263, 2.355, 2.263, respectively. These are the refractive indices of Erbium doped AlGaN materials with different Al concentration. The cover index is 1, which means the media covers the third (top) layer, the sides of the layered rectangular waveguide, and the Sapphire surface beyond the waveguide is air.



**Figure 5.7 (b)**

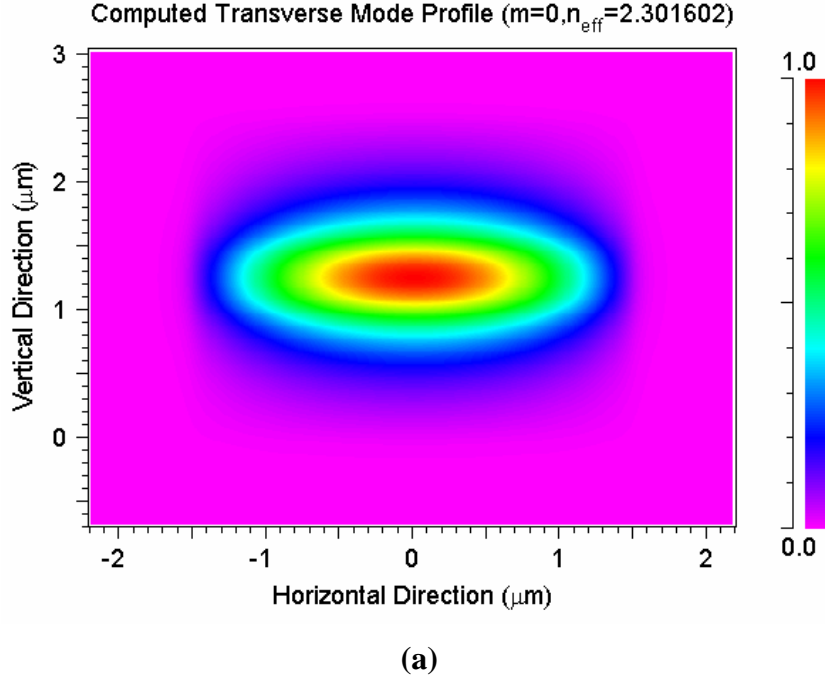
Figure 5.7(b) illustrates the cross section at the input side of the layer-structured rectangular waveguide. From the figure, it can be seen that the rectangular waveguide has a width of  $3 \mu\text{m}$  and a total height of  $1.5 \mu\text{m}$ , with  $0.5 \mu\text{m}$  high for each layer. The figure also illustrates the different refractive indices of different layers in different colors. This helps to verify the dimensions of the design.



**Figure 5.7 (c)**

Figure 5.7(c) shows another function of the *BeamPROP*. It shows the vertical cut of index profile at  $x = -0.01$ , where  $x$  is the value of the horizontal direction as in

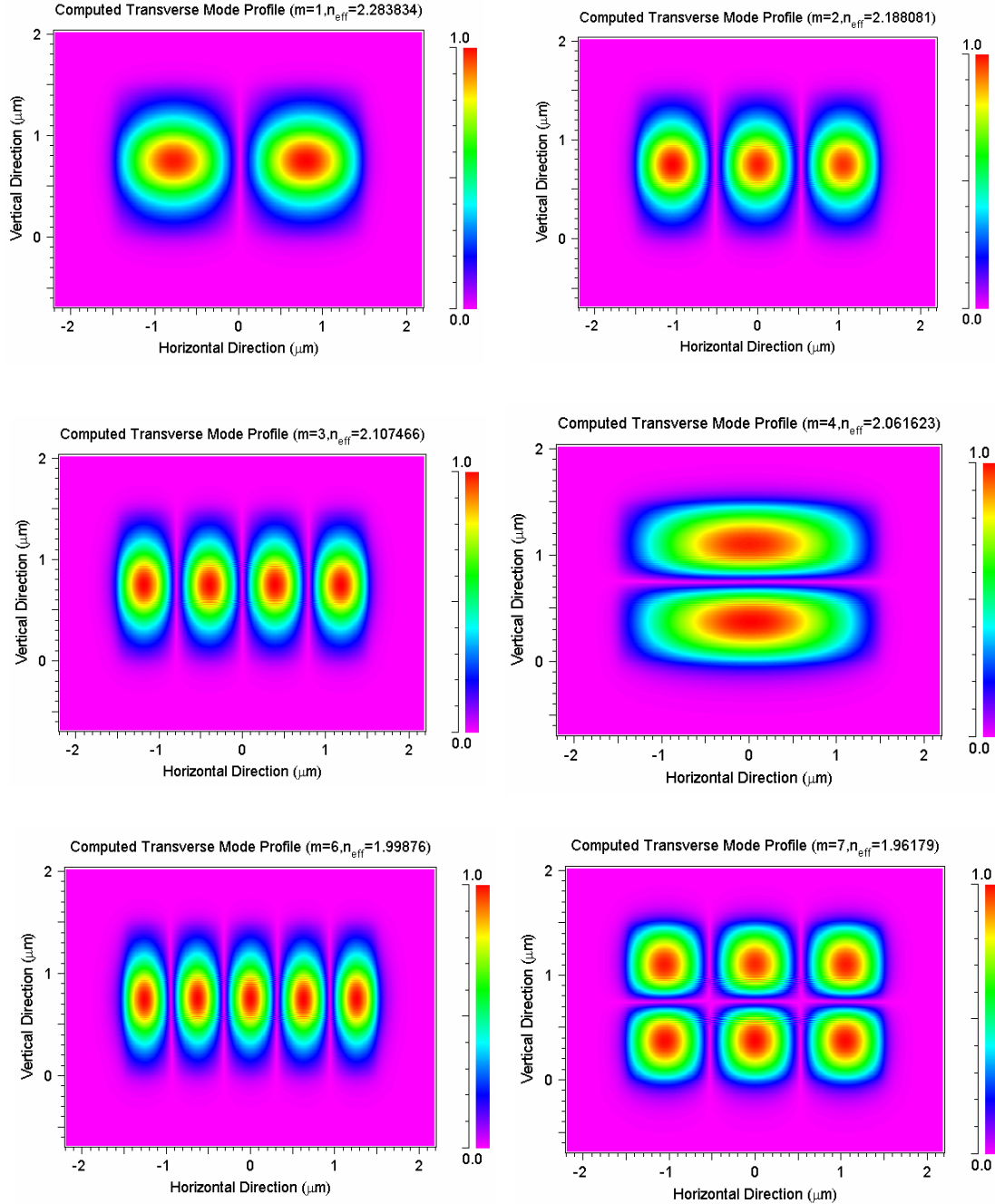
figure 5.7(b). The vertical cut can be made anywhere along the horizontal direction, so that we can have any vertical refractive index profile in which we are interested.



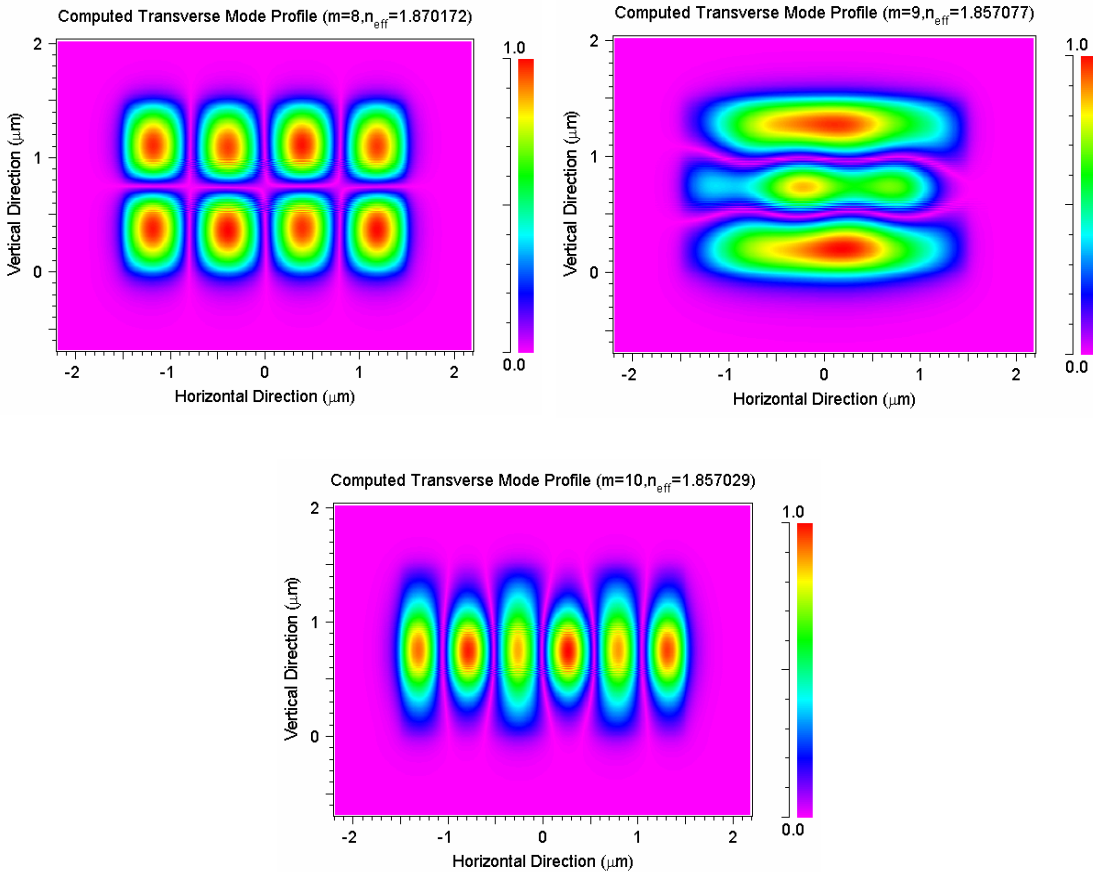
**Figure 5.8** The mode calculation of a layered rectangular waveguide with *BeamPROP*. (a) The basic mode. (b) The illustration of the cross section of waveguide design. The refractive index is illustrated in different colors. (c) Vertical cut of index profile of the rectangular waveguide.

We have set the length of the layer-structured straight rectangular waveguide as 1,000  $\mu\text{m}$  and run the simulation with *BeamPROP* to calculate the mode solution. In the simulation, we used wavelength 980 nm as signal wavelength. Figure 5.8 shows our simulation results. Figure 5.8(a) shows the fundamental mode of the waveguide. The power distribution in cross section of the waveguide is illustrated

with different colors. Also it can be seen that the effective refractive index is calculated for this mode propagation.



**Figure 5.8 (b)**



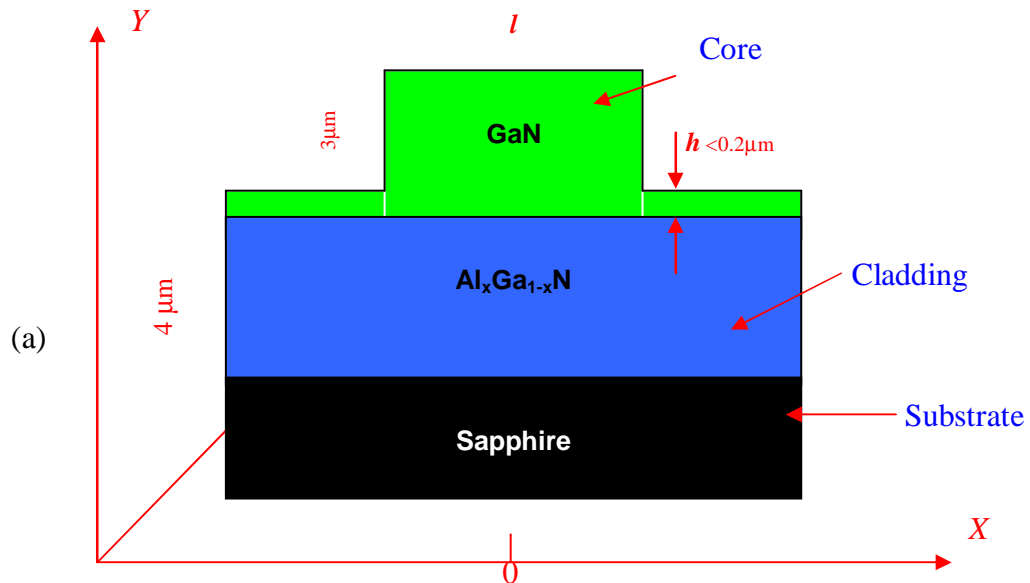
**Figure 5.8 (c)**

Figure 5.8(b) and (c) show the other calculated modes of the waveguide with *BeamPROP*. It can be seen that the waveguide has multi modes. Also we can see that the effective refractive index is calculated for each mode.

By simply adjusting the dimensions of the width and the height of the waveguide, we can have different results of mode calculation. By proper adjusting the dimensions of all the layers, we can obtain single mode waveguide for the wavelength we choose. We will show this in the next subsection.

### 5.3.3.2 Single-Mode Layered Rectangular Waveguide Design with *BeamPROP*

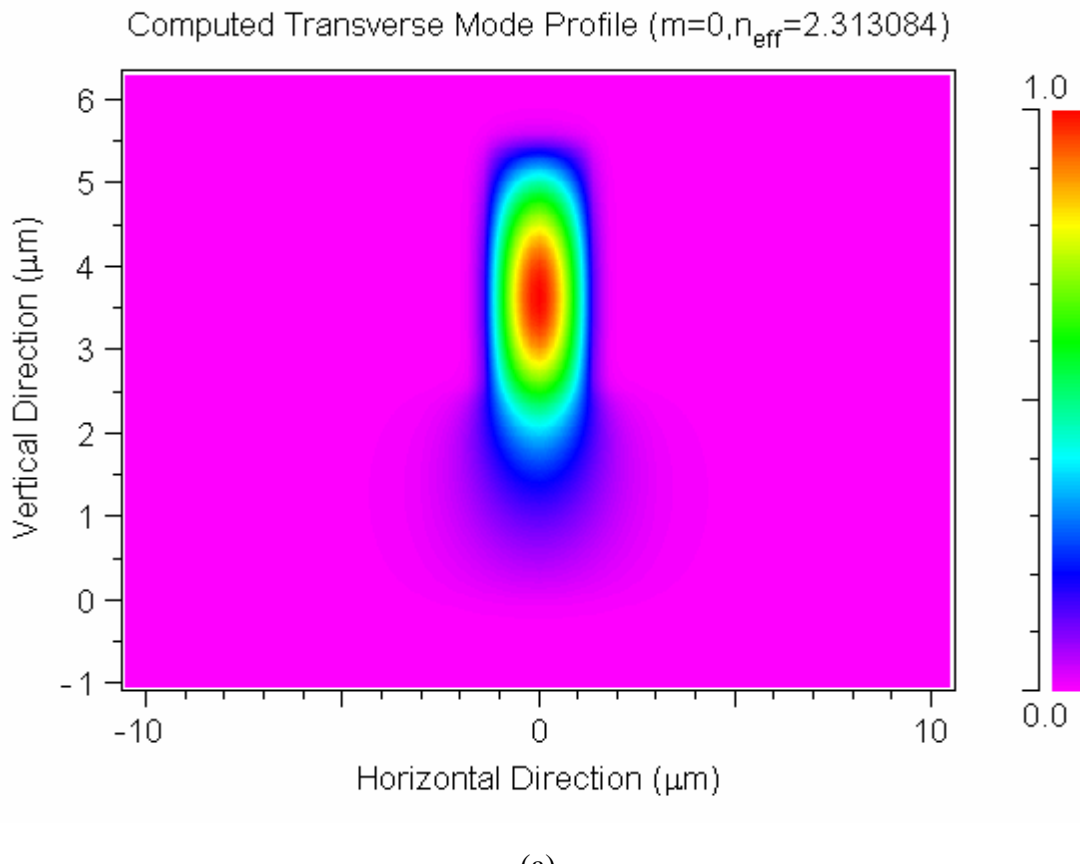
As we mentioned above, we can use *BeamPROP* to design single-mode layered rectangular waveguide. The previous work we did gives the values of refractive indices of GaN and its alloys  $\text{Al}_x\text{Ga}_{1-x}\text{N}$  with Al molar fraction  $x$  varying. These values will be given out later in this chapter (figure 5.12(a)). Based on these results, we designed layered single-mode optical waveguide and the related optical devices with *BeamPROP*.



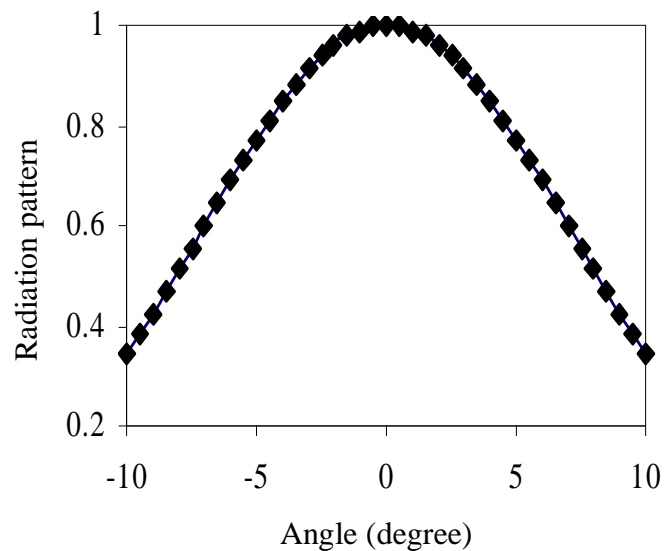
**Figure 5.9** The cross section of the design of GaN single-mode waveguide.

Figure 5.9 shows schematically the cross section of the designed straight single-mode waveguide using GaN as the core,  $\text{Al}_x\text{Ga}_{1-x}\text{N}$  as the cladding and Sapphire as the substrate. In our simulation, the value of the core refractive index was

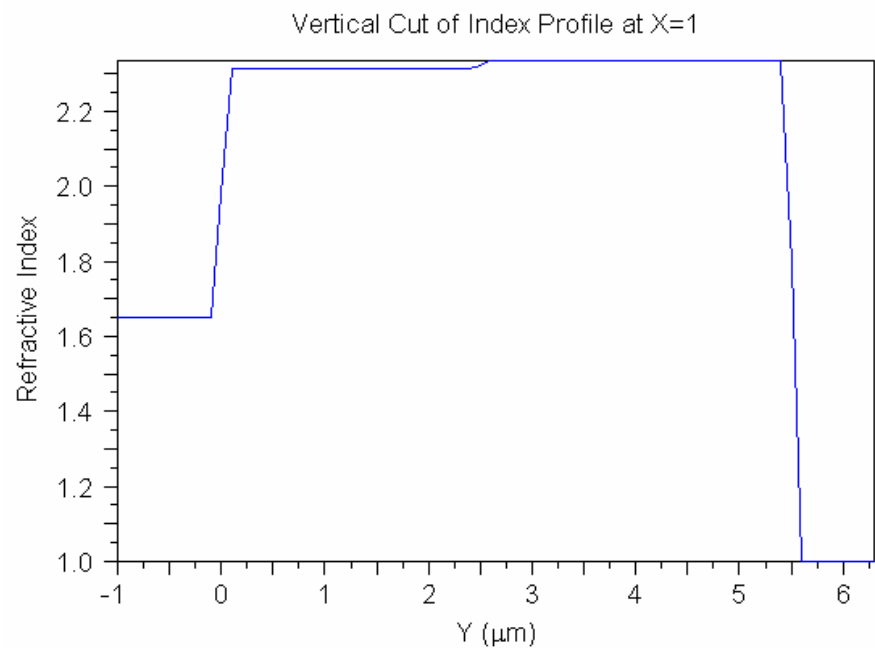
set as 2.335. This is the refractive index of GaN we previously obtained, which will also be shown later in this chapter. Then we varied the value of the cladding refractive index and the value of the waveguide width  $l$  as shown in figure 5.9. We found that when the cladding refractive index is 2.312, which corresponds to the Al molar fraction  $x \sim 3\%$  [29], the value of  $l$  has to be between  $3 \mu\text{m}$  and  $5 \mu\text{m}$  for the waveguide to support a single-mode. From figure 5.9, we can see that there is a thin slab above the  $4 \mu\text{m}$  cladding. In the simulation, it was found that the height  $h$  of this slab has to be less than  $0.2 \mu\text{m}$  to keep the waveguide as single-mode. In our design, we have taken  $h$  equal to 0 for convenience. However, the condition  $h < 0.2 \mu\text{m}$  is meaningful since it is difficult to get exactly  $h = 0$  in the real waveguide fabrication process. We then measured the effective refractive index through the simulation and the result we got was around 2.313 as shown in figure 5.10(a). Figure 5.10(a) also clearly shows the verification of the single-mode transmission on our designed waveguide. Figure 5.10(b) shows radiation pattern versus exit angle of the waveguide. Figure 5.10(c) shows the refractive index characteristics in the cross section along  $Y$  direction at  $X = 0$ . It was in accordance with our designed values. All the single waveguides except for the tapered connections in the devices we designed have the cross section as shown in figure 5.9.



**Figure 5.10** Simulation result of the designed GaN single-mode waveguide with *BeamPROP*. (a) Single mode simulation verification and the effective refractive index; (b) Radiation pattern versus exit angle; (c) Refractive index characteristics along  $Y$  direction, at  $X = 0$ .



(b)



(c)

**Figure 5.10** (b) and (c)

### **5.3.3.3 Optical waveguide preparation and characterization**

Based on the BPM simulation result, several different waveguide configurations have been designed. These designs include straight waveguides,  $2 \times 2$  waveguide couplers and AWGs, which will be discussed later. To verify the design, various sample devices were fabricated with the help of the Physics Department at Kansas State University. In the fabrication process, the optical waveguide structures were formed by photolithographic patterning and inductively-coupled plasma (ICP) dry etching [65]. According to the design, the etching depth is controlled at approximately  $2.8 \mu\text{m}$  and the *Al* molar fraction  $x$  is about 3%. The sample devices will be presented and discussed later.

## **5.4 Measurement Method and Experimental Setup**

Based on the configurations of the single-mode waveguide we obtained through our simulation as shown in the above section, we fabricated waveguides and some simple devices. Before we introduce them here, we would like to show the measurement method and illustrate the experimental setup first.

### **5.4.1 Measurement Method Based On Febry-Perot (FP) Interference**

In the application of all-optical communications, it is important to measure the effective refractive index of a waveguide precisely. It is also important to measure the waveguide's single-pass power attenuation, excluding the uncertainties caused by optical coupling at both the input and output of the waveguide. To do the required

measures, Febry-Perot (FP) interference method was applied in our measurement, where the two end facets of the straight waveguide forms the F-P cavity. In the measurement, an erbium-doped fiber amplifier (EDFA) without optical signal input was used to provide a wide-band amplified spontaneous emission (ASE). The ASE optical spectrum at the output of the optical waveguide was recorded with an optical spectrum analyzer (OSA).

From the OSA, we can get the measured optical transmission spectrum. Then apply this measured transmission spectrum to fit the normalized FP transmission equation [66]

$$T(\lambda) = [1 + R^2 A^2 - 2RA \cos(4\pi L n_{eff} / \lambda + \phi_0)]^{-1} \quad (5.47)$$

where  $L$  is the waveguide length,  $R$  is the power reflectivity of the waveguide end facet,  $\phi_0$  is an initial phase or a fitting constant,  $n_{eff}$  can be obtained through the simulation,  $A$  is the single-pass power attenuation. With the best fitting, value  $A$  can be obtained. Thus the waveguide loss per unit length can be obtained.

As for the application of this method to get the effective refractive index,  $n_{eff}$ , it is also shown in equation (5.47). From the equation,  $n_{eff}$  can be easily obtained as long as all the other parameters were measured or calculated. Optical signals with different polarizations can be applied and the different effective refractive indices related to different polarizations may be obtained.

### 5.4.2 Experimental Setup

To characterize the waveguide samples we have designed and fabricated, a fiber-optic setup operating in the 1550 nm wavelength region was constructed. Optical coupling at the input and the output of the waveguide was accomplished by using tapered single-mode fibers with 6- $\mu\text{m}$ -working distance and 2.5- $\mu\text{m}$ -spot size of the focus. Each tapered fiber end was mounted on a five-dimensional precision positioning stage to optimize the optical coupling efficiency. A tunable laser diode was used as the light source and an optical power meter was used to measure the optical power that passes through the waveguide. Figure 5.11 shows this experimental setup.

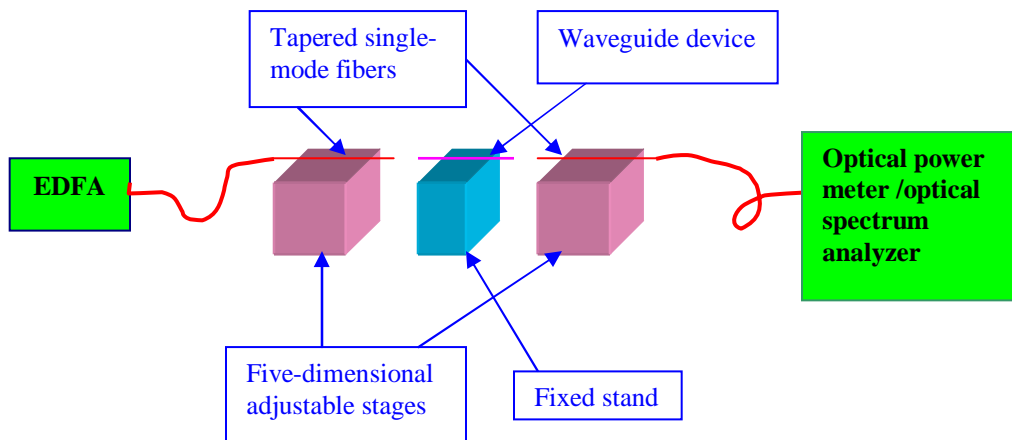


**Figure 5.11** Fiber-optical experimental setup.

## 5.5 Measurement of Refractive Indices in Infrared

From section 5.3.3, we could see that, in order to design guided-wave optical devices, the knowledge of material refractive indices in the operating wavelength region is essential. We have conducted the refractive index measurements for  $Al_xGa_{1-x}N$  with different  $Al$  molar fractions. In order to perform this measurement, a number of sample  $Al_xGa_{1-x}N$  films were grown by metal organic chemical vapor deposition (MOCVD) on sapphire substrates. The films' thickness range from 1.1  $\mu\text{m}$  to 1.5  $\mu\text{m}$  and  $Al$  molar fractions range from  $x = 0.1$  to  $x = 0.7$  [67]. To evaluate the refractive index of each film, optical transmission spectra were measured. Due to the Fabry-Perot (FP) interference caused by the two facets of the film (one facet is between  $Al_xGa_{1-x}N$  and the air and the other facet is formed between  $Al_xGa_{1-x}N$  and sapphire), optical transmission efficiency is wavelength-dependent. With the knowledge of the film thickness, the film refractive index can be obtained by best fitting the measured optical transmission spectrum to a well-known FP transmission equation.

Figure 5.12(a) shows the measured refractive indices of  $Al_xGa_{1-x}N$  versus wavelength for several different  $Al$  molar fractions. The continuous curves in the same figure were numerical fittings obtained by using the first order Sellmeir dispersion formula:

$$n(\lambda) = \sqrt{1 + \frac{(B_0 + B_1x + B_2x^2)\lambda^2}{\lambda^2 - (C_0 + C_1x)^2}} \quad (5.48)$$

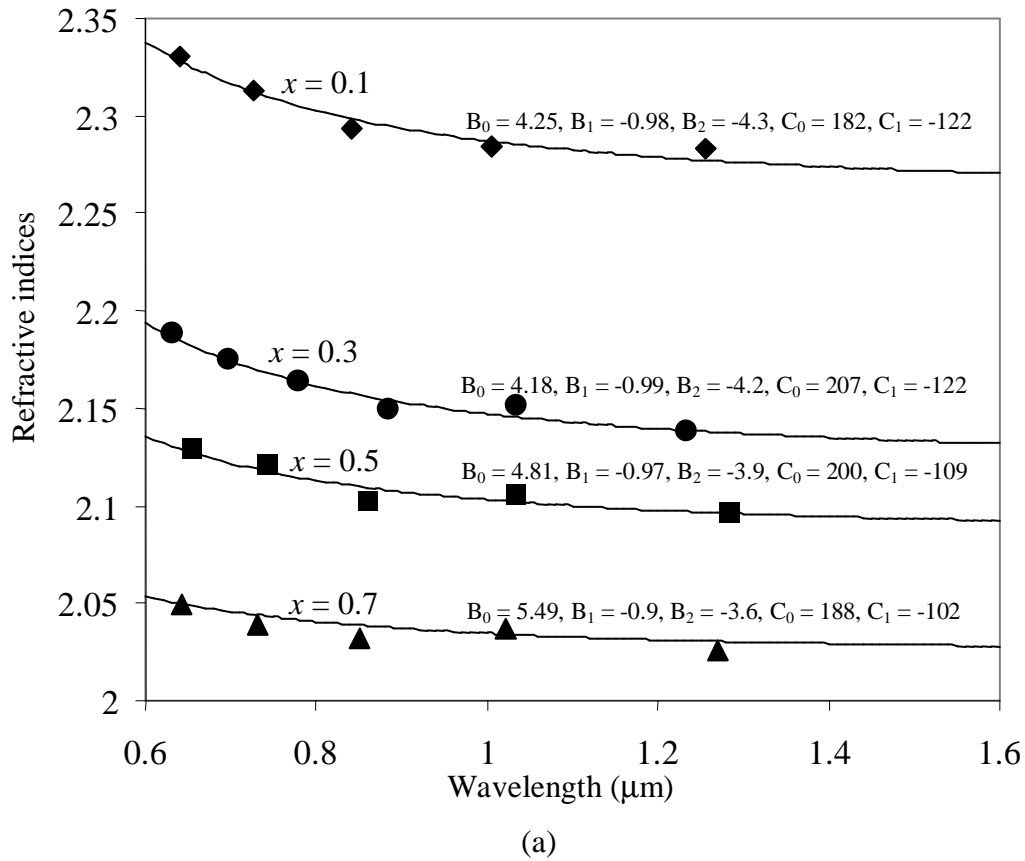


**Figure 5.12** (a) Refractive indices of  $\text{Al}_x\text{Ga}_{1-x}\text{N}$  versus wavelength for several different Al molar fractions. (b) Sellmeier expansion coefficients versus Al molar

The coefficients for best fit are displayed in Figure 5.12(a) and their variations versus *Al* molar fraction  $x$  are shown in Figure 5.12(b). Since we are mostly interested in the refractive indices in 1550 nm wavelength window, this information can be collected from Figure 5.12 and the following polynomial expression is obtained for the *Al* molar fraction ( $x$ ) dependence of the refractive index at 1550nm wavelength,

$$n(1550\text{nm}) = 0.431x^2 - 0.735x + 2.335. \quad (5.49)$$

The monotonic decrease of  $Al_xGa_{1-x}N$  refractive index with the increase of  $Al$  molar fraction  $x$  makes the design of single-mode optical waveguide devices straightforward.

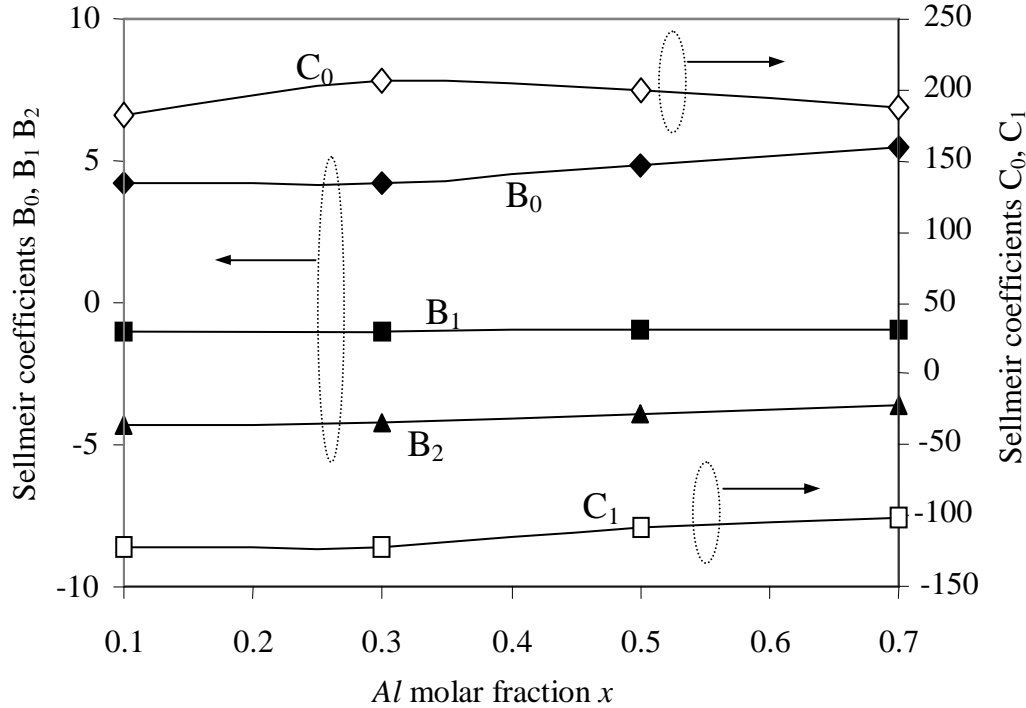


**Figure 5.12 (b)**

## 5.6 Measurement Results of the Single-Mode GaN/AlGaN Waveguides

### 5.6.1 Experimental Results: Power Loss in Waveguide Transmission

Based on the method in section 5.4.1 and the experimental setup in section 5.4.2, we then did an experiment to measure the effective refractive index and the single-pass power loss of our fabricated waveguide. The measured result is shown in figure 5.13 where the normalized output optical spectrum we got from the OSA is

illustrated. In the figure, the solid points formed measured optical transmission spectrum. The continuous line was obtained by fitting the normalized FP transmission equation (5.47). By the best fitting, we got the single-pass power attenuation value  $A = 4.8$  dB, corresponding to a waveguide length 1.393 mm. The waveguide loss per unit length is  $\sim 34.4$  dB/cm. It should be pointed out that the actual attenuation of the waveguide should be less than this value, since the cleaved waveguide end facets may not be ideally flat and they are definitely not exactly perpendicular to the waveguide axis to form an ideal F-P cavity.

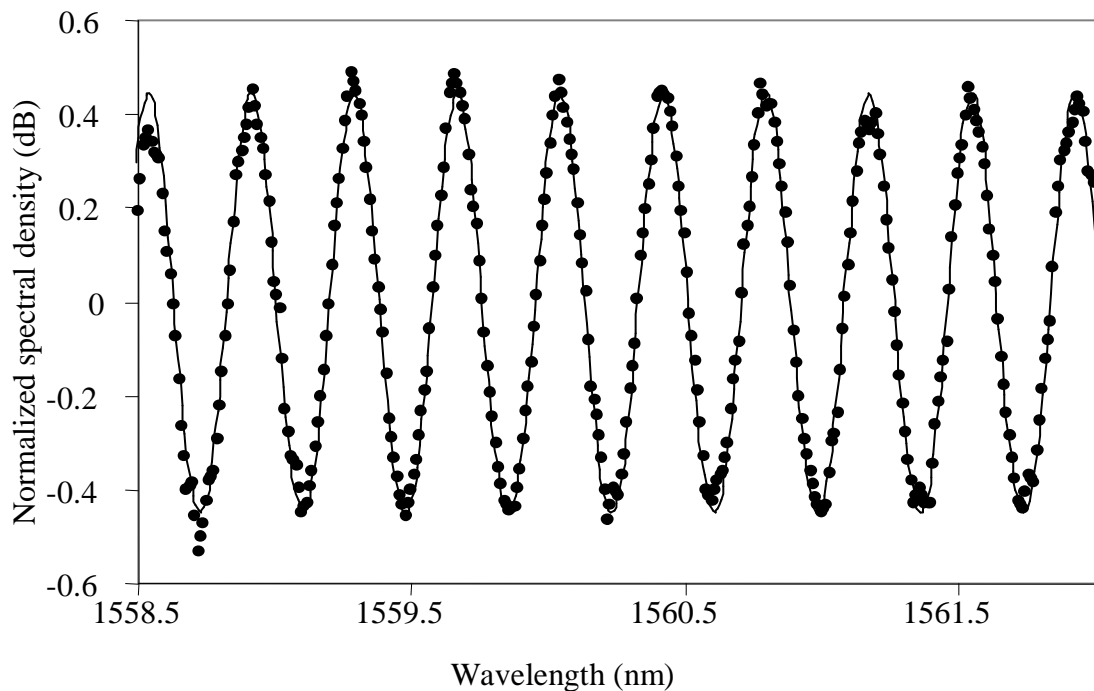


**Figure 5.13** Measured optical transmission spectrum (solid point) and numerical fitting using equation (2-13) (continuous line). (Ref.[29])

### **5.6.2 Birefringence of GaN/AlGaN optical waveguides**

In planar lightwave circuit applications, an important parameter is the refractive index of the material, which we have discussed in the above subsection. Besides this, the knowledge of the birefringence of the material is also critical in waveguide design and in device performances. So we studied the birefringence characteristic of the GaN/AlGaN optical waveguides. The birefringence of GaN films grown on sapphire substrates has been reported [68]. A refractive index change of approximately 4% was observed at wavelength around 800 nm when the signal polarization was varied from perpendicular to parallel to the GaN crystal c-axis [69]. On the other hand, due to the wurtzite structure, the crystal lattice of GaN has a hexagonal configuration on the *a-b* plane. It has been reported that the efficiency of the optical emission changes periodically when the optical propagation direction changes on the *a-b* plane [70]. Figure 5.14 shows the wurtzite structure of GaN unit cell and the coordinate choices. It can be seen that the structure has a hexagonal configuration in *a-b* plane. We believe that the birefringence is not only due to the polarization direction of the optical signal, but also due to the incident direction of the input light beam relative to the direction of axis *a* as shown in figure 5.14.

In order to investigate the birefringence caused by both signal polarization and different incident direction relative to *a*-axis direction, different single-mode waveguides were made by changing the angle between the directions of straight waveguide and the crystal *a*-axis. Figure 5.15 shows this design, where angle  $\theta$  varied for different waveguide samples. In the figure, axis *a*, *b* and *c* are the same as in

Figure 5.14 while  $G$  is the direction of the waveguide. The lengths of the waveguide samples ranged from 1.5 – 3.0 mm.

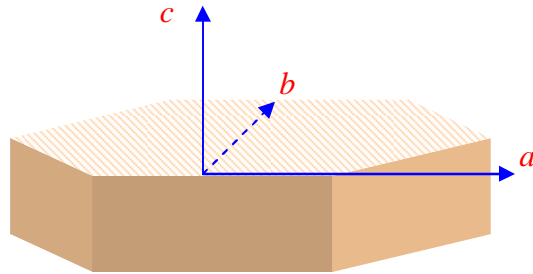


**Figure 5.14** The wurtzite structure of GaN unit cell and the choice of coordinates.

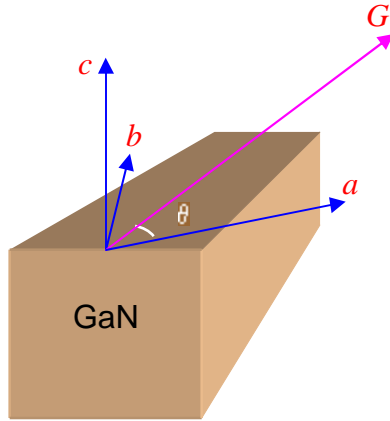


**Figure 5.15** Waveguide sample. Waveguide differs by the angle  $\theta$

Again the measurement method based on the FP interference was applied. The difference in the experimental setup was the use of a fiber-optical polarizer and a

polarization controller, which are inserted immediately after the ASE source. The experimental setup is shown in figure 5.16.

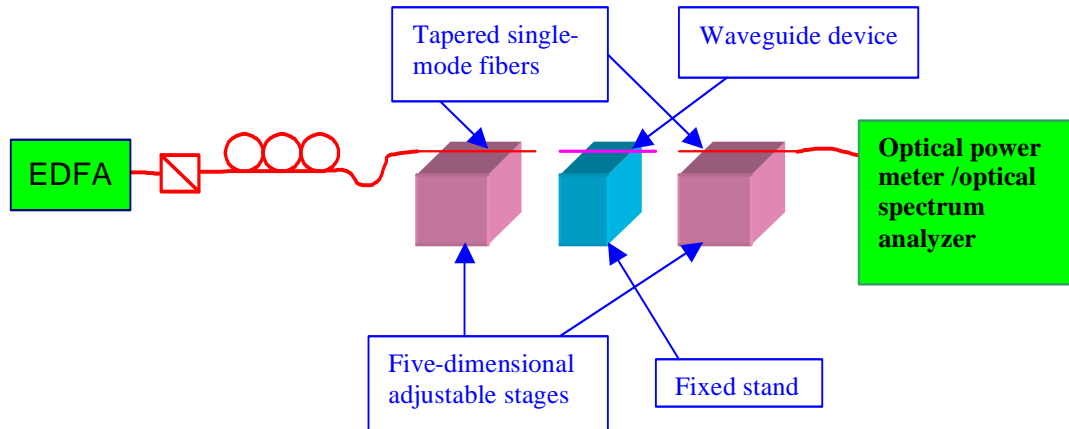


**Figure 5.16** The birefringence measurement experimental setup.

The refractive indices were measured for the signal's optical field perpendicular, parallel, or in a specific angle to the crystal c-axis for each sample with a specific  $\theta$  value. Figure 5.17 shows the measured optical transfer functions on a particular waveguide sample for  $\theta = 15^\circ$ . In the measurement, the input signals were applied in three polarization states, and the relative measured results of transfer functions are shown with the three traces in the figure. Trace 1 is for the input optical signal polarized perpendicular to the  $c$ -axis while trace 3 is for the signal parallel to the  $c$ -axis. For a better illustration, we have intentionally shifted the two traces by  $\pm 0.8$  dB based on the measured values. It can be seen that the transfer functions are

typically FP-typed. It can also be seen that there is a small difference in the periods of the two traces. This means that the effective refractive indices are slightly different for the signals with different polarizations. Furthermore, these two traces can be numerically fit by a normalized FP transfer function [34]:

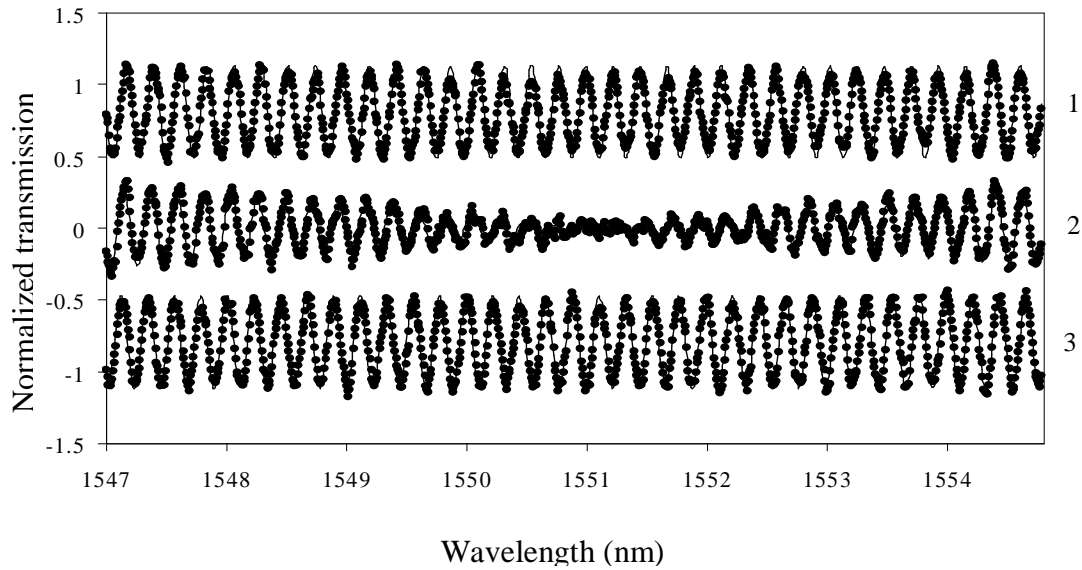


**Figure 5.17** Measured (solid dots) and calculated (continuous lines) optical transfer function with the input optical field perpendicular (trace 1), parallel (trace 3) and  $45^0$  from (trace 2) the crystal c-axis. (After [34])

$$T(\lambda) = \left\{ 1 + R^2 - 2R \cos \left[ \frac{4\pi L(n_{eff} \pm \Delta n / 2)}{\lambda} + \varphi_0 \right] \right\}^{-1} \quad (5.50)$$

Where  $L = 2.31 \text{ mm}$  is the length of the waveguide;  $R = 3.75\%$  is the effective round-trip power loss of the waveguide when it acts as a FP cavity with its end surfaces

acting as mirrors; and  $\phi_0$  is the initial phase that can be determined by the best fitting between the measured and the calculated values. If we denote  $n_{\perp}$  as the effective refractive index of the waveguide when the optical field is perpendicular to the material  $c$ -axis, and  $n_{\parallel}$  as the effective refractive index when the optical field is parallel to  $c$ -axis in the waveguide, we usually get  $n_{\perp} \neq n_{\parallel}$  when birefringence exists for the waveguide. From the numerical fitting by using equation (5.50) as shown in figure 5.17 (the solid lines), we can obtain  $n_{\parallel} = 2.357$ , and  $n_{\perp} = 2.315$  by the best fittings, as shown in traces 1 and 3. So the refractive index difference due to the birefringence is  $\Delta n = (n_{\parallel} - n_{\perp}) = 0.042$  in this particular case. To explore where this birefringence is from, we did a separate BPM simulation on the waveguide in figure 5.9, and found that the refractive index difference between the “ $\perp$ ” and the “ $\parallel$ ” polarization components induced by the waveguide structure is less than  $10^{-5}$ . This clearly indicates that the measured  $\Delta n$  value of 0.042 is primarily caused by the material birefringence instead of the waveguide structure, which means that it is not practical to try to overcome the birefringence by changing the structure, more specifically, the width and the height of the waveguide.

Another measurement and fitting were also made for the input signal splitting equally into the “ $\perp$ ” and the “ $\parallel$ ” polarization modes. This is shown as trace 2 in figure 5.17. From the figure, we could see that the ripple amplitude of the FP transfer function has a null at wavelength 1551.2 nm. This can be explained that there is a  $\pi$  phase walk-off between the TE and the TM polarization modes of that wavelength. If

we compare trace 1 and trace 3 in the figure carefully, we can clearly see this  $\pi$  phase walk-off. It is obvious that multiple nulls can be found at different wavelengths for this polarization state of the input signal by simply enlarging the measurement wavelength coverage. With the information of the wavelengths at which the nulls appear, we can determine the birefringence by [34]

$$\Delta n = \lambda_0^2 / (2L\Delta\lambda) \quad (5.51)$$

Where  $\lambda_0$  is the average wavelength used in the measurement, and  $\Delta\lambda$  is the wavelength difference between the adjacent nulls in the transfer function.

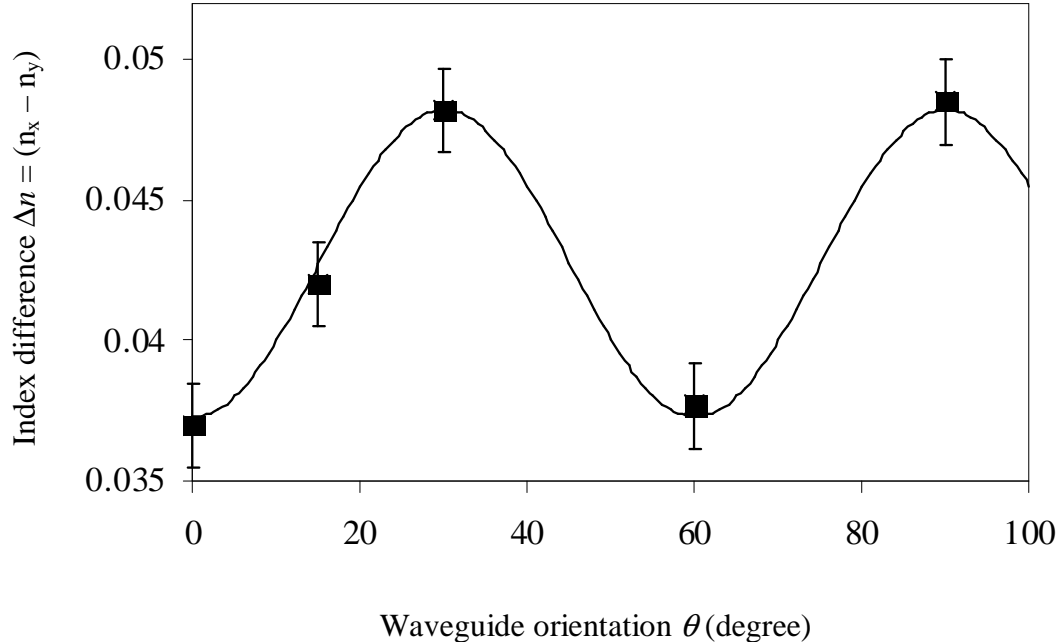


**Figure 5.18** Measured birefringence versus waveguide orientation (solid squares). The continuous line is a sinusoid fitting using,  $\Delta n = 0.04275 - 0.00545\cos(6\theta)$ , where  $\theta$  is in degree.

Besides that the two values of  $n_{\perp}$  and  $n_{\parallel}$  are not the same, more importantly, we found that there is an approximately 10% change in the index difference  $\Delta n = n_{\parallel} - n_{\perp}$  with varying the  $\theta$  value, and also a  $60^{\circ}$  periodicity was observed. Figure 5.18 shows this result, where systematic measurements were made on a number of waveguide samples with angle  $\theta = 0^{\circ}, 15^{\circ}, 30^{\circ}, 60^{\circ}$  and  $90^{\circ}$ . The continuous line in figure 5.18 is the fitting curve,  $\Delta n = 0.04275 - 0.00545 \cos(6\theta)$ , where  $\theta$  is in degree. Thus we verified that the refractive index not only depends on the optical signal polarization but also depends on the optical propagation direction within the  $a$ - $b$  plane of the waveguide samples. This is attributed to the wurtzite structure of the GaN crystal.

Although the above periodical variation of  $\Delta n$  within  $c$ -plane was obtained in the infrared wavelengths, we can assume that this  $60^{\circ}$  periodicity in  $\Delta n$  variation also exists in the wavelength regions near the band edge based on the fact that the periodical emission-efficiency variation versus angle  $\theta$  in  $c$ -plane has been reported in [70].

For most applications of planar lightwave circuits, the birefringence of the waveguide is an important issue that has to be considered. Less birefringence in the waveguides guarantees better real communication systems. Several techniques have been proposed to reduce the birefringence in the waveguides made by semiconductor materials. Those techniques include polarization compensation [71]; special waveguide cross-section design [72][73]; and the introduction of build-in compressive, or tensile stresses during the crystal growth [74][75].

The measured result given above gives us a foundation for the design of the polarization insensitive waveguide with the technique of special cross-section design. Since there are two types of birefringence: the material birefringence and the waveguide birefringence, it is important to consider both of them in the designing. Through simulation, we could design some specific waveguide birefringence in the waveguide design based on the chosen refractive indices. Then, we can carefully choose the direction of the incident beam to have some specific material birefringence. If these two types of birefringence compensate for each other, a polarization insensitive waveguide can be realized.

## 5.7 Design of Optical Couplers and Mach-Zehnder Interferometer Device with GaN/AlGaN

In Chapter 2, we discussed the principles of basic devices such as couplers, Mach-Zehnder Interferometers. In this section, we are going to design functional devices with GaN materials.

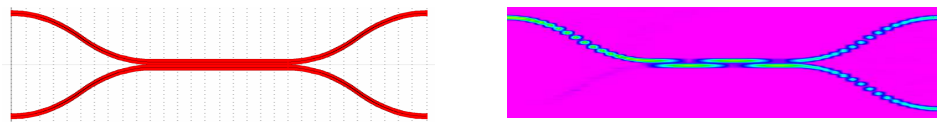


**Figure 5.19** Simulation of a 3dB coupler.

### 5.7.1 Simulation Results of Couplers and Mach-Zehnder Interferometer Device

The simulation results for our designing of simple  $2 \times 2$  waveguide couplers and Mach-Zehnder Interferometers are shown here. Figure 5.19 shows a simulation result for a  $2 \times 2$  3-dB waveguide coupler. The input power from one of the input ports of the coupler was split equally to the two output ports.

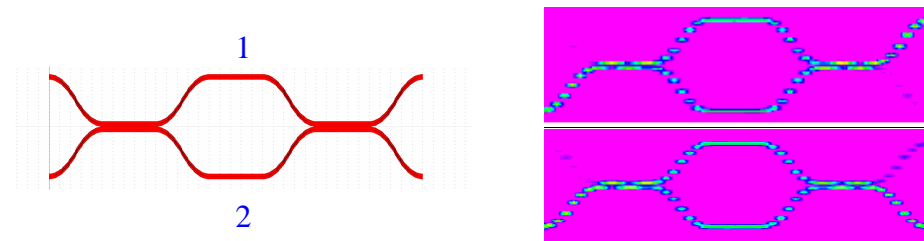


**Figure 5.20** Simulation of M-Z Interferometer optical switch controlled by carrier induced refractive index change.

Figure 5.20 shows the simulation result where a Mach-Zehnder Interferometer acted as a simple optical switch. In the simulation, the length difference  $\Delta L$  between the two arms was realized by having different refractive indices in the waveguides of the two arms. This can be made by having an electrode on one of them. In our simulation, the refractive index difference between the two arms was set as 0.0238. The signals with different wavelengths  $1.5464 \mu\text{m}$  and  $1.5625 \mu\text{m}$  were launched into the same input port. But they exit from different output ports. This simulation was set

for the design of optical switches that could be realized with carrier induced refractive index change.

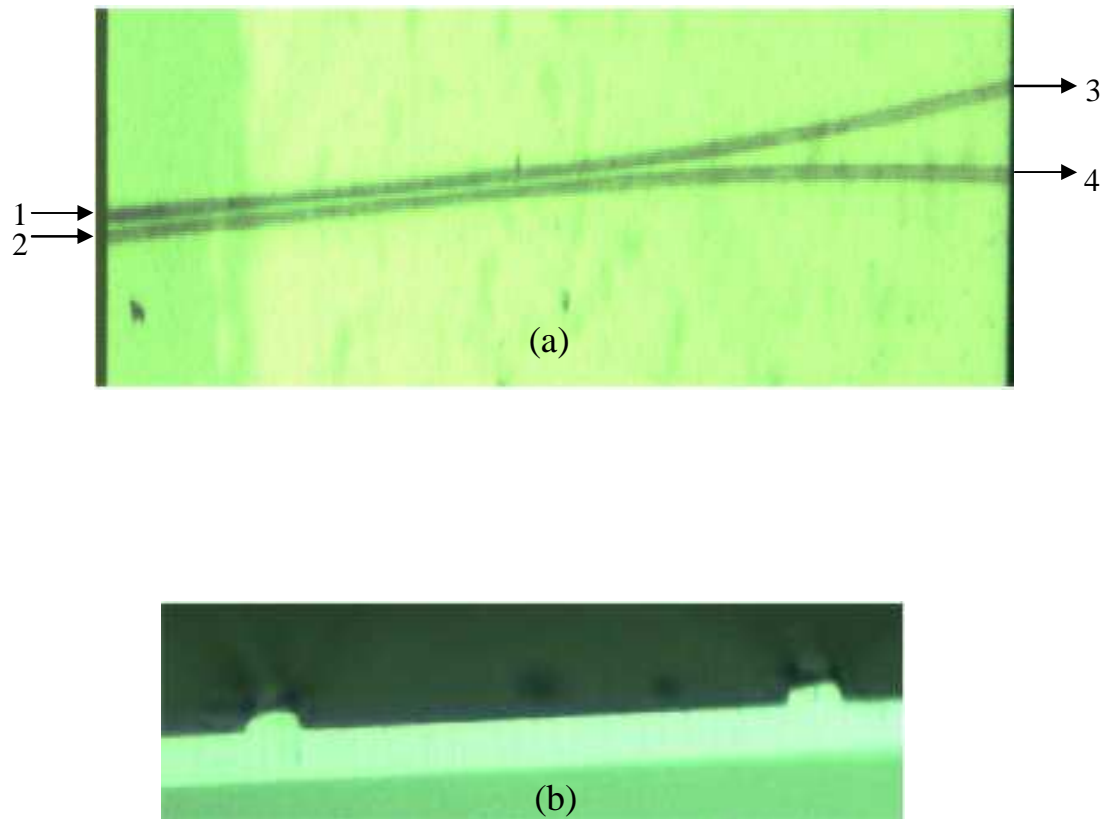


**Figure 5.21** Microscopic images of a  $2 \times 2$  GaN/AlGaN heterostructure optical waveguide coupler (a) top view and (b) cross section at the output. (Ref. [29])

### 5.7.2 A Simple Example: Waveguide Coupler

The first samples we designed have the waveguide widths all equal to  $3\mu\text{m}$ . Several different waveguide configurations were designed and fabricated. The devices included straight waveguides and  $2 \times 2$  waveguide couplers.

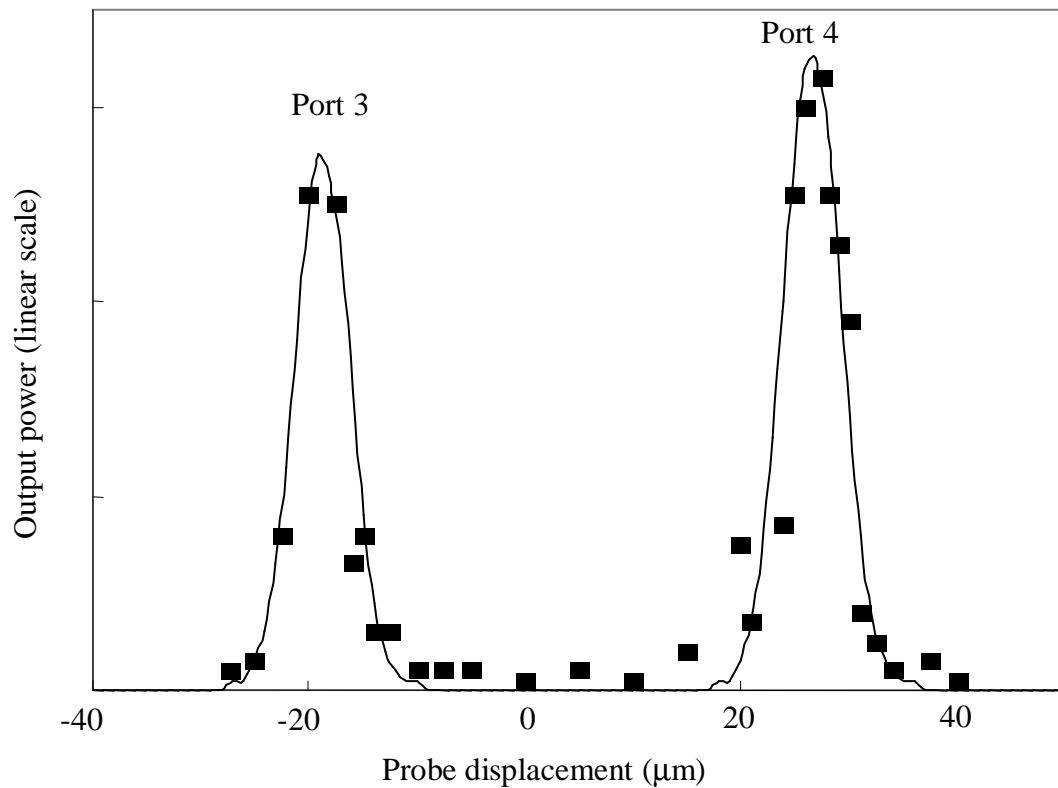


**Figure 5.22** Measured output optical power vs the probe displacement in the horizontal direction for a  $2 \times 2$  GaN/AlGaN heterostructure optical waveguide coupler. The input optical signal is launched at port 1 (as illustrated in Fig. 3-6) (Ref [29]).

Figure 5.21 shows an example of a fabricated device samples based on our design. It is a typical  $2 \times 2$  optical waveguide coupler [29]. The power splitting ratio

of this particular coupler was designed to be 3dB. To characterize the sample, the experimental setup was the same as shown in figure 5.11, except that a tunable laser was used to replace the EDFA. The result is shown in figure 5.22, where the output powers were measured at the two outputs (3 and 4) while the input power was from input port 1. From figure 5.22, we see that the experiment result is in accordance with our design. A ~50% power splitting was realized.

## 5.8 The AWG Based on the GaN/AlGaN Heterostructures

In chapter 2, we have discussed the basic principles of an AWG. In chapter 3, the AWG was used as the basic component to construct an IAWG and IAWG-based WDM cross connects or all optical switches. In this section, we are going to show the design of an AWG with GaN/AlGaN materials. We will also explain the reason why we have chosen GaN/AlGaN instead of other materials.

One approach to make the AWG devices is to use the silica PLC, which is the most popular one, and the AWGs made in this way are commercially available now. However, AWG devices made of silica are usually not tunable due to the passive nature of silica. One approach to make the AWG tunable to make wavelength switches is by using thermal tuning method [76][77]. The thermal tuning method has been briefly discussed in chapter 2, for thermo-optic Mach-Zehnder Interferometer (MZI) switch, and in the introduction part of chapter 3. In the AWG case, a small resistor is deposited near each arrayed waveguide. This small resistor can heat the

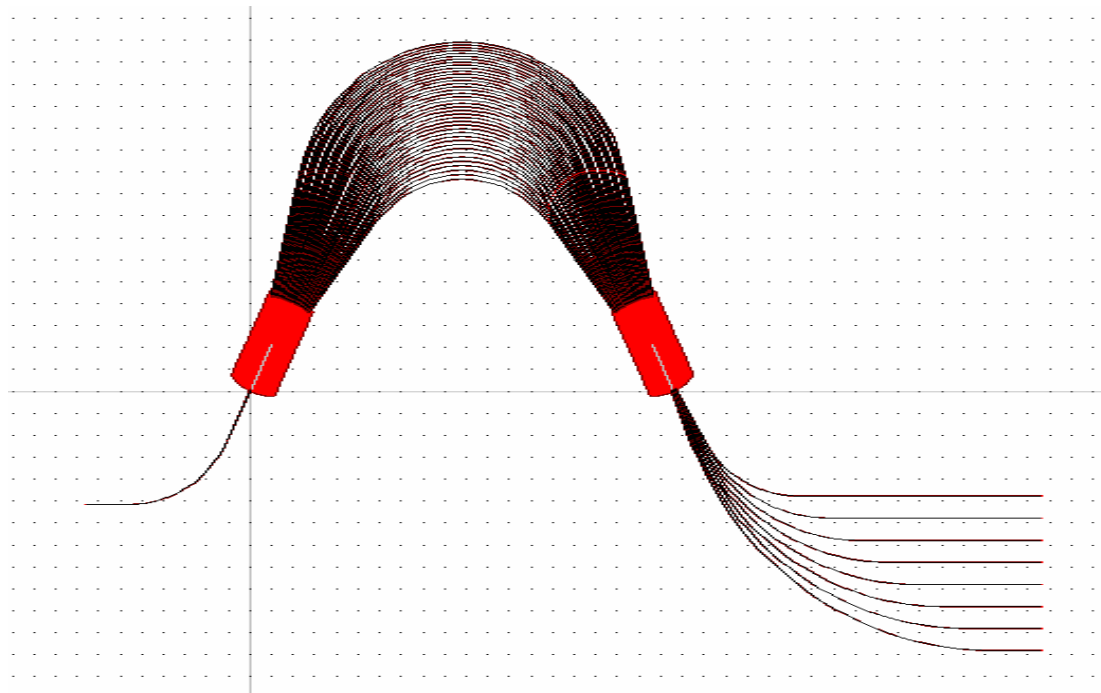
related waveguide individually to change its refractive index, so that a relative optical delay is introduced in the waveguide. However, as we have pointed out in chapter 2, this method is very slow since it is in millisecond level. It cannot be applied to the packet switch-based optical networks. Another approach is to use semiconductor materials to make planar waveguide PLCs. Since InP is semiconductor, the InP-based PLC can be potentially made fast tunable with the carrier injection [6][8]. However, there are also several disadvantages with the InP-based devices. Firstly, it has too high refractive index ( $n \approx 3.5$ ) compared with silica. The cross-section of the waveguide made of InP is very small, which causes extra coupling loss at the interface with an optical fiber, due to the refractive index mismatch, and due to the mode spot size mismatch. Secondly, the temperature sensitivity of the refractive index of InP material is very high, which is  $dn/dT \approx 10^{-4} K^{-1}$ , which is approximately 10 times higher than that of silica. So the performance of the InP-based AWG devices is very sensitive to the temperature change, and the stringent temperature control is required. This has become part of the reason why the InP-based AWG devices have not become commercially competitive so far.

Compared with InP and Silica, the III-nitrides have distinct advantages for the application of tunable AWG optical devices. The lower refractive index than InP makes the waveguide cross section larger than that of InP waveguide, which reduces the coupling loss with optical fibers significantly. The wide bandgap relative to the application wavelength 1550 nm makes the intrinsic loss and optical gain small. On the other hand, its semiconductor characteristic makes it possible to change its

refractive index by carrier injection, primarily by free carrier absorption in this case as we have discussed in chapter 4. This makes it possible to design fast tunable AWG devices.

### **5.8.1 Simulation Results of the Arrayed Waveguide Gratings**

Based on the previous simulations, another waveguide device, arrayed waveguide grating (AWG) on GaN and  $\text{Al}_x\text{Ga}_{1-x}\text{N}$  was then designed and simulated. Figure 5.23 shows this AWG configuration (a), and the related simulation result (b). The size of the AWG configuration was about  $5.5 \times 8.8 \mu\text{m}^2$ . It consisted of one input star coupler with one input port, one output star coupler with eight output ports, and 40 arrayed waveguides between the two star couplers. The waveguide had the same layered structure as in Figure 5.9. The simulation result was in accordance with what we had expected. Each of the eight output ports had its specific peak wavelength for the output signal.



(a)

**Figure 5.23** (a) Arrayed waveguide grating configuration, (b) simulation output result.

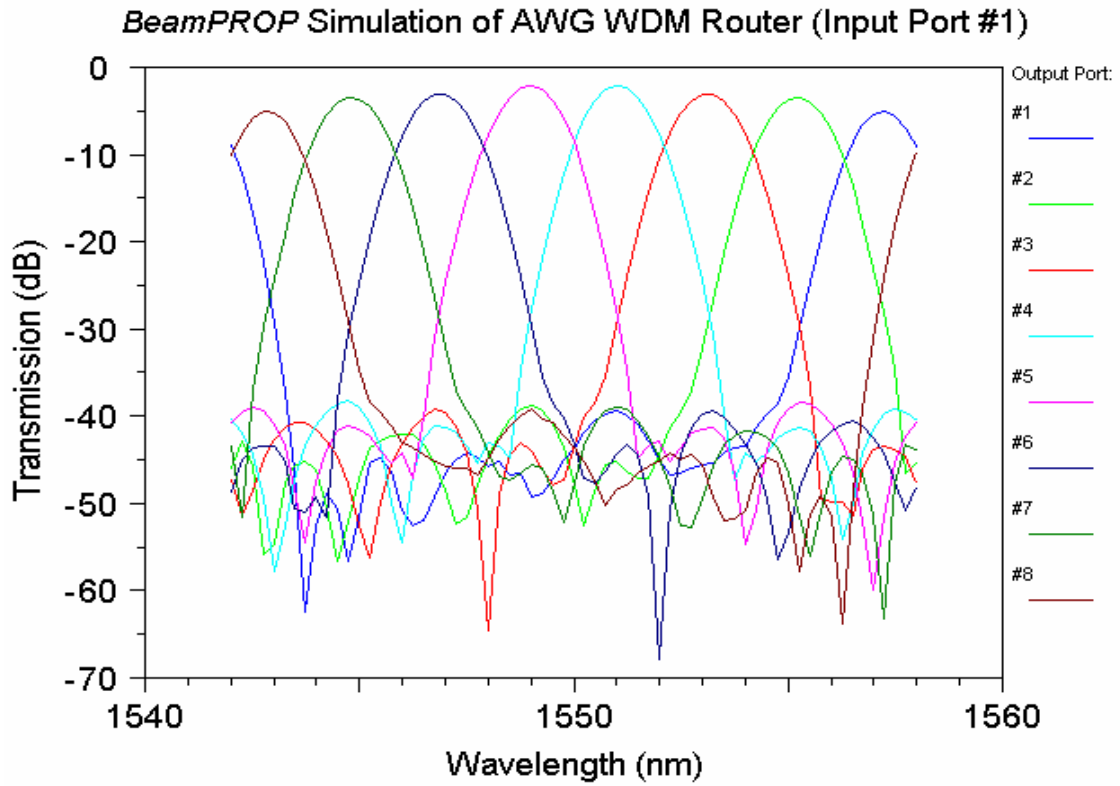
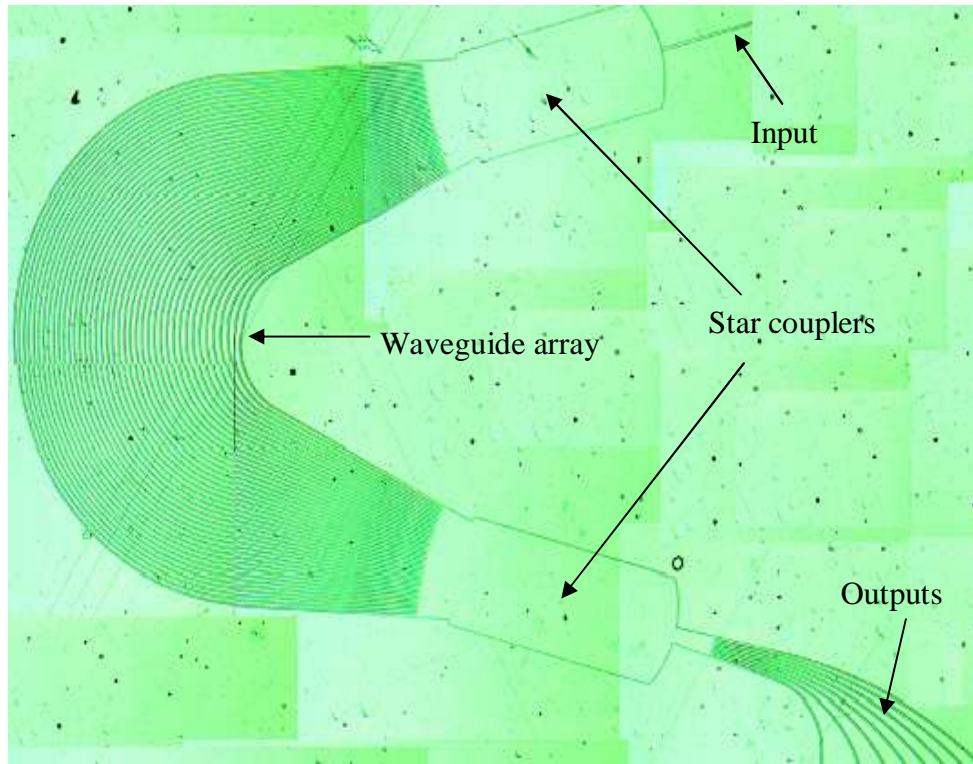


**Figure 5.23 (b)**

### 5.8.2 A Sample: A Fabricated Arrayed Waveguide Grating

To verify the feasibility, a GaN/AlGaN-based AWG was fabricated for the first time based on the simulation result as shown above. The fabrication procedure was identical to that described in section 5.3.3.3, which involved photolithographic patterning and inductively-coupled plasma (ICP) dry etching [65]. Figure 5.24 shows a sample of an AWG-based  $1 \times 8$  WDM demultiplexer. Figure 5.24(a) is a microscope picture of the device configuration, which consists of one input

waveguide, eight output waveguides, two star couplers, and 40 arrayed waveguides between the two star couplers. By design, the channel spacing of the WDM outputs is 2 nm. Figure 5.24(b) shows the measured optical transfer function versus the signal wavelength for all the eight output ports. It can be seen that the measured transfer function of the AWG generally agrees with the simulated one as shown in figure 5.23(b). The results clearly demonstrated an approximately 2 nm wavelength spacing between transmission peaks of adjacent output waveguides. This indeed verifies the accuracy of the design. It is noticed that the out-of-band rejection ratio of the measured transfer function is only approximately 10 at most of the output ports. This is mainly due to the non-uniformity of the waveguide array caused by the imperfections in the fabrication process.



(a)

**Figure 5.24** Microscope picture (a) and measured optical transfer function (b) of an AWG-based WDM coupler with 2nm channel separation.

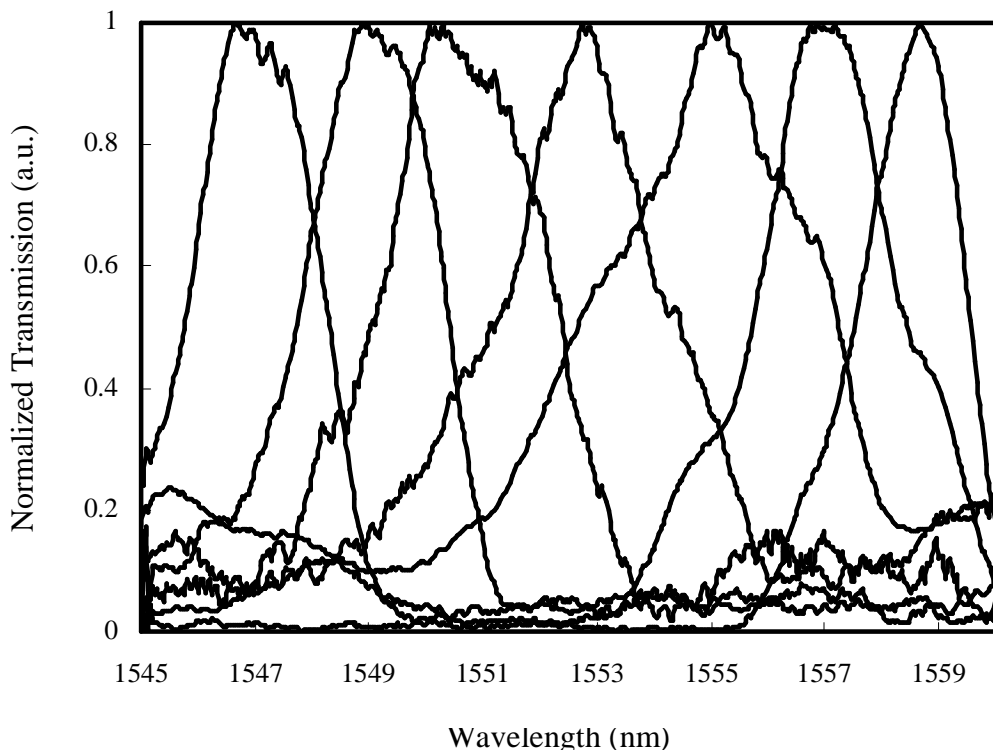


**Figure 5.24 (b)**

## 5.9 The Thermal Stability of the Refractive Index

The dependence of the refractive index of  $\text{Al}_x\text{Ga}_{1-x}\text{N}$  on temperature has been investigated extensively [78]. Although previous research has been focused on the characteristics of  $\text{Al}_x\text{Ga}_{1-x}\text{N}$  in UV and visible wavelength region, the theoretical formulation can be extended into near the infrared region. We adopt the expression of the refractive index as the function of temperature, wavelength and *Al* concentration for  $\text{Al}_x\text{Ga}_{1-x}\text{N}$  in [78]:

$$n(\lambda, x, T) = \frac{1}{\sqrt{2}} \left\{ \epsilon_r + \sqrt{\epsilon_r^2 + \epsilon_i^2} \right\}^{1/2} \quad (5.52)$$

Where  $\epsilon_r$  and  $\epsilon_i$  are the real and the imaginary parts of the dielectric constant  $\epsilon$ , respectively, with,

$$\epsilon(\lambda, x, T) = C(x, T) + \frac{A(x, T)}{E_g^{1.5}(x, T)} \cdot \frac{2 - \sqrt{1+y} - \sqrt{1-y}}{y^2} \quad (5.53)$$

$$y = \frac{hc/\lambda + i\Gamma(x, T)}{E_g(x, T)} \quad (5.54)$$

$$E_g(x, T) = 3.502 + 1.35x + 0.99x^2 - \frac{0.224}{\exp(0.386/T) - 1} \quad (5.55)$$

$$C(x, T) = 2.49 + 2.27 \times 10^{-3}T - 1.8 \times 10^{-6}T^2 - (0.74 + 4.61 \times 10^{-3}T - 5.33 \times 10^{-6}T^2)x \quad (5.56)$$

$$A(x, T) = \left\{ 79.3 - 8.37 \times 10^{-2}T - 6.73 \times 10^{-5}T^2 + (18.99 + 0.13T - 1.76 \times 10^{-4}T^2)x \right\} [eV^{1.5}] \quad (5.57)$$

$$\Gamma(x, T) = \left\{ -8.69 + 4.13 \times 10^{-2}T + (248.24 - 0.19T)x^2 \right\} \times 10^{-3} [eV] \quad (5.58)$$

This approximation is valid for the *Al* concentration  $x < 0.64$  and the accuracy was tested against the measured data obtained with a spectroscopic ellipsometer between 3.5 eV and 1.5 eV (850nm wavelength). Although the accuracy of this equation in the 1550 nm wavelength region has not been fully verified, at this wavelength that is far away from the material bandgap, no abrupt variation is expected for the material characteristics. Equations (5.52)-(5.58) will provide a

reasonably accurate estimation for the temperature sensitivity of the refractive index at 1550 nm. Figure 5.25 (a) shows the sensitivity of the refractive index against the temperature change ( $dn/dT$ ) at the wavelength of 1550 nm with various values of *Al* concentration  $x$ . Within 0 and +50 °C, the temperature sensitivity is less than  $2 \times 10^{-5} / ^\circ C$ . This value is similar to that of silica [54], and approximately one order of magnitude lower than that of InP, which is about  $3 \times 10^{-4} / ^\circ C$  [55][56] at this wavelength. It is interesting to note that for  $Al_xGa_{1-x}N$  at room temperature (25 °C), the temperature sensitivity of the refractive index is not monotonic versus *Al* concentration  $x$ , as shown in Figure 5.25(b), which shows a maximum around  $x = 0.4$ .

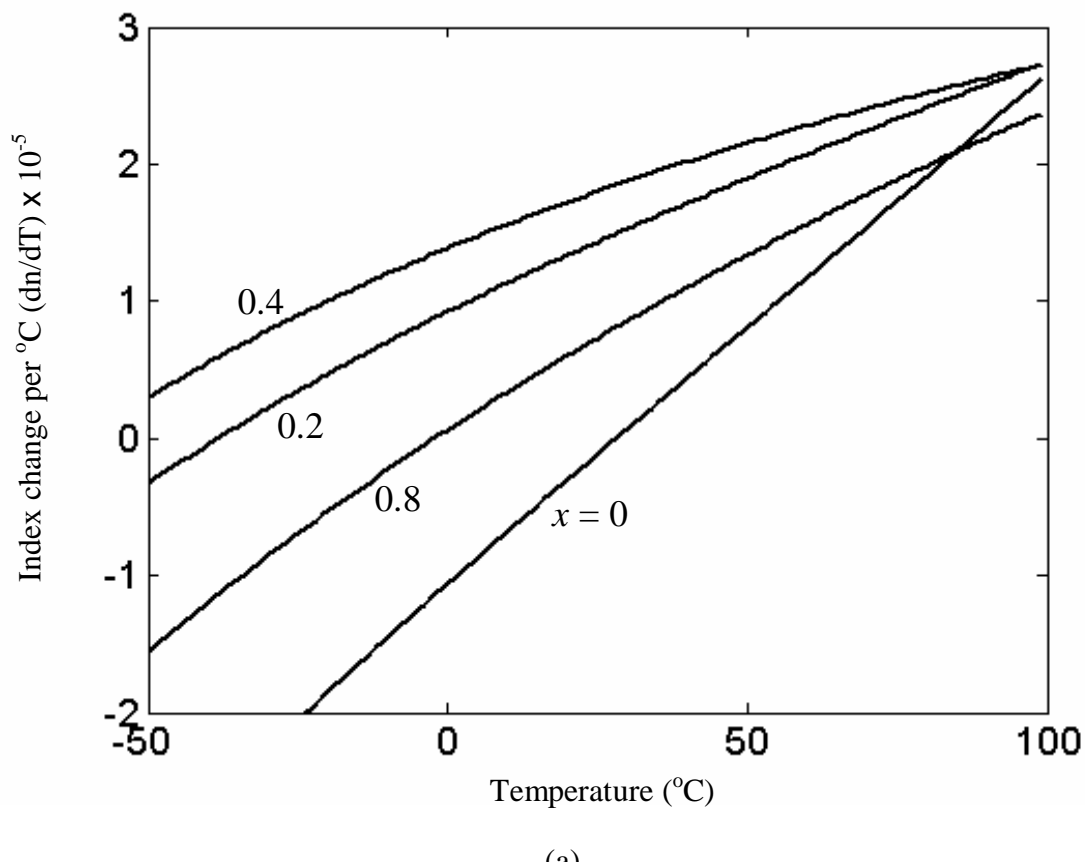


**Figure 5.25** Calculated temperature sensitivity of AlGaN refractive index, (a) as a function of operation temperature for different Al concentration  $x$  and, (b) as a function of Al concentration with a fixed operating temperature at 25°C.

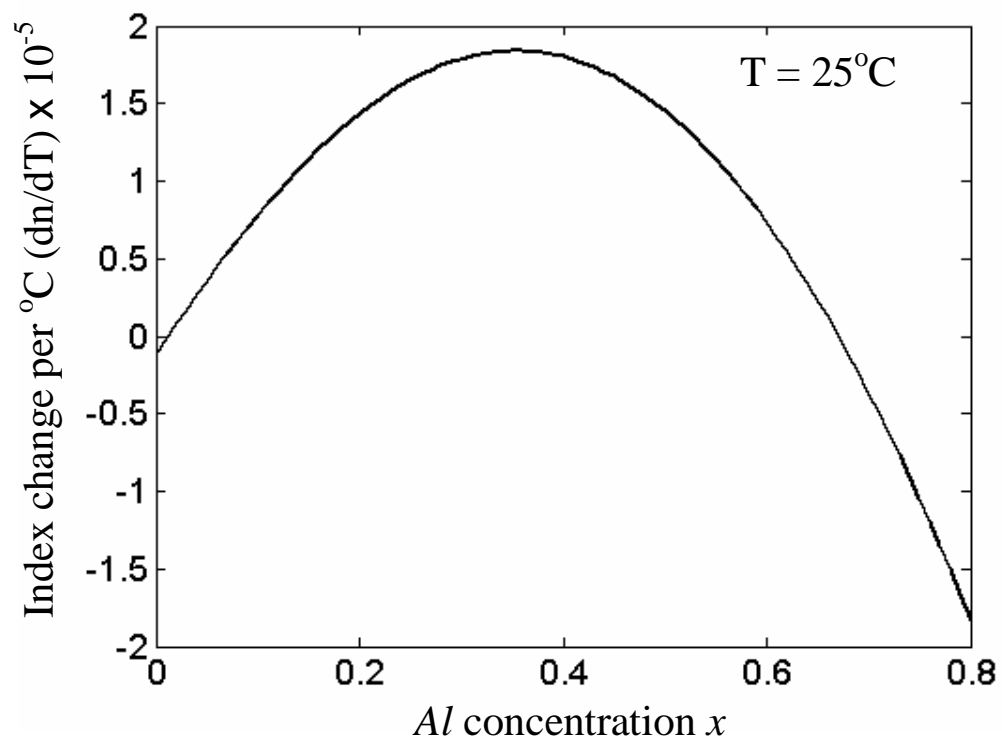


**Figure 5.25 (b)**

## 6. Conclusions and Future Work

### 6.1 Conclusions

In this dissertation, we have reviewed the basic concepts of telecommunication network architectures, optical networks, WDM network elements, and basic components in optical networks. Among the basic components, we have particularly focused on the basic principles and applications of optical couplers, Mach-Zehnder Interferometers (MZI), and arrayed waveguide gratings (AWG). In terms of large optical switch architectures, we have emphasized our interest in the Spanke architecture. Then we reviewed a number of popular switch device technologies, such as MEMS and thermo-optic switches. The MEMS technique has inspired us to build  $1 \times N$  optical switches to realize  $N \times N$  with the Spanke architecture. The thermo-optic technique has inspired us to explore the possibility of using carrier-induced semiconductor material to realize the switching of optical signals with particular wavelengths.

Our main focus has always been on all-optical switching in WDM technology. We have explored and invented a novel structure for an all-optical switch in Chapter 3. We started with the basic AWG design and expanded it into the  $N$ -interleaved AWG ( $N$ -IAWG). Compared to a conventional AWG, an  $N$ -IAWG requires a unique differential path length design in the bridge waveguides between the two star couplers. We derived a general design rule for the required differential lengths of bridge waveguides in an  $N$ -IAWG. We discovered that there exist multiple solutions to the

differential path lengths in the  $N$ -IAWG design. Based on this, we designed and systematically analyzed a  $1 \times N$  WDM switch, which consists of two  $N$ -IAWGs with a phase shifter array between them. A practical design example of a  $1 \times 4$  non-blocking WDM switch was then presented to illustrate the design steps and the methods to find the required phase assignment at each phase shifter for various output status. We also calculated the device transfer functions and discussed the switching functionalities in detail. Based on the reciprocity principle, we also proposed a simplified structure of a  $1 \times N$  WDM switch that requires only one  $N$ -IAWG, where total reflection is implemented at the end of each phase shifter. This simplified structure significantly reduces the device size and relaxes the design tolerance. It is also important to note that the proposed  $1 \times N$  switch structure is a PLC with no waveguide crossings, therefore it can be monolithically integrated to create sophisticated optical devices with various functionalities. We can use this type of  $1 \times N$  WDM switches as fundamental building blocks to construct non-blocking  $N \times N$  WDM all-optical switches, which we have also suggested in this dissertation and which will be indispensable for future all-optical networks.

The feasibility of incorporating carrier-induced index tuning into switchable PHASAR devices depends on the characteristics of semiconductors. Therefore, it is important to find proper materials to realize our unique designs. We proposed to use III-nitrides because of their unique characteristics. We presented a theoretical study of carrier-induced refractive index change in GaN semiconductors in the infrared wavelength region, which was previously not well-known. The results of this study

provide us critical material parameters for switchable phasor device designs for optical communication applications. In our approach, we have studied three carrier effects: band filling, bandgap shrinkage, and free-carrier absorption. The results indicate that in infrared wavelengths, the dominant cause of carrier-induced refractive change is due to free-carrier absorption. Through our calculation, we verified that the magnitude of carrier-induced refractive change is high enough for future applications as PHASAR devices for optical communications. The devices we proposed are feasible with GaN materials.

We then characterized the optical properties of  $\text{Al}_x\text{Ga}_{1-x}\text{N}$  epilayers in the 1550 nm wavelength region experimentally, including the refractive indices and the impact of Al concentrations. We designed various functional optical devices based on the single-mode ridged optical waveguides using GaN/AlGaN heterostructures. The devices were then systematically characterized for their operation in the 1550 nm wavelength window. We observed and studied the birefringence of wurtzite GaN grown on sapphire substrate. We found that the refractive indices were different for the signal optical field perpendicular and parallel to the crystal *c*-axis ( $n_{\perp} \neq n_{\parallel}$ ). More importantly, we found an approximately 10% change in the index difference  $\Delta n = n_{\parallel} - n_{\perp}$  when varying the waveguide orientation within the *c*-plane, with a 60° periodicity. This is attributed to the hexagonal structure of the nitride materials. This knowledge will help the understanding of polarization effect in the devices and the design of polarization independent optical waveguides. An 8-wavelength array-waveguide grating was designed and fabricated using III-nitride semiconductor

materials for the first time. The performance reasonably agrees with our design expectation, which indicates that we have good understanding of the material properties as well as device design rules. We have also investigated the thermal sensitivity of the refractive index of AlGaN in the 1550 nm wavelength region, which has been found comparable to that of silica and approximately one order of magnitude lower than that of InP.

## 6.2 Future Work

This report has demonstrated our work in three areas of all-optical switching: high level schematic designs; device structural calculations and simulations; and experimental testing and verification. Although a foundation has been formed, there is still plenty of room for future research in these three areas.

- New schematic designs can still be explored. For example, a ring resonator can be used for demultiplexing or multiplexing filters. It can also be applied to configure multiplexer by using multiple resonators [41].
- We have measured the birefringence of GaN materials. However, it still remains a task to practically design polarization insensitive waveguides in integrated optical circuits. The techniques include a careful choice of an angle between *a*-axis and the waveguide direction in the photonic circuit design. A special cross-section design of waveguide and an introduction of built-in stresses in the crystal structure are worth further exploring.
- Carrier-induced refractive index changes in the GaN rectangular waveguide have been theoretically explored and calculated. Devices designed using

theoretical calculations and simulations have been recently fabricated. The remaining work in this area is to experimentally measure the carrier-induced refractive index change. There are two ways to improve in this part. One way is to improve the sample preparation process so that we could have an ideal F-P cavity so the experimental method introduced in Chapter 5 can still be applied to measure the refractive index change. The other way is to develop novel methods to do the measurement. We have already started to try some new methods. For example, we started using a fabricated MZI device with electrodes attached to verify the results experimentally. It can be seen that either way is challenging.

- Besides the experimental verification of carrier-induced refractive index change, the design and location of the electrodes on or near optical waveguide also remains to be explored. We will then have a solid foundation to fabricate and characterize the active optical devices we proposed in this dissertation.
- After the verification of the carrier-induced refractive index change experimentally, a series of measurements needs to be taken to measure the effective refractive index changes with different carrier concentrations in waveguide samples. Then we can compare the experimental results with the theory to verify some key parameters we had chosen in the theoretical calculations.
- A thorough research in the mechanism of optical power loss needs to be carried out. For example, losses could be due to coupling to radiation modes

or due to scattering [41]. Understanding this loss mechanism could help us to design low loss waveguides. For example, we can reduce the loss due to scattering by using geometries that can minimize the mode overlap with the rough sidewalls of the waveguide [41].

- There are some approximations we made when investigating temperature sensitivity of the refractive index for GaN materials. This temperature characteristic needs to be verified experimentally.
- Recently, silicon has been widely investigated and applied as a new material for optical devices due to the recent realization of sub-micrometer-size photonic structures [41][79]. Besides the channel waveguides and ridge waveguides, novel waveguide configurations such as photonic-crystal waveguides and slot waveguides have also been proposed [41]. Because of the high refractive index of silicon, confined bent waveguides with small radii can be realized. Although there is a big difference between the materials of Silicon and III-Nitrides, the basic principles in theory, in architecture designs, and in experimental methods are very similar. Therefore we can extend our research method presented in this dissertation into silicon applications in optical telecommunications.

## 7. Bibliography

- [1] Rajiv Ramaswami and Kumar N. Sivarajan, *Optical Networks, A Practical Perspective, 2<sup>nd</sup> Ed*, Academic Press, San Francisco, 2002.
- [2] R.P. Khare, *Fiber Optics and OptoElectronics*, Oxford University Press, New Delhi, 2004.
- [3] Gerd Keiser, *Optical Fiber Communications 3<sup>rd</sup> Ed*, (McGraw-Hill, Boston, 2000).
- [4] M. F. Dautartas, A. M. Benzoni, Y. C. Chen and G. E. Blonder, “A Silicon-based moving-mirror optical switch,” *IEEE/OSA Journal of Lightwave Technology*, Vol. 10, pp. 1078-1085, 1992
- [5] L. Y. Lin, E. L. Goldstein, J. M. Simmona and R. W. Tkach, “Free-space micromachined optical switches with submillisecond switching time for large-scale optical crossconnects,” *IEEE Photonics Technology Letters*, Vol. 10, pp. 525-527, 1998.
- [6] C. R. Dorr, C. H. Joyner, L. W. Stulz and R. Monnard, “Wavelength-division multiplexing cross connect in InP,” *IEEE Photonics Technology Letters*, Vol. 10, pp. 117-119, 1998.
- [7] C. G. P. Herben, D. H. P. Maat, X. J. M. Leijtens, M. R. Leys, Y. S. Oei and M. K. Smit, “Polarization independent dilated WDM cross-connect on InP,” *IEEE Photonics Technology Letters*, Vol. 12, pp. 1599-1601, 1999

- [8] M. K. Smit and C. van Dam, “PHASAR-based WDM-devices: Principles, design and applications,” *IEEE Journal of Selected Topics in Quantum Electronics*, Vol. 2, No. 2, pp. 236-250, 1996.
- [9] S. Nakamura and G. Fasol, *The blue laser diodes*, (Springer-Verlag, Berlin, Heidelberg, New York, 1997).
- [10] Nitride News, *Compound Semiconductor*, Vol.3, page 4, 1997.
- [11] S. Taherion, R. Hui and K. Nordheden, M. Goano, A. Baldanzi, and H. X. Jiang “Experimental and theoretical study of refractive indices of wurtzite GaN thin film from visible to infrared,” *Integrated Photonics Research Conference*, Monterey, California, June 13 –15, 2001
- [12] Luying Zhou, *et al*, “Development of a GMPLS-Capable WDM optical network testbed and distributed storage application”, *IEEE Communications Magazine*, vol. 44, issue 2, pp. 23 - 29, 2006.
- [13] Guangzhi Li; Dongmei Wang; Yates, J.; Doverspike, R.; Kalmanek, C, “Detailed study of IP/ reconfigurable optical networks”, *Broadband Networks, 2004. BroadNets 2004. Proceedings. First International Conference*, pp. 64-73, 2004.
- [14] Kyeong Soo Kim, *et al*, “Design and Performance Analysis of Scheduling Algorithms for WDM-PON Under SUCCESS-HPON Architecture”, *IEEE Journal of Lightwave Technology*, vol. 23, pp.3716-3731, 2005.
- [15] Yikai Su, *et al*, “A Multirate Upgradeable 1.6-Tb/s Hierarchical OADM Network”, *IEEE Photonics Technology Letters*, vol. 16, pp.317-319, 2004.

- [16] Zhaoxin Wang, Chinlon Lin, and Chun-Kit Chan, “Demonstration of a Single-Fiber Self-Healing CWDM Metro Access Ring Network With Unidirectional OADM”, *IEEE Photonics Technology Letters*, vol. 18, pp.163-165, 2006.
- [17] Michael Vasilyev, *et al*, ““Broadcast and Select” OADM in  $80 \times 10.7$  Gb/s Ultra-Longhaul Network”, *IEEE Photonics Technology Letters*, vol. 15, pp.332-334, 2003.
- [18] June-Koo Rhee, Ioannis Tomkos, and Ming-Jun Li, “A Broadcast-and-Select OADM Optical Network With Dedicated Optical-Channel Protection”, *IEEE Journal of Lightwave Technology*, vol. 21, pp.25-31, 2003.
- [19] A. Yariv, *Optical Electronics in Modern Communications*, Oxford University Press, 1997.
- [20] H. Takahashi, K. Oda, H. Toba, Y. Inoue, “Transmission Characteristics of Arrayed Waveguide  $N \times N$  Wavelength Multiplexer”, *J. of Lightwave, Technol.*, vol. 13, pp. 447-455, March 1995.
- [21] “What is MEMS Technology?”  
URL: <http://www.memsnet.org/mems/what-is.html>
- [22] C. Dragone, “An  $N \times N$  optical multiplexer using a planar arrangement of two star couplers,” *IEEE Photon. Technol. Lett.* vol. 3, pp. 812-815, Sept. 1991.
- [23] C. Dragone, C. A. Edwards, and R. C. Kistler, “Integrated optics  $N \times N$  multiplexer on silicon,” *IEEE Photon. Technol. Lett.* vol. 3, pp. 896-899, Oct. 1991.

- [24]Y. Tachikawa, Y. Inoue, M. Kawachi, H. Takahashi, and K. Inoue, “Arrayed-waveguide grating add-drop multiplexer with loop-back optical paths,” *Electron. Lett.*, vol. 29, pp. 2133-2134, Nov. 1993.
- [25]H. Takahashi, O. Ishida, K. Oda and H. Toba, “Anticrosstalk arrayed-waveguide add-drop multiplexer with foldback paths for penalty free transmission,” *Electron. Lett.*, vol. 30, pp. 2053-2055, Nov. 1994.
- [26]S. Matsuo, Y. Yoshikuni, T. Segawa, Y. Ohiso and H. Okamoto, “A Widely Tunable Optical Filter Using Ladder-Type Structure,” *IEEE Photon. Technol. Lett.* vol. 15, pp. 1114-1116, Aug. 2003.
- [27]C. R. Doerr, “Proposed WDM Cross Connect Using a Planar Arrangement of Waveguide Grating Routers and Phase Shifters,” *IEEE Photon. Technol. Lett.* vol. 10, pp. 528-530, Apr. 1998.
- [28]C. R. Doerr, C. H. Joyner, L. W. Stulz, and R. Monnard, “Wavelength-Division Multiplexing Cross Connect in InP,” *IEEE Photon. Technol. Lett.* vol. 10, pp. 117-119, Jan. 1998
- [29] R. Hui, *et al*, “GaN-based waveguide devices for long-wavelength optical communications”, *Appl. Phys. Lett.*, vol. 82, 1326(2003).
- [30]Ivan Kaminow, Tingye Li, *Optical Fiber Telecommunications IV A Components*, Chapter 9, Academic Press, San Diego, 2002.
- [31]*BeamPROP AWG Utility Version 2.1*, Rsoft, Inc. Research Software.
- [32] C. Dragone, “Optimum design of a planar array of tapered waveguides,” *J. Opt. Soc. Amer.A*. vol. 7, pp. 2081-2091, 1990.

- [33]K. Okamoto, *Fundamentals of Optical Waveguides*, Academic Press, 2000
- [34]R. Hui, *et al*, “III-Nitride-Based Planar Lightwave Circuits for Long Wavelength Optical Communications”, *IEEE J. Quantum Electron.*, vol. 41, no. 1, pp.100-110, Jan, 2005.
- [35]B. R. Bennett, Richard A. Soref, Jesús A. Edl Alamo, “Carrier-Induced Change in Refractive Index of InP, GaAs, and InGaAsP”, *IEEE J. Quantum Electron.*, vol. 26, pp.113-122, 1990.
- [36]K. Ishida, H. Nakamura, H. Matsumura, T. Kadoi, and H. Inoue, “InGaAsP/InP optical switches using carrier induced refractive index change,” *Appl. Phys. Lett.*, vol. 50, pp.141-142, 1987.
- [37]W. Kowalsky and K. J. Ebeling, “Optically controlled transmission of InGaAsP epilayers,” *Opt. Lett.*, vol. 12, pp. 1053-1055, 1987.
- [38] J. G. Mendoza-Alvarez, R. H, Yan and L. A. Coldren, “Contribution of the band-filling effect to the effective refractive-index change in double-heterostructure GaAs/AlGaAs phase modulators,” *J. Appl. Phys.*, vol. 62, pp. 4548-4553, 1987.
- [39] J. G. Mendoza-Alvarez, L. A. Coldren, A. Alping, R. H, Yan, T. Hausken, K. Lee, and K. Pedrotti, “Analysis of depletion edge translation lightwave modulators,” *J. Lightwave Technol.*, vol. 6, pp 793-808, 1988.
- [40] J. Manning, R. Olshansky, and C. B. Su, “The carrier-induced index change in AlGaAs and 1.3  $\mu\text{m}$  InGaAsP diode lasers,” *IEEE J. Quantum Electron.*, vol. QE-19, pp 1525-1530, 1983.

- [41] Michal Lipson, “Guiding, Modulating, and Emitting Light on Silicon—Challenges and Opportunities,” *J. Lightwave Technol.*, vol. 23, pp 4222-4238, 2005.
- [42] E. Burstein, “Anomalous optical absorption limit in InSb” *Phys. Rev.*, vol. 93, pp 632-633, 1954.
- [43] T. S. Moss, G. J. Burrell, and B. Ellis, *Semiconductor Opto-electronics*. New York: Wiley, 1973, pp 48-94.
- [44] B. R. Bennett, Richard A. Soref, “Electrorefraction and electroabsorption in InP, GaAs, GaSb, InAs, and InSb”, *IEEE J. Quantum Electron.*, vol. QE-23, pp.2159-2166, 1987.
- [45] A. Yariv, Optical Electronics, 3rd ed. New York: Holt, Rinehart and Winston, 1985, pp. 474-478.
- [46] E. Michael, et al, *Properties of Advanced Semiconductor Materials, GaN, AlN, InN, BN, SiC, SiGe*, John Wiley & Sons, Inc., New York, 2001.
- [47] J. F. Muth, J. H. Lee, I. K. Shmagin, R. M. Kolbas, H. C. Casey, Jr., B. P. Keller, U. K. Mishra, and S. P. DenBaars, “Absorption coefficient, energy gap, exciton binding energy, and recombination lifetime of GaN obtained from transmission measurements,” *Appl. Phys. Lett.* 71, 18(1997), 2572-2574.
- [48] J. D. Dow and D. Redfield, “Toward a unified theory of Urbach’s rule and exponential absorption edges,” *Phys. Rev. B*, vol. 5, pp. 594-610, 1972.

- [49] C. H. Henry, R. A. Logan, and K. A. Bertness, “Spectral dependence of the change in refractive index due to carrier injection in GaAs lasers,” *J. Appl. Phys.*, vol. 52, pp. 4457-4461, 1981.
- [50] Shun Lien Chuang, *Physics of Optoelectronic Devices*, John Wiley & Sons, New York, 1995.
- [51] E. A. J. Marcatili, “Dielectric rectangular waveguide and directional coupler for integrated optics,” *Bell Syst. Tech. J.* **48**, 2071-2102 (1969)
- [52] E. A. J. Marcatili, “Slab-coupled waveguides,” *Bell Syst. Tech. J.* **53**, 645-674 (1974)
- [53] Katsunari Okamoto, *Fundamentals of Optical Waveguides*, ACADEMIC PRESS, San Diego, 2000.
- [54] M. Levy, L. Eldada, R. Scarmozzino, R.M. Osgood, Jr., P.S.D. Lin, and F. Tong, “Fabrication of Narrow-Band Channel-Dropping Filters”, *IEEE Photon. Technol. Lett.* vol. 4, p. 1378, 1992.
- [55] L. Eldada, M. N. Ruberto, M. Levy, R. Scarmozzino, and R. M. Osgood, Jr., “Rapid Direct Fabrication of Active Electro-Optic Modulators in GaAs”, *J. Lightwave Tech.*, vol. 12, p. 1558, 1994.
- [56] I. Ilic, R. Scarmozzino, R.M. Osgood, Jr., J.T. Yardley, K.W. Beeson, and M.J. McFarland, “Modeling Multimode-Input Star Couplers in Polymers”, *J. Lightwave Tech.*, vol. 12, p. 996, 1994.
- [57] I. Ilic, R. Scarmozzino, R.M. Osgood, Jr., J.T. Yardley, K.W. Beeson, and M.J. McFarland, and J. Schweyen, “Photopatterned Polymer Multimode 8x8 Star

Couplers: Comparative Design Methodologies and Device Measurements”, *IEICE Trans. Commun.*, vol. E80-B, 1997.

- [58] L. Eldada, R. Scarmozzino, R.M. Osgood, Jr., D.C. Scott, Y. Chang, and H.R. Fetterman, “Laser-Fabricated Delay Lines in GaAs for Optically-Steered Phased-Array Radar”, *J. Lightwave Tech.*, vol. 13, p. 2034, 1995.
- [59] M.H. Hu, Z. Huang, K.L. Hall, R. Scarmozzino, and R.M. Osgood, Jr., “An Integrated Two-Stage Cascaded Mach-Zehnder Device in GaAs”, *J. Lightwave Tech.*, vol. 16, pp. 1447-1455, 1998.
- [60] M. Hu, R. Scarmozzino, M. Levy, and R.M. Osgood, Jr., “A low-loss and compact waveguide y-branch using refractive index tapering”, *Photon. Tech. Lett.*, vol. 9, pp. 203-205, 1997.
- [61] R. Scarmozzino, R.M. Osgood, Jr., L. Eldada, J.T. Yardley, Y. Liu, J. Bristow, J. Stack, J. Rowlette, and Y.S. Liu, “Design and Fabrication of Passive Optical Components for Multimode Parallel Optical Links”, *SPIE Photonic West Meeting*, San Jose, CA, vol. 3005, p. 257, 1997.
- [62] M. Hu, J.Z. Huang, R. Scarmozzino, M. Levy, and R.M. Osgood, Jr., “Tunable Mach-Zehnder polarization splitter using height-tapered y-branches”, *Photon. Tech. Lett.*, vol. 9, pp. 773-775, 1997.
- [63] J. Fujita, M. Levy, R. Scarmozzino, R.M. Osgood, Jr., L. Eldada, and J.T. Yardley, “Integrated Multistack Waveguide Polarizer”, *Photon. Tech. Lett.*, vol. 10, pp. 93-95, 1998.
- [64] *BeamPROP<sup>TM</sup>* Version 5.0, Rsoft, Inc

URL: <http://www.rsoftinc.com>

- [65] T. N. Oder, J. Y. Lin and H. X. Jiang, "Propagation properties of light in AlGaN/GaN quantum-well waveguides," *Applied Physics Letters*, Vol. 79, pp. 2511-2513, 2001
- [66] Max Ming-Kang Liu, *Principles and Applications of Optical Communications*, McGraw-Hill, Inc., Chicago, 1996.
- [67] K. B. Nam, J. Li, M. L. Nakarmi, J. Y. Lin, and H. X. Jiang, "Achieving highly conductive AlGaN alloys with high Al contents," *Appl. Phys. Lett.* Vol. 81, pp. 1038-1040, 2002.
- [68] V. Fiorentini, F. Bernardini, F. Della Sala, A. Di Carlo and P. Lugli, "Effects of macroscopic polarization in III-V nitride multiple quantum wells", *Phys. Rev. B*, 60, 8849, (1999)
- [69] S. Ghosh, P. Waltereit, O. Brandt, H. T. Grahn and K. H. Ploog, "Polarization-dependent spectroscopic study of M-plane GaN on  $\gamma$ -LiAlO<sub>2</sub>", *Appl. Phys. Lett.* 80, 413 (2002)
- [70] T. N. Oder, J.Y. Lin and H.X. Jiang, "Fabrication and Optical Characterization of III-Nitride Sub-micron Waveguides," *Appl. Phys. Lett.*, vol. 79, pp. 12-14, 2001
- [71] M. Zirngibl, C. H. Joyner and P. C. Chou, "Polarization compensated waveguide grating router on InP," *IEEE Electronics Letters*, Vol. 31, No. 19, pp. 1662-1664, 1995.

- [72] H. Bissessur, P. Pagnod-Rossiaux, R. Mestic, and B. Martin, “Extremely small polarization independent phased-array demultiplexers on InP,” IEEE Photonics Technology Letters, Vol. 8, No. 4, pp. 554-556, 1996.
- [73] J. Sarathy, S. Chandrasekhar, A. D. Dentai, and C. R. Doerr, “Polarization insensitive waveguide grating routers in InP,” IEEE Photonics Technology Letters, Vol. 10, No. 2, pp. 145-147, 1998.
- [74] IEEE J. Quantum Electronics, Special Issue on *Strained-layer Optoelectronic Materials and Devices*, Vol. 30, No. 2, 1994.
- [75] T. Kakitsuka, Y. Shibata, M. Itoh, Y. Kadota, Y. Tohmori and Y. Yoshikuni, “Influence of buried structure on polarization sensitivity in strained bulk semiconductor optical amplifiers,” IEEE J. Quantum Electronics, Vol. 38, No. 1, pp. 85-92, 2002.
- [76] M. Okuno, K. Kato, Y. Ohmori, M. Kawachi and T. Matsunaga, “Improved 8x8 integrated optical matrix switch using silica-based planar lightwave circuits,” IEEE/OSA Journal of Lightwave Technology, Vol. 12, pp. 1597-1605, 1994.
- [77] N. Takato, T. Kominato, A. Sugita, K. Jingugi, H. Toba and M. Kawachi, “Silica-based integrated optical Mach-Zehnder multi/demultiplexer family with channel spacing of 0.01 – 250nm,” IEEE Selected areas in Communications, Vol. 8, No. 6, pp. 1120-1127, 1990.

[78] U. Tisch, B. Meyler, O. Katz, E. Finkman and J. Salzman, “Dependence of the refractive index of  $\text{Al}_x\text{Ga}_{1-x}\text{N}$  on temperature and composition at elevated temperatures,” *J. Appl. Phys.*, Vol. 89, No. 5, pp. 2676-2685, 2001.

[79] R. C. Johnson. (2002). “Intel reveals long-term goals for silicon photonics, sensors,” *Electron. Eng. Times.* Available: <http://www.eetimes.com/semi/news/OEG20020228S0033>